ORGANIC CHEMISTRY FRONTIERS

RESEARCH ARTICLE

View Article Online
View Journal | View Issue

Cite this: *Org. Chem. Front.*, 2024, **11**, 5340

Z-shaped polycyclic aromatic hydrocarbons with embedded five-membered rings and their application in organic thin-film transistors†‡

Sven M. Elbert,[a] Evelin Bolgert,[a] Owen T. A. Paine,[a] Farhad Ghalami,[b] Wen-Shan Zhang,[a] Ute Zschieschang,[c] Frank Rominger,[a] Dennis Popp,[a] Hagen Klauk,[c] Marcus Elstner[b] and Michael Mastalerz*[a]

Received 8th July 2024,
Accepted 26th July 2024

DOI: 10.1039/d4qo01252f

rsc.li/frontiers-organic

Z-shaped polycyclic hydrocarbons with embedded five-membered rings as well as their diaza-analogues have been synthesized. Soluble congeners were obtained by the introduction of mesityl substituents and studied by cyclo- as well as differential pulse voltammetry revealing an amphoteric redox behavior. Unsubstituted congeners showed close π-stacking in single crystal X-ray diffraction analyses and thus promising characteristics for the application as semiconducting materials in p-channel thin-film transistors (TFTs). The hole transport characteristics of the corresponding devices were investigated by GIWAXS.

Introduction

Polycyclic aromatic hydrocarbons with fused five-membered rings (also named cyclopenta-fused or short cp-PAHs) are a subclass of non-alternant PAHs with unique electronic and photophysical properties.[1,2] cp-PAHs often represent cut-outs of fullerenes such as C_{60} or C_{70} and have a high electron affinity.[3–8] Thus, cp-PAHs found application as semiconductors in electronic devices.[9–11] For example, the dibenzo[*a*,*m*]rubicene (Fig. 1),[12] a cut-out of C_{70} with two five-membered rings in the aromatic backbone was used as p-type organic semiconductor with a field effect mobility of 1.0 $cm^2 V^{-1} s^{-1}$ in thin-film transistors (TFTs).[13–15] Another cp-PAH with two five-membered rings, a derivative of acenaphto[1,2-*k*]fluoranthene[16] (Fig. 1), was used as a green emissive dye in organic light-emitting diodes (OLEDs).[17]

Besides cp-PAHs, zethrenes are another class of Z-shaped PAHs with exceptional properties.[18,19] They have biradical character with indices up to $y_0 = 0.58$. The y_0-values were tuned by benzannulation as shown in the cases of the 1,2:9,10-, and the 5,6:13,14-dibenzoheptazethrenes (short: DBHZ; Fig. 1).[20] Furthermore, for organic field effect transistors (OFETs) based on single crystals of a DBHZ, a hole mobility up to 0.15 $cm^2 V^{-1} s^{-1}$ was obtained.[21]

Rubicenes[14,22–25] and some of their extended congeners are rare examples combining both, a molecular Z-shape with

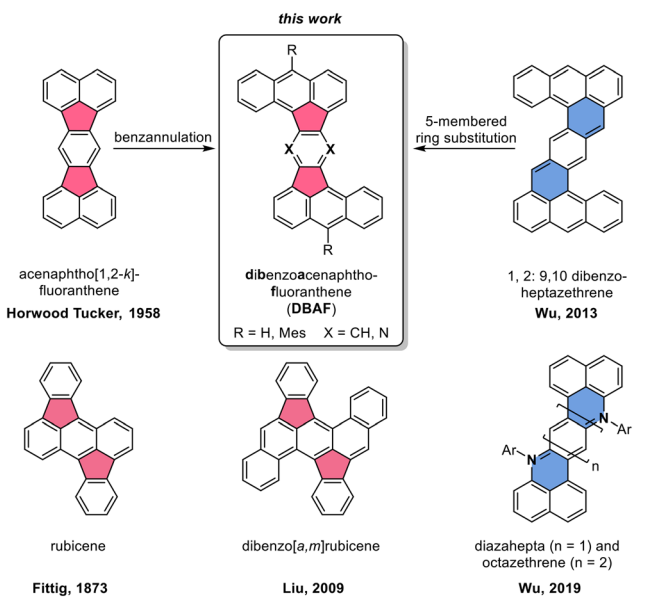

Fig. 1 Top: Molecular structures of acenaphtho[1,2-*k*]fluoranthene[16] (left) and 1,2:9,10-dibenzoheptazethrene[20] (right) and the hypothetical structural relationship to the dibenzoacenaphthofluoranthenes (**DBAFs**; middle). Bottom: Structure of rubicene (left),[22,23] dibenzo[*a*,*m*]rubicene[12] and diaza zethrenes.[27]

[a]*Institute of Organic Chemistry, Ruprecht-Karls-Universtity Heidelberg, Im Neuenheimer Feld 270, 69120 Heidelberg, Germany. E-mail: michael.mastalerz@oci.uni-heidelberg.de*
[b]*Institute of Physical Chemistry and Theoretical Chemical Chemistry, Karlsruhe Institute of Technology, Kaiserstraße 12, D-76131 Karlsruhe, Germany*
[c]*Max Planck Institute for Solid State Research, Heisenbergstr. 1, 70569 Stuttgart, Germany*

† Dedicated to Prof. Dr. Frank Würthner on the occasion of his 60th birthday.

‡ Electronic supplementary information (ESI) available. CCDC 2353527–2353534. For ESI and crystallographic data in CIF or other electronic format see DOI: https://doi.org/10.1039/d4qo01252f

embedded five-membered rings which is created by a phenyl–anthracenyl–phenyl scaffold (Fig. 1).[26] We envisioned to extend the portfolio of PAHs (or cp-PAHs) in this respect by a series of compounds which can be understood either as benzannulated acenaphtofluoranthenes or as 1,2:9,10-dibenzoheptazethrenes with two six-membered rings formally substituted by five-membered ones (shown in blue and red in Fig. 1). Therefore, these compounds are named dibenzoacenaphthofluoranthenes, abbreviated as DBAFs. The DBAFs have an "inverted" anthracenyl-phenyl-anthracenyl scaffold in comparison to rubicenes (Fig. 1).[26]

By simple modifications of the molecular precursors, nitrogen substituted analogues (the DBAF-N_2s) are accessible to investigate the influence of nitrogen substitution on the compounds' properties which was for example realized for diazahepta and octazethrenes[27–29] (Fig. 1) and is generally rare in the field of cp-PAHs.[30,31]

Results and discussion

The Z-shaped five-membered ring containing PAHs were obtained by Suzuki–Miyaura cross-coupling reactions followed by palladium-catalysed arylations under C–H activation starting from dichlorodibromobenzene **1**[32] or -pyrazine **2**[33] (Scheme 1). The cross-coupling of **1** or **2** with 9-anthracenylboronic acid **3** gave the corresponding products **5** and **6** in 80% and 56% yield respectively. The mesityl-substituted congeners **7** and **8** were obtained from **1** and **2** with 10-mesityl-anthracenyl boronic pinacol ester **4** in 34% and 68% yield. Compounds **5–8** were fully characterized by NMR as well as IR spectroscopy, mass spectrometry and their constitution was unambiguously proven by single crystal X-ray diffraction (SCXRD; for details see ESI‡).

Subjecting the four dichlorinated precursors **5–8** to typical conditions for arylations under C–H-activation ($PdCl_2(PCy_3)_2$, DBU, DMAc, 200 °C, 48 h)[34–41] gave after sublimation unsubstituted **DBAF** in 96% and **DBAF-N_2** in 55% yield as well as the mesityl substituted **mes-DBAF** in 33% and **mes-DBAF-N_2** in 69% after column chromatography (Scheme 1). The parent **DBAF** and **DBAF-N_2** are poorly soluble in common organic solvents at room temperature and NMR spectroscopy had to be performed in *ortho*-dichlorobenzene-d_4 at elevated temperatures (323 K; see ESI‡). The successful pentannulations have been proven by 1D- and 2D-NMR spectroscopy as well as mass spectrometry (see ESI‡) and by SCXRD analyses (see discussion below).

The optical properties of the DBAF series were investigated by UV/vis- as well as fluorescence spectroscopy in *o*DCB (**DBAF** and **DBAF-N_2**) or dichloromethane (**mes-DBAF** and **mes-DBAF-N_2**) (Fig. 2 and Table 1). **DBAF** and **DBAF-N_2** were only soluble in *o*DCB after heating and ultrasonication. **DBAF** shows an intensive absorption maximum at λ_{abs} = 349 nm and additional low energy absorption maxima at λ_{abs} = 461, 491, 518 and 550 nm. A red emission can be detected by bare eye, which corresponds to a maximum at λ_{em} = 572 nm and a shoulder at λ_{em} ~ 620 nm with a Stokes shift of $\tilde{\nu}$ = 699 cm^{-1} and a photoluminescence quantum yield of φ = 21%.

mes-DBAF shows similar spectroscopic properties as its non-mesitylated analogue with a high intensity absorption band at λ_{abs} = 350 nm (**DBAF**: 349 nm) and again poorly resolved maxima at λ_{abs} = 460, 493, 526 and 561 nm and a slightly red-shifted emission with λ_{em} = 588 nm (**DBAF**: 572 nm) leading to a larger Stokes shift of $\tilde{\nu}$ = 819 cm^{-1} (φ = 20%, Table 1).

DBAF-N_2 shows two maxima at λ_{abs} = 379 and 399 nm and a less resolved pattern of overlapping adsorption maxima with a most red-shifted maximum at λ_{abs} = 519 nm with a shoulder at λ_{abs} = 555 nm. The corresponding emission maximum is found at λ_{em} = 577 nm with a shoulder at λ_{em} = 621 nm and a

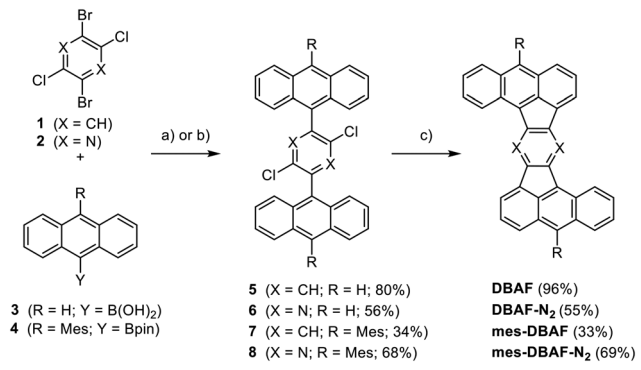

Scheme 1 Synthesis of **DBAF**, **DBAF-N_2**, **mes-DBAF** and **mes-DBAF-N_2** from dibromodichlorobenzene **1** and dibromodichloropyrazine **2**. (a) For **5** and **7**: $Pd(OAc)_2$ (2.5–3 mol%), SPhos (5–6 mol%), $K_2CO_{3\ aq.}$ (1 M), THF, 85 °C 16 h; for **6** and **8**: (b) $Pd(dppf)Cl_2$ (10 mol%), K_2CO_3 (1 M), THF, 85 °C, 16 h, (c) $PdCl_2(PCy_3)_2$, DBU, DMAc, 200 °C, 16 h.

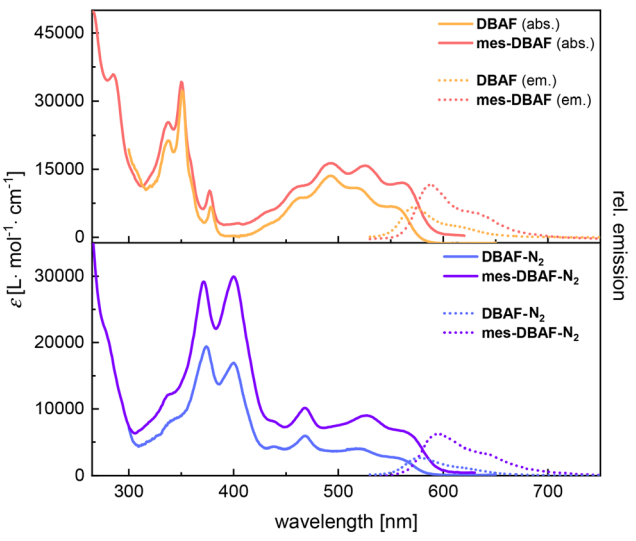

Fig. 2 UV/vis absorption (solid lines) and fluorescence (dashed lines) spectra of **DBAF** (red) and **mes-DBAF** (orange) (top) and **DBAF-N_2** (blue) and **mes-DBAF-N_2** (violet) (bottom), measured in *o*-DCB (**DBAF** and **DBAF-N_2**) or CH_2Cl_2 (**mes-DBAF**) and **mes-DBAF-N_2** at room temperature.

Table 1 Optical and electronic properties of the DBAF-series

Cmpd	λ_{max} [nm] [a,b]	λ_{onset} [nm] [b]	$E_{gap,opt}$ [eV] [c]	λ_{em} [nm] [b]	$\tilde{\nu}_{Stokes}$ [cm^{-1}] [b]	$PLQY$ [%] [b]	$E_{IP,CV}$ [eV] [d]	$E_{EA,CV}$ [eV] [d]	$E_{gap,CV}$ [eV]	$E_{HOMO,DFT}$ [eV] [e]	$E_{LUMO,DFT}$ [eV] [e]	$E_{Diff,DFT}$ [eV] [e]
DBAF	550	581	2.1	572	699	21	—[f]	—[f]	—[f]	−5.0	−2.4	2.6
DBAF-N$_2$	555	582	2.1	577	687	5	—[f]	—[f]	—[f]	−5.2	−2.6	2.6
mes-DBAF	561	589	2.1	588	819	20	−5.3	−3.0	2.3	−4.9	−2.4	2.6
mes-DBAF-N$_2$	561	592	2.1	593	961	29	−5.6	−3.2	2.4	−5.1	−2.5	2.6

[a] Most-red-shifted absorption maximum. [b] **DBAF** and **DBAF-N$_2$** were measured in *o*-DCB at room temperature; **mes-DBAF** and **mes-DBAF-N$_2$** were measured in CH_2Cl_2 at room temperature. [c] Estimated from the corresponding λ_{onset} by $E_{gap,opt} = 1240/\lambda_{onset}$. [d] Cyclic voltammograms (CV) of **mes-DBAF** and **mes-DBAF-N$_2$** in dichloromethane (c = 1 mM) using $[Bu_4N][PF_6]$ (0.1 M) as electrolyte. CV scan speed 100 mV s^{-1}. $E_{IP,CV} = -(E^{Ox}_{1/2} + 4.8\ eV)$; $E_{EA,CV} = -(E^{red}_{1/2} + 4.8\ eV)$. [e] Calculated at the u-B3LYP/6-31G(d,p) level of theory. [f] Not determined due to solubility issues.

Stokes shift of $\tilde{\nu}$ = 687 cm^{-1} with φ = 5% (Table 1). Similarly, as for **mes-DBAF** and **DBAF** the spectral differences of **mes-DBAF-N$_2$** and **DBAF-N$_2$** are negligible (Fig. 2 and Table 1), indicating that the mesityl groups change the solubility without significantly influencing the optoelectronic properties of the molecular scaffolds.

As already mentioned, **DBAF** and **DBAF-N$_2$** are poorly soluble in organic solvents so that decent cyclovoltammograms could not be recorded. Therefore, only the mesitylated derivatives **mes-DBAF** and **mes-DBAF-N$_2$** have been investigated by cyclic as well as differential pulse voltammetry revealing an amphoteric redox behaviour in both cases (Fig. 3). Two reversible oxidations can be found for **mes-DBAF** at E^1_{Ox} = 0.52 V and E^2_{Ox} = 0.83 V as determined by DPV (CV: $E^{Ox,1}_{1/2}$ = 0.56 V und $E^{Ox,2}_{1/2}$ = 0.86 V) and one reversible reduction was detected at E_{red} = −1.76 V (CV: $E^{red}_{1/2}$ = −1.80 V). For **mes-DBAF-N$_2$** the corresponding oxidation waves appear at approx.

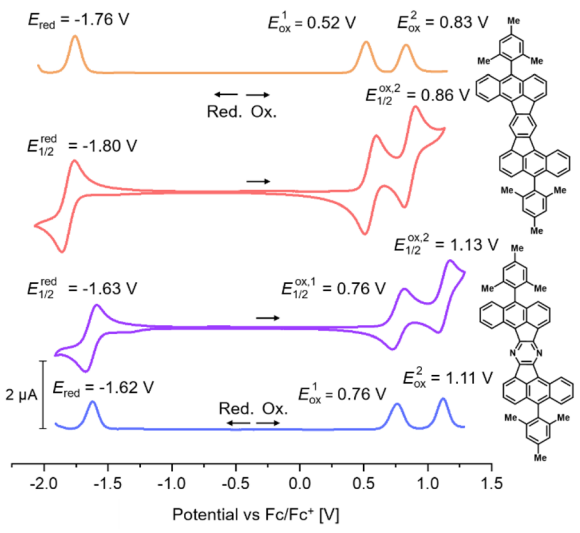

Fig. 3 Cyclic voltammograms (CV) and differential pulse voltammograms (DPV) of **mes-DBAF** (top) and **mes-DBAF-N$_2$** (bottom) in dichloromethane (c = 1 mM) using $[Bu_4N][PF_6]$ (0.1 M) as electrolyte. CV scan speed 100 mV s^{-1}; DPV: step size of 0.005 V, a modulation amplitude of 0.025 V a modulation time of 0.05 s and an interval time of 0.5 s.

0.2–0.3 V higher potentials with E^1_{Ox} = 0.76 V and E^2_{Ox} = 1.11 V (CV: $E^{Ox,1}_{1/2}$ = 0.76 V und $E^{Ox,2}_{1/2}$ = 1.13 V). The reduction is shifted by 0.14 V to higher potentials with E_{red} = −1.62 V (CV: $E^{red}_{1/2}$ = 1.63 V) indicating the electrochemical stabilization of PAHs by nitrogen substitution.[42–44] This is further displayed in the differences of the corresponding ionization potentials (**mes-DBAF**: IP = −5.32 eV; **mes-DBAF-N$_2$**: IP = −5.56 eV) as well as electron affinities (**mes-DBAF**: EA = −3.04 eV; **mes-DBAF-N$_2$**: EA = −3.18 eV) derived from this data. By UV/vis spectrsocopy it was demonstrated that the mesityl substituents, which are oriented orthogonal to the π backbone, do not significantly influence these electronically. Therefore, it is assumed that the redox behaviour of **DBAF** and **DBAF-N$_2$** are comparable to **mes-DBAF** and **mes-DBAF-N$_2$**. By DFT calculations (u-B3LYP/6-31G (d,p); Fig. 4 and Table 1) a 0.19 eV lower HOMO energy of **mes-DBAF-N$_2$** (E_{HOMO} = −5.12 eV) in comparison to **mes-DBAF** (E_{HOMO} = −4.93 eV) is found as well as a 0.14 eV lower LUMO energy (**mes-DBAF-N2**: E_{LUMO} = −2.52 eV; **mes-DBAF**: E_{LUMO} = −2.38 eV), which corroborates with the trend found by CV.

Again, the mesityl substituents seem to only have a small influence to the energy levels with the HOMOs being lowered by only 0.09–0.1 eV and the LUMOs by only 0.04–0.06 eV for **DBAF** and **DBAF-N$_2$** in comparison to their mesitylated congeners (Fig. 4 and Table 1) and the distribution of frontier molecular orbital coefficients are nearly the same for all four compounds (Fig. 4).

By thermal crystallization from *ortho*-dichlorobenzene as well as by sublimation isomorphic single crystals of **DBAF** suitable for SCXRD were obtained. **DBAF** crystallizes in the monoclinic space group $P2_1/n$ with Z = 2. The crystalline packing is dominated by slipped π-stacked molecular columns (Fig. 5b and c) with a spacing of $d_{\pi-\pi}$ = 3.33 Å propagating along the crystallographic a-axis. Edge-to-face π stacking with $d_{C-H\cdots\pi}$ = 2.70 Å and an angle of the π-systems of θ = 51.8° (Fig. 5c) leads to a herringbone like motif (Fig. 5d). Suitable crystals of **DBAF-N$_2$** have also been obtained by sublimation. **DBAF-N$_2$** also crystallized in the $P2_1/n$ space group and again slipped π-stacked columns can be found, here with a slightly larger distance of $d_{\pi-\pi}$ = 3.40 Å but with a larger overlap of two adjacent π systems (compare Fig. 5b and f). Similar edge-to-face π stacking is found but with a larger angle of θ = 73.1° and a larger

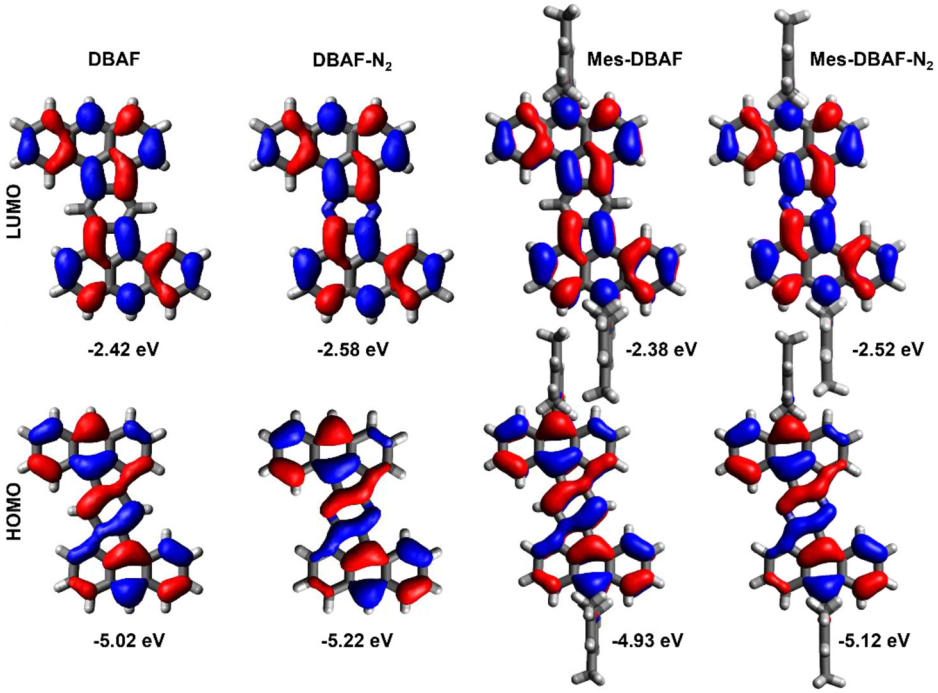

Fig. 4 DFT-calculated frontier molecular orbitals on the u-B3LYP/6-31G(d,p) level of theory (LUMOs top; HOMOs bottom) of (from left to right) **DBAF**, **DBAF-N_2**, **mes-DBAF** and **mes-DBAF-N_2** with the calculated energy levels.

distance between adjacent molecules ($d_{C-H\cdots\pi}$ = 2.87 Å), leading to a herringbone type packing as well (Fig. 5g and h). Single-crystals of **mes-DBAF** were obtained by slow evaporation of a chloroform solution and crystallized in the monoclinic space group $P2_1/n$ with Z = 2. This time with one enclathrated disordered molecule of chloroform per **mes-DBAF** (Fig. 5). Due to the almost perpendicular oriented (87.6°) mesityl groups, no direct π stacking of the DBAF central backbone is found (Fig. 5i). Instead, the crystalline packing is dominated by C–H···π-interactions of the *para*-methyl-group of a mesityl substituent with the central benzene ring of the DBAF backbone ($d_{C-H\cdots\pi}$ = 2.34 Å) leading to a loose herringbone-like arrangement with chloroform molecules in its voids (Fig. 5j–l). Crystals of **mes-DBAF-N_2** were obtained by vapor phase diffusion of n-hexane into a saturated chloroform solution. **mes-DBAF-N_2** also crystallized in the monoclinic space group $P2_1/n$ with Z = 2. In contrast to **mes-DBAF**, **mes-DBAF-N_2** shows linear columns of face-to-face π stacks along the crystallographic *a*-axis (Fig. 5n and p). Within these stacks two symmetrically independent molecules with unparallel π-planes and a shortest distance of $d_{\pi-\pi}$ = 3.22 Å are found in a rare twisted offset[45–47] with an angle of ~32° between the central molecular axes to maximize orbital overlaps by avoiding the steric repulsion of the mesityl groups. The columns themselves interact with each other by dispersion interactions between the methyl groups of the mesityl substituents.

Charge transfer integrals (t) between the molecules as well as intrinsic charge carrier mobilities (hole and electron) were calculated *via* fragment based non-adiabatic molecular dynamic simulations (for a detailed description of the method see ESI‡).[48,49] Only hole transport properties will be discussed (calculated electron transport properties can be found in the ESI‡), due to the fact, that the experimentally determined electron affinities of EA = −3.04 to −3.18 eV exclude a potential use in n-type semiconducting devices due to a mismatch with the work functions of commonly used electrode materials such as gold.[50] The hole transfer integral of **DBAF** along the axis of the face-to-face stacking was calculated using the non-self-consistent density functional tight binding (DFTB) method with special parameter set[51] to be $t_{\|,h}$ = 20 ± 14 meV (Fig. 5d). In the direction of the edge-to-face stacking only small transfer integrals were found ($t_{\perp,h}$ = 1 ± 3 meV). The corresponding theoretical hole mobility of μ_h = 0.31 $cm^2\ V^{-1}\ s^{-1}$ calculated by the fewest switches surface hopping algorithm with implicit relaxation (FSSH-IR), where the reorganization energy is calculated by DFT with B3LYP functional and 6-31G(d,p) level of theory to be $\lambda_{h,\ B3LYP}$ = 153 meV indicates the potential use of **DBAF** in such devices. In the case of **DBAF-N_2** (Fig. 5h), a higher electronic coupling with transfer integrals of $t_{\|,h}$ = 70 ± 24 meV was found. The corresponding hole mobilities of μ_h = 14.41 $cm^2\ V^{-1}\ s^{-1}$ are based on a reorganization energy of $\lambda_{h,\ B3LYP}$ = 167 meV. The mesitylated congeners **mes-DBAF** and **mes-DBAF-N_2** showed either no or only negligible theoretical mobilities and have thus been excluded for device fabrication (see ESI‡ for further details).

Organic p-channel TFTs of **DBAF** gave hole mobilities of 1 × 10^{-4} to 1 × 10^{-3} $cm^2\ V^{-1}\ s^{-1}$ independent of the type of the substrate (silicon or flexible polyethylene naphthalate (PEN))

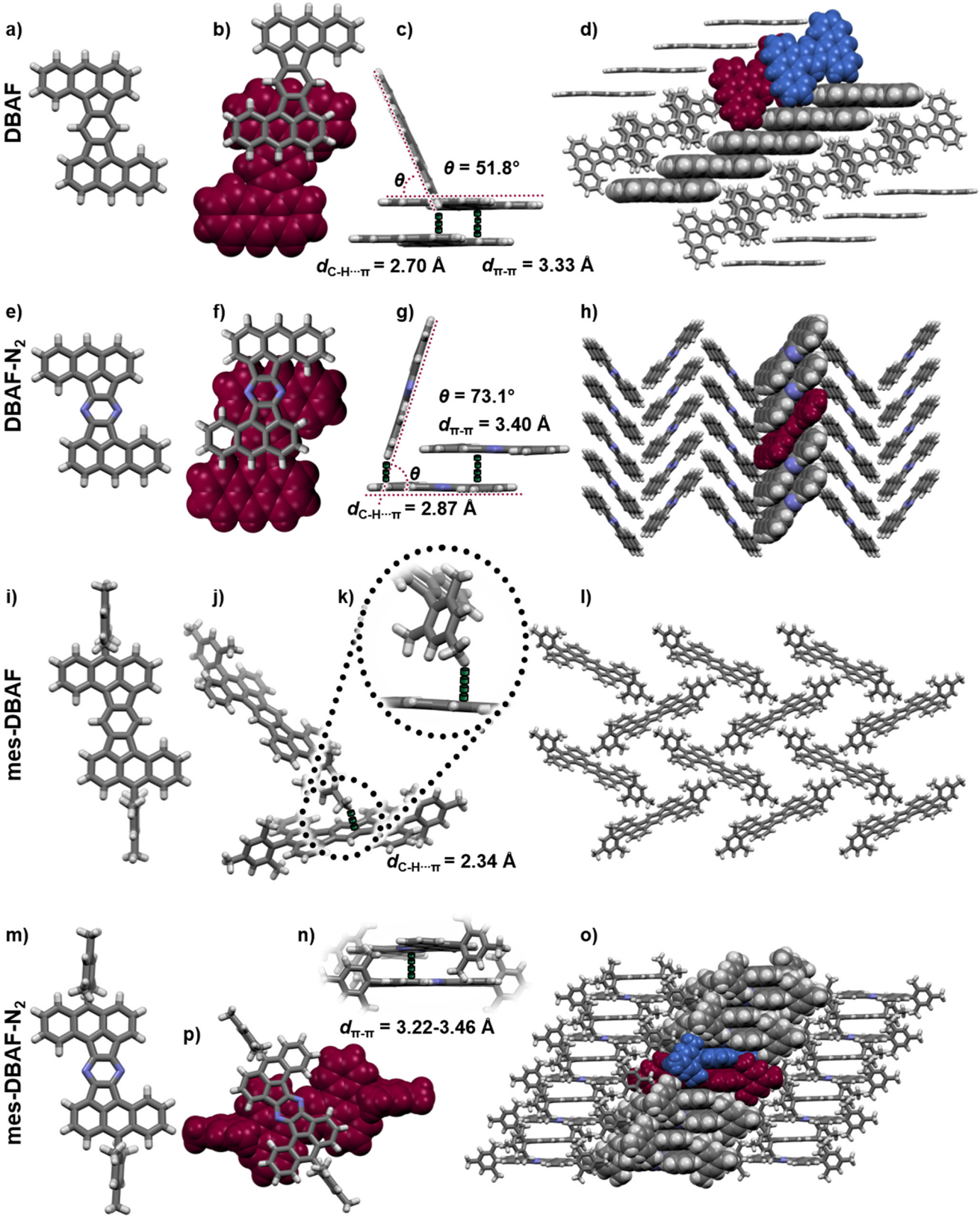

Fig. 5 Single crystal X-ray structures of **DBAF** (a–d), **DBAF-N_2** (e–h), **mes-DBAF** (i–l) and **mes-DBAF-N_2**. a, e, i and m: molecular structures. b, f and p: top-view on face-to-face π-stacked dimers. c, g and j: side-view on edge-to-face interactions. d, h, l and o: molecular packings. k: zoom-in on the C–H···π-interaction of **mes-DBAF**. n: side-view on the face-to-face π-stacked dimer of **mes-DBAF-N_2**.

and the substrate temperature during the vacuum deposition of the semiconductor (60 or 80 °C) when using a pentadecafluoro-octadecylphosphonic acid self-assembled monolayer (F-SAM) as part of the gate dielectric.[52]

These mobilities significantly increased using an *n*-tetradecylphosphonic acid SAM (H-SAM) instead. In this case, mobilities of 0.08 up to 0.4 $cm^2 V^{-1} s^{-1}$ have been obtained, again independent of the type of substrate and the substrate temperature during the semiconductor deposition. The best TFT performance was obtained on a PEN substrate using a substrate temperature of 80 °C during the semiconductor deposition (for details see ESI‡), with a mobility of $\mu_{h,exp}$ = 0.4 $cm^2 V^{-1} s^{-1}$ (Fig. 6), which is in good agreement to the theoretical mobility discussed above ($\mu_{h,theo}$ = 0.31 $cm^2 V^{-1} s^{-1}$). Although **DBAF-N$_2$** showed even higher theoretical hole mobilities ($\mu_{h,theo}$ = 14.41 $cm^2 V^{-1} s^{-1}$, see discussion above), the mobilities obtained experimentally are much smaller, only 4×10^{-5} to 5×10^{-4} $cm^2 V^{-1} s^{-1}$, independent of the type of substrate, the type of SAM, and the substrate temperature during the semiconductor deposition. The calculated values represent the intrinsic mobility in the perfect crystalline structures of **DBAF** and **DBAF-N$_2$**, where no grain boundaries or other defects are present. However, in thin-films, such defects exist, and the thin-film structures may deviate from the ideal single-crystal form. Consequently, the calculated mobilities provide a useful estimation of how closely the deposited thin-films approximate a perfect single crystal. This can be inferred from the similarity of their charge-transport properties. The significant difference between the experimental and theoretical mobilities suggests that the deposited **DBAF-N$_2$** structure deviates considerably from the perfect crystal structure.

To better understand the measured TFT characteristics (schematic device structure shown in Fig. 7a), grazing-incidence wide-angle X-ray scattering (GIWAXS) was employed. The critical angles (α_c) of **DBAF** and **DBAF-N$_2$** are estimated at 0.17° and 0.18°, respectively.[53] Therefore, the incident angle (α_i) of the incoming X-ray was set at 0.3° ($\alpha_i > \alpha_c$) in order to probe microstructures of the deeper-lying organic/SAM/inorganic interface, rather than those from the topmost surface. Though the AFM and SEM investigations reveal the polycrystallinity of the thin-films with non-specific orientations, the small grain size (~0.1–0.5 μm) makes the in-plane information difficult or impossible to be detected by GIWAXS. Instead, we obtain the strong out-of-plane signals and are thus able to analyze the interface configurations. Two sets of out-of-plane signals have been observed. As exemplified in Fig. 7c and d, the lower one at ~21 Å stems from the self-assembled monolayer that is part of the gate dielectric, while the upper one at ~10 Å belongs to the organic semiconductor thin-films. Specifically, for **DBAF**, the reflex at 9.99 Å is assigned to the (001) plane (10.5 Å calculated from the signal crystal data) and for **DBAF-N$_2$**, the reflex at 9.75 Å to the (10$\bar{1}$) plane (9.77 Å calculated from the signal crystal data). Both molecules show an edge-on orientation and a layered structure. **DBAF** stays more tilted (43°–44°) than **DBAF-N$_2$** (77°–78°) to the substrate, which could slightly lower the HOMO level. Within one layer, both **DBAF** and **DBAF-N$_2$** molecules stack in lines. The small π–π distance (**DBAF** 3.3 Å and **DBAF-N$_2$** 3.4 Å) of two adjacent molecules and a reasonable overlap of their electron clouds (~1/3 for **DBAF** and ~2/3 for **DBAF-N$_2$**) favor the horizontal charge-carrier hopping along the stack-propagating direction (Fig. 7b). This agrees with the values of the calculated transfer integrals (for **DBAF** $t_{\parallel,h}$ = 20 ± 14 meV and for **DBAF-N$_2$** $t_{\parallel,h}$ = 70 ± 24 meV). The main difference is found in the vertical perspective (parallel to the substrate surface normal) between the adjacent layers. **DBAF** shows an edge-to-face π–π-arrangement ($t_{\perp,h}$ = 1 ± 3 meV), whereas **DBAF-N$_2$** has an edge-to-edge arrangement, giving rise to a negligible overlap of the π-electron cloud of molecules stemming from different layers (Fig. 7i). Thus, the vertical charge-carrier transport in the **DBAF-N$_2$** thin-films is inefficient, leading to a larger contact resistance and thereby to a smaller effective charge-carrier mobility[54] compared to the **DBAF** TFTs. Another explanation for the substantial difference in measured charge-carrier mobilities is that unlike **DBAF**, **DBAF-N$_2$** does not form a completely closed film on the substrate surface (as indicated by the AFM images in the ESI in Fig. S74‡), which is expected to greatly impede the lateral charge transport.

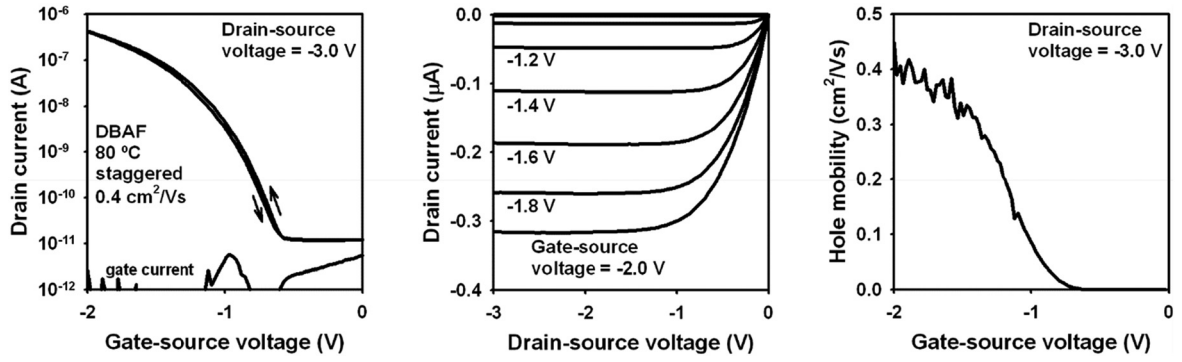

Fig. 6 Electrical characteristics of a **DBAF** TFT fabricated on a flexible PEN substrate in the inverted staggered (bottom-gate, top-contact) device architecture using an *n*-tetradecylphosphonic acid SAM as part of the gate dielectric, with the substrate held at a temperature of 80 °C during the semiconductor deposition. The effective charge-carrier mobility is 0.4 $cm^2 V^{-1} s^{-1}$.

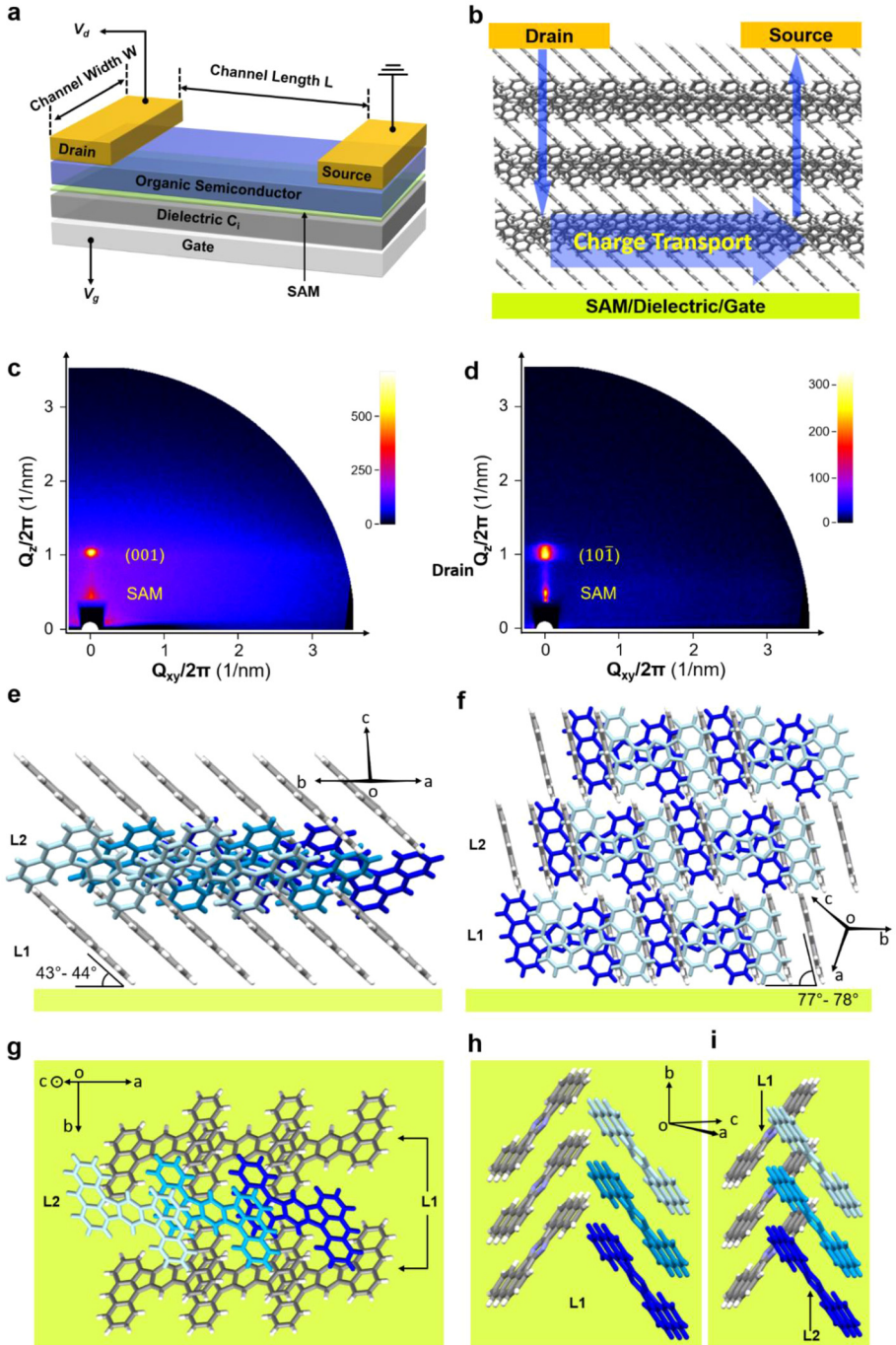

Fig. 7 Molecular orientation of **DBAF** and **DBAF-N_2** at the organic/SAM/inorganic interface of the OTFT devices. (a) The OTFT device used in this work has a bottom-gate-top-contact structure. (b) Illustration of charge transport taking place in a working device of **DBAF**. (c) and (d) are typical GIWAXS data for the **DBAF**- and **DBAF-N_2**-based devices, respectively. (e) Side view and (g) top view of the orientation of **DBAF** molecules. (f) Side view and (h and i) top views of the orientation of **DBAF-N_2** molecules. (h) shows the first layer (L1) at the SAM/inorganic substrate (bright green). (g) and (i) show the first two layers, in which molecules colored in grey come from the first layer (L1) and molecules in various blue colors are from the second layer (L2).

Conclusions

The PAHs presented in this study have a Z-shape conformation and can be tuned in terms of their solubility by peripheral substituents without influencing the electronic properties of the core structure as proven by spectroscopic methods and quantum chemical calculations. This made the investigation in solution as *e.g.* by electrochemical methods possible and revealed suitable characteristics for the application in p-type thin-film transistors. Corresponding devices of **DBAF** showed

experimental mobilities up to $\mu_{h,exp}$ = 0.4 $cm^2 V^{-1} s^{-1}$ which is in agreement to quantum chemical calculations based on single crystal X-ray structure data. A substitution of two carbon atoms in the aromatic backbone with nitrogen was possible by simple modification of the molecular precursors. While an expected stabilization of the frontier molecular orbitals was achieved and higher theoretical hole mobilities were obtained, proving the beneficial intrinsic properties of **DBAF-N_2**, the corresponding devices suffered from a disadvantageous orientation of the crystalline films on the devices' surface resulting in three orders of magnitude smaller experimental mobilities. This study shows on the one hand the potential of this class of PAHs for the application as semiconducting materials in organic electronics and on the other hand the importance of the interplay of suitable intrinsic molecular properties and the controllable device morphology upon structural changes on a molecular level.

Data availability

The data that support the findings of this study are available from the corresponding author upon reasonable request.

Conflicts of interest

There are no conflicts to declare.

Acknowledgements

All authors are grateful for financial support to this project by Deutsche Forschungsgemeinschaft (DFG) in the framework of the Collaborative Research Center SFB1249 (TP-A04, -B02, and -C01). Support by the state of Baden-Württemberg through bwHPC and the DFG through grant no. INST 40/575-1 FUGG (JUSTUS 2 cluster) is acknowledged. Jan Lennart Peters is acknowledged for assistance with synthesis. We thank the Kivala group (Heidelberg) for access to their fluorimeter for PLQY determination.

References

1 R. Zahradník, Electronic Structure and Properties of Non-Alternant Hydrocarbons, *Angew. Chem., Int. Ed. Engl.*, 1965, **4**, 1039–1050.
2 K. N. Plunkett, What About the Five-Membered Ring? Cyclopenta-fused Polycyclic Aromatic Hydrocarbons as a Building Block for Functional Materials, *Synlett*, 2013, **24**, 898–902.
3 R. G. Lawton and W. E. Barth, Synthesis of corannulene, *J. Am. Chem. Soc.*, 1971, **93**, 1730–1745.
4 A. M. Butterfield, B. Gilomen and J. S. Siegel, Kilogram-Scale Production of Corannulene, *Org. Process Res. Dev.*, 2012, **16**, 664–676.
5 X. Li, F. Kang and M. Inagaki, Buckybowls: Corannulene and Its Derivatives, *Small*, 2016, **12**, 3206–3223.
6 J. D. Wood, J. L. Jellison, A. D. Finke, L. Wang and K. N. Plunkett, Electron Acceptors Based on Functionalizable Cyclopenta[hi]aceanthrylenes and Dicyclopenta[de,mn]tetracenes, *J. Am. Chem. Soc.*, 2012, **134**, 15783–15789.
7 G. C. Kulkarni, J. L. Morales-Cruz, W. A. Hussain, I. J. Garvey and K. N. Plunkett, Electron Acceptors Based on Cyclopentannulated Tetracenes, *Synlett*, 2018, **29**, 2572–2576.
8 E. Misselwitz, J. Spengler, F. Rominger and M. Kivala, Indenoannulated Tridecacyclene: An All-Carbon Seven-Stage Redox-Amphoter, *Chem. – Eur. J.*, 2024, **30**, e202400696.
9 S. M. Elbert, A. Haidisch, T. Kirschbaum, F. Rominger, U. Zschieschang, H. Klauk and M. Mastalerz, 2,7,11,16-Tetra-tert-Butyl Tetraindenopyrene Revisited by an "Inverse" Synthetic Approach, *Chem. – Eur. J.*, 2020, **26**, 10585–10590.
10 H. Tanoguchi, T. Yuki, S. Yokokura, T. Yanase, M. Jin, H. Ito, T. Nagahama and T. Shimada, Single Crystal Growth of Cyclopenta-Fused Polycyclic Aromatic Hydrocarbon by the Naphthalene Flux Method: 2D Ambipolar Charge Transport Properties and NIR Absorption, *ACS Appl. Electron. Mater.*, 2023, **5**, 6266–6274.
11 A. Naibi Lakshminarayana, J. Chang, J. Luo, B. Zheng, K.-W. Huang and C. Chi, Bisindeno-annulated pentacenes with exceptionally high photo-stability and ordered molecular packing: simple synthesis by a regio-selective Scholl reaction, *Chem. Commun.*, 2015, **51**, 3604–3607.
12 H.-H. Hseuh, M.-Y. Hsu, T.-L. Wu and R.-S. Liu, Efficient Synthesis and Characterization of Dibenzo[a,m]rubicenes and Tetrabenzo[a,f,r,m]rubicenes, *J. Org. Chem.*, 2009, **74**, 8448–8451.
13 X. Gu, X. Xu, H. Li, Z. Liu and Q. Miao, Synthesis, Molecular Packing, and Thin Film Transistors of Dibenzo[a,m]rubicenes, *J. Am. Chem. Soc.*, 2015, **137**, 16203–16208.
14 L. Ma, Y. Han, Q. Shi and H. Huang, The design, synthesis and application of rubicene based polycyclic aromatic hydrocarbons (PAHs), *J. Mater. Chem. C*, 2023, **11**, 16429–16438.
15 H. Sakurai, T. Daiko and T. Hirao, A Synthesis of Sumanene, a Fullerene Fragment, *Science*, 2003, **301**, 1878–1878.
16 S. H. Tucker, Synthesis of fluoranthenes. Part XIII. Synthesis of benzo[1:2-a, 3:4-a′]- and of benzo[1:2-a, 4:5-a′]-diacenaphthylene, *J. Chem. Soc.*, 1958, 1462–1465.
17 L. Han, K. Ye, C. Li, Y. Zhang, H. Zhang and Y. Wang, Thermally Stable and Highly Luminescent Green Emissive Fluorophores with Acenaphtho[1,2-k]fluoranthene Cores and Aromatic Amine Groups, *ChemPlusChem*, 2017, **82**, 315–322.
18 Y.-C. Hsieh, H.-Y. Fang, Y.-T. Chen, R. Yang, C.-I. Yang, P.-T. Chou, M.-Y. Kuo and Y.-T. Wu, Zethrene and

Dibenzozethrene: Masked Biradical Molecules?, *Angew. Chem., Int. Ed.*, 2015, **54**, 3069–3073.
19 L. Shan, Z. Liang, X. Xu, Q. Tang and Q. Miao, Revisiting zethrene: synthesis, reactivity and semiconductor properties, *Chem. Sci.*, 2013, **4**, 3294–3297.
20 Z. Sun, S. Lee, K. H. Park, X. Zhu, W. Zhang, B. Zheng, P. Hu, Z. Zeng, S. Das, Y. Li, C. Chi, R.-W. Li, K.-W. Huang, J. Ding, D. Kim and J. Wu, Dibenzoheptazethrene Isomers with Different Biradical Characters: An Exercise of Clar's Aromatic Sextet Rule in Singlet Biradicaloids, *J. Am. Chem. Soc.*, 2013, **135**, 18229–18236.
21 C. Zong, X. Zhu, Z. Xu, L. Zhang, J. Xu, J. Guo, Q. Xiang, Z. Zeng, W. Hu, J. Wu, R. Li and Z. Sun, Isomeric Dibenzoheptazethrenes for Air-Stable Organic Field-Effect Transistors, *Angew. Chem., Int. Ed.*, 2021, **60**, 16230–16236.
22 R. Fittig and E. Ostermayer, Ueber das Phenanthren, einen neuen Kohlenwasserstoff im Steinkohlentheer, *Liebigs Ann. Chem.*, 1873, **166**, 361–382.
23 A. Schmitz and I. Ueber, hochsiedende Kohlenwasserstoffe des Steinkohlentheers, *Liebigs Ann. Chem.*, 1878, **193**, 115–128.
24 V. Sachweh and H. Langhals, Synthese von Reinst-Rubicen und Rubicen-Derivaten, *Chem. Ber.*, 1990, **123**, 1981–1987.
25 M. Kawamura, E. Tsurumaki and S. Toyota, Facile Synthesis of Rubicenes by Scholl Reaction, *Synthesis*, 2018, 134–138.
26 S. Toyota, S. Ban, M. Hara, M. Kawamura, H. Ikeda and E. Tsurumaki, Synthesis and Properties of Rubicene-Based Aromatic π-Conjugated Compounds as Five-Membered Ring Embedded Planar Nanographenes, *Chem. – Eur. J.*, 2023, **29**, e202301346.
27 C. H. E. Chow, Y. Han, H. Phan and J. Wu, Nitrogen-doped Heptazethrene and Octazethrene Diradicaloids, *Chem. Commun.*, 2019, **55**, 9100–9103.
28 K. Fujimoto, S. Takimoto, S. Masuda, T. Inuzuka, K. Sanada, M. Sakamoto and M. Takahashi, 5,11-Diazadibenzo[hi,qr]tetracene: Synthesis, Properties, and Reactivity toward Nucleophilic Reagents, *Chem. – Eur. J.*, 2021, **27**, 8951–8955.
29 K. Tajima, K. Matsuo, H. Yamada, N. Fukui and H. Shinokubo, Diazazethrene bisimide: a strongly electron-accepting π-system synthesized via the incorporation of both imide substituents and imine-type nitrogen atoms into zethrene, *Chem. Sci.*, 2023, **14**, 635–642.
30 Y. S. Park, D. J. Dibble, J. Kim, R. C. Lopez, E. Vargas and A. A. Gorodetsky, Synthesis of Nitrogen-Containing Rubicene and Tetrabenzopentacene Derivatives, *Angew. Chem., Int. Ed.*, 2016, **55**, 3352–3355.
31 Y. Morimoto, Y. H. Koo, K. Otsubo, H. Kitakado, S. Seki, A. Osuka and T. Tanaka, Dibenzodiazapyracylenes: Doubly N-Doped Cyclopenta-Fused Polycyclic Molecules That Exhibit High Carrier Mobility, *Angew. Chem., Int. Ed.*, 2022, **61**, e202200341.
32 H. W. H. Lai, Y. C. Teo and Y. Xia, Functionalized Rigid Ladder Polymers from Catalytic Arene-Norbornene Annulation Polymerization, *ACS Macro Lett.*, 2017, **6**, 1357–1361.
33 P. Meti, E.-S. Lee, J.-W. Yang and Y.-D. Gong, Regioselective synthesis of dipyrrolopyrazine (DPP) derivatives via metal free and metal catalyzed amination and investigation of their optical and thermal properties, *RSC Adv.*, 2017, **7**, 18120–18131.
34 B. D. Steinberg, E. A. Jackson, A. S. Filatov, A. Wakamiya, M. A. Petrukhina and L. T. Scott, Aromatic π-Systems More Curved Than C60. The Complete Family of All Indenocorannulenes Synthesized by Iterative Microwave-Assisted Intramolecular Arylations, *J. Am. Chem. Soc.*, 2009, **131**, 10537–10545.
35 M.-K. Chen, H.-J. Hsin, T.-C. Wu, B.-Y. Kang, Y.-W. Lee, M.-Y. Kuo and Y.-T. Wu, Highly Curved Bowl-Shaped Fragments of Fullerenes: Synthesis, Structural Analysis, and Physical Properties, *Chem. – Eur. J.*, 2014, **20**, 598–608.
36 T. Kubo, S. Miyazaki, T. Kodama, M. Aoba, Y. Hirao and H. Kurata, A facile synthesis of trinaphtho[3.3.3]propellane and its π-extension and the formation of a two-dimensional honeycomb molecular assembly, *Chem. Commun.*, 2015, **51**, 3801–3803.
37 Y.-C. Hsieh, T.-C. Wu, J.-Y. Li, Y.-T. Chen, M.-Y. Kuo, P.-T. Chou and Y.-T. Wu, Dinaphthozethrene and Diindenozethrene: Synthesis, Structural Analysis, and Properties, *Org. Lett.*, 2016, **18**, 1868–1871.
38 X. Tian, L. M. Roch, K. K. Baldridge and J. S. Siegel, Diindenocorannulenes: Curved Aromatics Blending Bowl-in-Bowl Assembly and Nanocarbon Material Properties, *Eur. J. Org. Chem.*, 2017, 2801–2805.
39 Y. Wang, O. Allemann, T. S. Balaban, N. Vanthuyne, A. Linden, K. K. Baldridge and J. S. Siegel, Chiral Atropisomeric Indenocorannulene Bowls: Critique of the Cahn–Ingold–Prelog Conception of Molecular Chirality, *Angew. Chem., Int. Ed.*, 2018, **57**, 6470–6474.
40 S. Seifert, D. Schmidt, K. Shoyama and F. Würthner, Base-Selective Five- versus Six-Membered Ring Annulation in Palladium-Catalyzed C–C Coupling Cascade Reactions: New Access to Electron-Poor Polycyclic Aromatic Dicarboximides, *Angew. Chem., Int. Ed.*, 2017, **56**, 7595–7600.
41 X.-Y. Wang, X. Yao and K. Müllen, Polycyclic aromatic hydrocarbons in the graphene era, *Sci. China: Chem.*, 2019, **62**, 1099–1144.
42 U. H. F. Bunz and J. Freudenberg, N-Heteroacenes and N-Heteroarenes as N-Nanocarbon Segments, *Acc. Chem. Res.*, 2019, **52**, 1575–1587.
43 T. Kirschbaum, F. Rominger and M. Mastalerz, A Chiral Polycyclic Aromatic Hydrocarbon Monkey Saddle, *Angew. Chem., Int. Ed.*, 2020, **59**, 270–274.
44 T. Kirschbaum, F. Rominger and M. Mastalerz, An Isosteric Triaza Analogue of a Polycyclic Aromatic Hydrocarbon Monkey Saddle, *Chem. – Eur. J.*, 2020, **26**, 14560–14564.
45 X. Roy, J. H. Chong, B. O. Patrick and M. J. MacLachlan, Molecular Scaffolding of Prussian Blue Analogues Using a

Phenanthroline-Extended Triptycene Ligand, *Cryst. Growth Des.*, 2011, **11**, 4551–4558.

46 L. Ueberricke, J. Schwarz, F. Ghalami, M. Matthiesen, F. Rominger, S. M. Elbert, J. Zaumseil, M. Elstner and M. Mastalerz, Triptycene End-Capped Benzothienobenzothiophene and Naphthothienobenzothiophene, *Chem. – Eur. J.*, 2020, **26**, 12596–12605.

47 L. Ueberricke, I. Ciubotaru, F. Ghalami, F. Mildner, F. Rominger, M. Elstner and M. Mastalerz, Di- and Tetracyano-Substituted Pyrene-Fused Pyrazaacenes: Aggregation in the Solid State, *Chem. – Eur. J.*, 2020, **26**, 11634–11642.

48 S. Roosta, F. Ghalami, M. Elstner and W. Xie, Efficient Surface Hopping Approach for Modeling Charge Transport in Organic Semiconductors, *J. Chem. Theory Comput.*, 2022, **18**, 1264–1274.

49 W. Xie, D. Holub, T. Kubař and M. Elstner, Performance of Mixed Quantum-Classical Approaches on Modeling the Crossover from Hopping to Bandlike Charge Transport in Organic Semiconductors, *J. Chem. Theory Comput.*, 2020, **16**, 2071–2084.

50 H. Klauk, Organic thin-film transistors, *Chem. Soc. Rev.*, 2010, **39**, 2643–2666.

51 A. Heck, J. J. Kranz, T. Kubař and M. Elstner, Multi-Scale Approach to Non-Adiabatic Charge Transport in High-Mobility Organic Semiconductors, *J. Chem. Theory Comput.*, 2015, **11**, 5068–5082.

52 U. Kraft, U. Zschieschang, F. Ante, D. Kälblein, C. Kamella, K. Amsharov, M. Jansen, K. Kern, E. Weber and H. Klauk, Fluoroalkylphosphonic acid self-assembled monolayer gate dielectrics for threshold-voltage control in low-voltage organic thin-film transistors, *J. Mater. Chem.*, 2010, **20**, 6416–6418.

53 M. Birkholz, in *Thin Film Analysis by X-Ray Scattering*, WILEY-VCH Verlag GmbH & Co. KGaA, 2006.

54 B. Peng, K. Cao, A. H. Y. Lau, M. Chen, Y. Lu and P. K. L. Chan, Crystallized Monolayer Semiconductor for Ohmic Contact Resistance, High Intrinsic Gain, and High Current Density, *Adv. Mater.*, 2020, **32**, 2002281.

Z-Shaped Polycyclic Aromatic Hydrocarbons with Embedded Five-Membered Rings and their Application in Organic Thin-Film Transistors

Sven M. Elbert,[a] Evelin Bolgert,[a] Owen T. A. Paine,[a] Farhad Ghalami,[b] Wen-Shan Zhang,[a] Ute Zschieschang,[c] Frank Rominger,[a] Dennis Popp,[a] Hagen Klauk,[c] Marcus Elstner,[b] Michael Mastalerz*[a]

a. Institute of Organic Chemistry, Ruprecht-Karls-University Heidelberg, Im Neuenheimer Feld 270, 69120 Heidelberg, Germany; E-mail: michael.mastalerz@oci.uni-heidelberg.de
b. Institute of Physical Chemistry and Theoretical Chemical Chemistry, Karlsruhe Institute of Technology, Kaiserstraße 12, D-76131, Karlsruhe, Germany
c. Max Planck Institute for Solid State Research, Heisenbergstr.1, 70569 Stuttgart, Germany

Supporting Information

Table of Contents

1. General Remarks

Materials: All used reagents, solvents and materials were purchased from Acros Organics, BLDPharm, Carbolution, Fisher Scientific/Thermo Fisher, Honeywell, Sigma-Aldrich, Grüssing, Merck or VWR Chemicals and used without further purification, if not mentioned otherwise. Compounds **1**,[S1] **2**[S2] and **4**[S3-5] were synthesized according to literature known procedures Anhydrous dichloromethane (DCM), tetrahydrofuran (THF) and toluene were dispensed from the solvent purification system MB SPS-800. Solvents were degassed by bubbling argon through it for at least 15 min. If not mentioned otherwise, all reactions were performed under standard conditions (25 °C, 1013 mbar).

Thin layer and flash column chromatography: Analytical thin layer chromatography was performed using fluorescent-labeled silica coated aluminum plates (TLC silica gel 60 F254, Merck). Detection was accomplished by using UV-light (λ_{Ex} = 254 nm).

For flash column chromatography silica gel with a particle size of 0.040–0.063 (Macherey-Nagel) and for coating 63–200 ppm (Sigma-Aldrich) was used. For chromatography, the following eluents were used: light petroleum ether (PE), ethyl acetate (EtOAc) and DCM or their mixtures.

Nuclear Magnetic Resonance Spectroscopy (NMR): NMR spectra were recorded using a Bruker Avance III 400 (^{1}H: 400 MHz, ^{13}C: 101 MHz), a Bruker Avance III 600 (^{1}H: 600 MHz, ^{13}C: 151 MHz) or a Bruker Avance Neo 700 (^{1}H: 700 MHz, ^{13}C: 171 MHz) spectrometer at 298 K unless otherwise stated. Abbreviations: s = singlet, d = doublet, t = triplet, quart = quartet, m = multiplet. Chemical shifts (δ) are given/expressed in parts per million (ppm) relative to traces of protonated solvent in $CDCl_3$ (δ_H = 7.26 ppm, δ_C = 77.2 ppm), THF-d_8 (δ_H = 3.58 ppm, δ_C = 65.6 ppm) or *o*DCB-d_4 (δ_H = 6.93 ppm, δ_C = 132.6 ppm), the coupling constants *J* are given in Hertz (Hz).

Melting points (M.p.): Melting points were measured using a Büchi M-565 melting point apparatus with a heating rate of 2.5 °C/min and are reported uncorrected.

Mass Spectrometry (MS): MS experiments were performed on a Bruker AutoFlex Speed time-of-flight spectrometer (MALDI-TOF-MS), DCTB (trans-2-[3-(4-*tert*-Butylphenyl)-2-methyl-propenylidene)malononitrile) was used as matrix.

Fourier-Transformation Infrared (FTIR) Spectroscopy: IR spectra were recorded using a Bruker Lumos Fourier transformation spectrometer with a Zn/Se ATR crystal. The signal intensities were described as followed: s (strong), m (medium), w (weak) and br (broad).

UV-Vis and fluorescence spectroscopy: UV-vis absorption spectra have been recorded using a Jasco V-730 spectrophotometer. Molar extinction coefficients (ε) were calculated by absorption measurements of five different concentrated solutions prepared by standard addition method. Fluorescence spectroscopy was done using a Jasco FP-8300 fluoro spectrometer and fluorescence quantum yield were determined applying direct methods[S6] using a Jasco FP-8500 Fluorescence Spectrometer with a Jasco ILF-835 (100 mm) integrating sphere. The data obtained was interpreted with Spectra Manager from Jasco.

Elemental Analysis (EA): Elemental analyses were measured in the Microanalytical Laboratory of the University of Heidelberg using an Elementar *vario MICRO cube* Element Analyzer.

Single crystal X-ray diffraction analysis: The crystal structures was measured on a Bruker APEX II (λ_{Mo}-K_α = 0.71073 Å) or a STOE Stadivari (λ_{Cu}-K_α = 1.54178 Å) diffractometer and a PILATUS detector. Data processing and absorption correction (X-Area LANA 1.83.8.0) was done by standard methods.[S7] The structures were solved with SHELXT-2014[S8] and refined using the SHELXL-2018/3[S9, 10] software.

Electrochemical Investigations: Cyclovoltammetry (CV) and Differential Pulse Voltammetry (DPV) spectra were recorded on a Metrohm Autolab PGSTAT101 potentiostat using a Pt working electrode (0.78 mm^2), a Pt counter electrode and an Ag/Ag+ pseudo reference electrode in degassed HPLC-grade CH_2Cl_2. Ferrocene was used as an internal standard for calibration. Cyclic voltammograms (CV) were obtained at a scan rate of 0.1 Vs^{-1} and differential pulse voltammograms (DPV) were obtained with a step size of 0.005 V, a modulation amplitude of 0.025 V a modulation time of 0.05 s and an interval time of 0.5 s.

GIWAXS: Grazing-Incidence Wide-Angle X-ray Scattering (GIWAXS) was performed on Rigaku SmartLab diffractometer operated at 9 kW and equipped with a HyPix-3000 detector. Visualization and data evaluation was accomplished using the Rigaku SmartLab Studio II software.

2. Synthetic Procedures

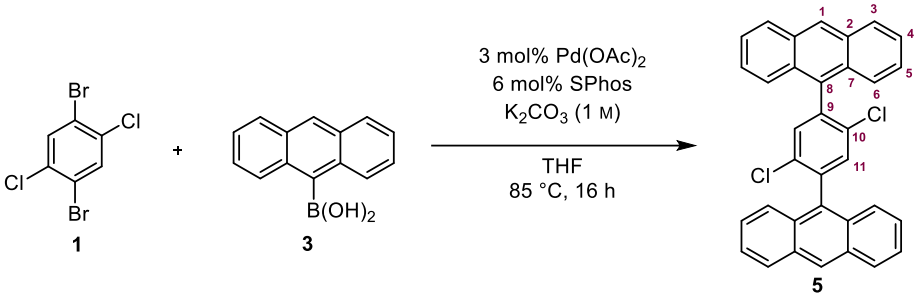

A screw-capped vial was charged with 1,4-dibromo-2,5-dichlorobenzene **1**[S1] (610 mg, 2.0 mmol) and 9-anthracene boronic acid **3** (1.78 g, 8.0 mmol) and purged with argon. Degassed tetrahydrofuran (8 mL) and a degassed aqueous K_2CO_3 solution (1 M, 8 mL) were added and the reaction mixture stirred. $Pd(OAc)_2$ (13.5 mg, 60.0 µmol, 3 mol%) and SPhos (49.3 mg, 120.0 µmol, 6 mol%) were added, the vial was sealed, and the reaction mixture vigorously stirred at 85 ◦C overnight. After cooling to room temperature, the orange precipitate was separated by filtration, washed with hot methanol (50 mL) and recrystallized from 1,2-dichlorobenzene (80 mL). The precipitate was isolated by filtration, rinsed with methanol and dried under airflow to give compound **5** as an off-white powder with a greenish tint in 80% yield (816 mg, 1.6 mmol).

M. p.: 380 °C (dec.).

^{1}H-NMR (400 MHz, *o*-DCB-*d*$_4$, 343 K): δ = 8.44 (s, 2H, H-1), 7.97 (d, *J* = 7.3 Hz, 4H, H-5), 7.81 (d, *J* = 8.3 Hz, 4H, H-4), 7.68 (s, 2H, H-11), 7.42-7.37 (m, 8H, H-3, 6). ppm.

^{13}C-NMR (101 MHz, *o*-DCB-*d*$_4$, 343 K): δ =134.3 (C_{quart}), 134.0 (C-11), 131.7 (C_{quart}), 128.9 (C-3), 128.2 (C-1), 125.8 (C-4,5,6), 125.5 (C-4,5,6) ppm.

Note: Due to the low solubility of compound **5**, the signal-to-noise ratio does not allow further assignment, especially due to overlap with dominant solvent signals (see Figure S2).

MS (HR-MALDI$^+$): *m/z* calculated for $[M]^+$: 498.094, found: 498.087.

FTIR (neat, ATR): $\tilde{\nu}$ = 3063 (w), 3003 (w), 2957 (w), 2918 (w), 2856 (w), 1954 (w), 1718 (w), 1610 (w), 1568 (w), 1520 (w), 1485 (w), 1441 (m), 1410 (w), 1379 (m), 1327 (w), 1238 (w), 1194 (w), 1148 (w), 1122 (w), 1082 (m), 1026 (w), 960 (w), 939 (m), 901 (w), 883 (w), 847 (m), 795 (w), 770 (vs), 704 (w), 687 (w), 667 (m), 613 (w) cm^{-1}.

UV-Vis (oDCB): λ_{abs} = 335, 351, 370, 391 nm.

Emission (DCM): $\lambda_{em}(\lambda_{ex})$ = 399 (351), 418 nm

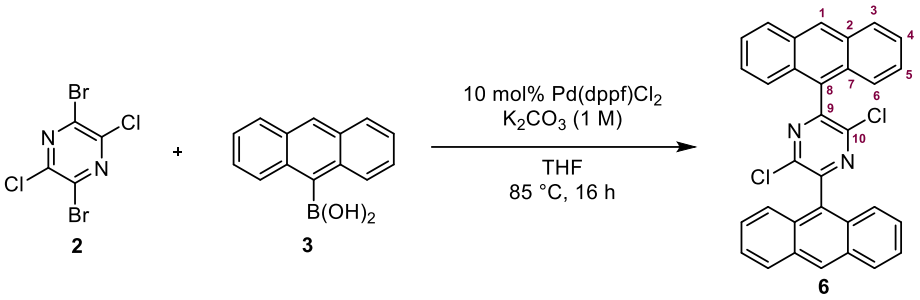

A screw-capped vial was charged with 2,5-dibromo-3,6-dichloropyrazine **2**[S2] (460 mg, 1.5 mmol) and 9-anthracene boronic acid **3** (1.33 g, 6.0 mmol) and purged with argon. Degassed tetrahydrofuran (6 mL) and a degassed aqueous solution of K_2CO_3 (1 M, 6 mL) were added and the mixture was stirred. $Pd(dppf)Cl_2$ (110 mg, 150.0 µmol, 10 mol%) was added against an argon flow, and the vial was sealed. The mixture was vigorously stirred at 85 ◦C overnight. After cooling to room temperature, the orange precipitate was isolated by filtration and washed with hot methanol (40 mL) before recrystallization from of 1,2-dichlorobenzene (45 mL). The solids were separated by filtration, rinsed with methanol, and dried under air flow to give **6** in 56% yield as a pale yellow crystalline powder (425 mg, 846.7 µmol).

M. p.: >400 °C (dec.).

^{1}H-NMR (700 MHz, DMSO-d_6, 393 K): δ = 8.89 (s, 2H, H-1), 8.28 (d, J = 8.3 Hz, 4H, H-3), 7.81 (d, J = 8.5 Hz, 4H, H-6), 7.67 (m, 8H, H-4/5) ppm.

^{13}C-NMR (171 MHz, DMSO-d_6, 393 K): δ = 150.7 (C-9), 147.1 (C-10), 130.3 (C-2), 129.0 (C-7), 128.7 (C-1), 128.2 (C-3), 127.5 (C-8), 126.7 (C-5), 125.0 (C-4), 124.2 (C-6) ppm.

MS (HR-MALDI$^+$): *m/z* calculated for $[M]^+$: 500.085, found: 500.121.

FTIR (neat, ATR): $\tilde{\nu}$ = 1622 (w), 1576(w), 1526 (w), 1506 (vw), 1431 (m), 1394 (w), 1362 (w), 1346 (w), 1286 (w), 1248 (w), 1221 (m), 1182 (w), 1159 (m), 1142 (s), 1099 (m), 1011 (m), 978 (w), 960 (w), 945 (w), 924 (m), 910 (w), 885 (m), 860 (m), 837 (w), 783 (s), 758 (m), 725 (vs), 692 (m), 669 (w), 631 (w), 609 (w) cm^{-1}.

UV-Vis (DCM): λ_{abs} (log(ε)) = 256 (5.21), 348 (3.80), 370 (4.00), 388 (4.02) nm.

Emission (DCM): λ_{em}(λ_{ex}) = 416 (255), 488, 530 (sh) nm

Elemental Analysis calculated for $C_{32}H_{18}Cl_2N_2 \cdot 1/2H_2O$: C (75.30%), H (3.75%), N (5.49%), found: C (75.08%), H (3.71%), N (5.34%).

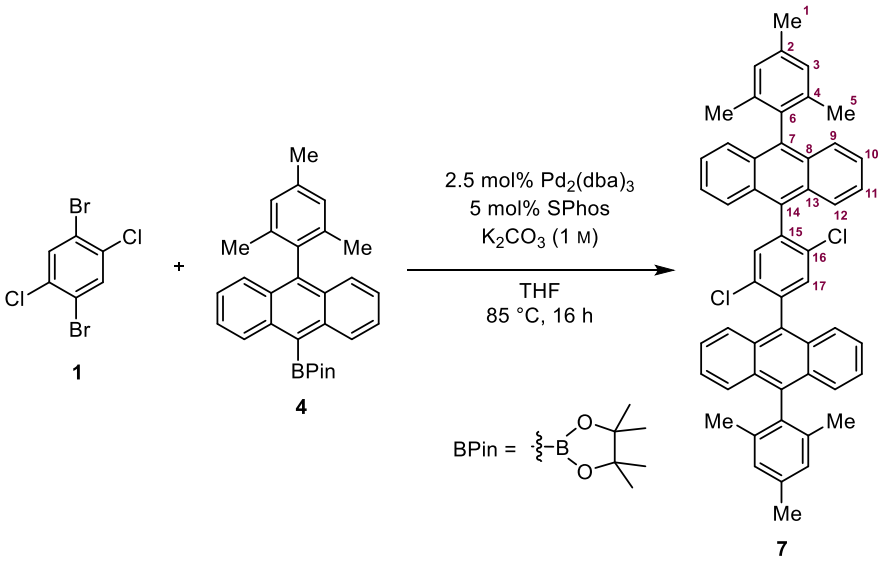

A screw-capped vial was charged with 1,4-dibromo-2,5-dichlorobenzene **1** (61.0 mg, 200 µmol), boronic acid ester **4**[S3-5] (338 mg, 800 µmol), $Pd_2(dba)_3$ (4.6 mg, 5.00 µmol, 2.5 mol%) and SPhos (8.2 mg, 20.0 µmol, 5 mol%) under argon atmosphere. Degassed THF (1 mL) and a degassed K_2CO_3 solution were added (aq, 1 M, 1mL) and the reaction mixture stirred at 85 °C for 16 h. After cooling to room temperature, DCM (10 mL) and water (5 mL) were added, the phases were separated, and the aqueous phase was extracted with DCM (3×5 mL). The combined organic phase was dried over $MgSO_4$, and the solvent was removed *in vacuo*. The crude product was washed with MeOH (20 mL) and filtered through a short plug of silica gel (5 cm) eluting with light petroleum ether first followed by a wash down of the product with DCM and a solvent removal under reduced pressure. The product was suspended in hot n-pentane (60 mL), filtered and dried on a Kugelrohr oven (150 °C, 3.2×10^{-2} mbar) overnight to give **7** in 34% yield as colorless powder (51.0 mg, 69.3 µmol).

M.p.: 385-388 °C (dec.).

^{1}H NMR (400 MHz, 323 K, $CDCl_3$): δ = 7.84 (s, 2H, H-17), 7.82 (d, *J* = 8.8 Hz, 4H, H-12), 7.63 (d, *J* = 8.7 Hz, 4H, H-9), 7.58-7.52 (m, 4H, H-11), 7.45-7.38 (m, 4H, H-10), 7.15 (s, 4H, H-3), 2.50 (s, 6H, H-1), 1.84 (s, 6H, H-5), 1.81 (s, 6H, H-5) ppm.

^{13}C-NMR (101 MHz, 323K, $CDCl_3$): δ = 139.2 (C-15), 137.7 (C-2/4), 137.5 (C-2/4), 137.4 (C-7), 137.3 (C-2/4), 134.6 (C-6), 134.1 (C-16), 133.9 (C-17), 131.8 (C-14), 129.9 (C-13), 129.6 (C-8), 128.4 (C-3), 128.3 (C-3), 126.5 (C-9), 126.2 (C-12), 126.0 (C-11), 125.4 (C-10), 21.1 (C-1), 20.0 (C-5), 19.9 (C-5) ppm.

MS (HR-MALDI$^+$, DCTB): *m/z* calculated for $[M]^+$: 734.251, found: 734.235.

FTIR (neat, ATR): $\tilde{\nu}$ = 3063 (vw), 3007 (vw), 2959 (w), 2918 (w), 2856 (vw), 615 (w), 883 (w), 1379 (m), 1082 (m), 1026 (w), 1441 (w), 939 (w), 847 (m), 770 (vs), 687 (w), 669 (w), 1610 (w) cm^{-1}.

UV-Vis (DCM): λ_{abs} (log ε) = 258 (5.11), 338 (3.83), 357 (4.08), 376 (4.33), 397 nm (4.39).

Emission (DCM, 298 K): λ_{em} (λ_{ex}) = 405 (254), 427, 452 nm.

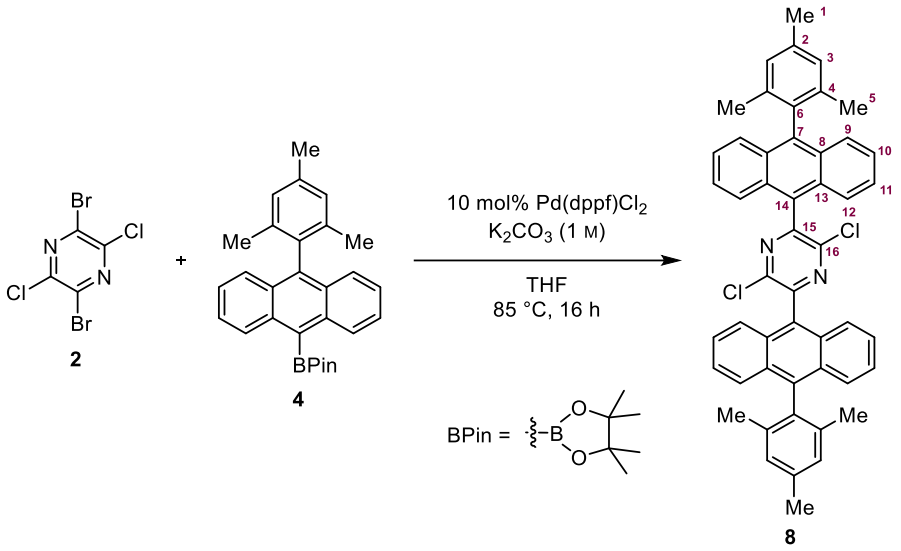

A screw-capped vial was charged with 1,4-dibromo-2,5-dichlorobenzene **2** (61.4 mg, 200 µmol) and boronic acid ester **4**[S3-5] (338 mg, 800 µmol), and purged with argon. Degassed tetrahydrofuran (1 mL) and a degassed potassium carbonate solution (1 M, 1 mL) were added and the mixture was stirred before $Pd(dppf)Cl_2$ (14.6 mg, 20 µmol, 10 mol%) was added against argon flow. The vial was sealed and stirred vigorously at 85 ◦C overnight. After cooling to room temperature, the solids formed were separated by filtration and washed with hot methanol (10 mL) before recrystallization from 1,2-dichlorobenzol (5 mL). The solids were separated by filtration, rinsed with methanol and dried under airflow to give **8** as an orange powder in 68% yield (100 mg, 136 µmol).

M.p.: 358 °C (dec.).

^{1}H NMR (400 MHz, 323 K, $CDCl_3$): δ = 7.68 (d, J = 8.1 Hz, 4H, H-12), 7.63 (d, J = 6.8 Hz, 4H, H-9), 7.60 (d, J = 16.4 Hz, 4H, H-11), 7.44 (d, J = 16.5 Hz, 4H, H-10), 7.15 (s, 4H, H-3), 2.50 (s, 6H, H-1), 1.82 (s, 12H, H-5) ppm.

^{13}C-NMR (101 MHz, 323 K, $CDCl_3$): δ = 152.6 (C-15), 149.0 (C-16), 139.5 (C-7), 137.8 (C-2/4), 137.8 (C-2/4), 137.7 (C-2, 4), 134.5 (C-6), 130.2 (C-13), 129.9 (C-8), 128.6 (C-3), 128.2 (C-14), 127.2 (C-9), 127.1 (C-9), 125.9 (C-10), 125.2 (C-12), 21.4 (C-1), 20.3 (C-5), 20.1 (C-5) ppm.

MS (HR-MALDI$^+$, DCTB): *m/z* calculated for $[M]^+$: 736.241, found: 736.291.

FTIR (neat, ATR): $\tilde{\nu}$ = 3061 (vw), 3015 (vw), 2962 (vw), 2916 (w), 2854 (vw), 1610 (w), 1564 (vw), 611 (w), 706 (w), 1290 (m), 889 (w), 760 (vs), 1107 (m), 1339 (w), 947 (m), 1022 (w), 845 (m), 1134 (m), 1269 (m), 662 (s), 1439 (w) cm^{-1}.

UV-Vis (DCM): λ_{abs} (log ε) = 255 (5.24), 355 (4.11), 374 (4.30), 396 nm (4.34).

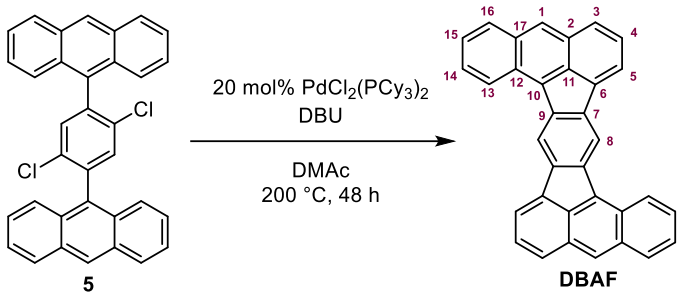

5 **DBAF**

Dichloride **5** (99.9 mg, 200 µmol) and $PdCl_2(PCy_3)_2$ (29.5 mg, 40.0 µmol, 20 mol%) were suspended in degassed *N,N*-dimethylacetamide (DMAc) (2.5 mL) under argon atmosphere. DBU (0.48 mL, 3.22 mmol) was added dropwise to the solution and the reaction mixture was stirred for 48 h at 200 °C. After cooling the mixture to room temperature, MeOH (5 mL) was added. The suspension was filtered and the precipitate washed with MeOH (20 mL). The crude product was purified by recrystallization from *o*-DCB to give 81.9 mg (192 µmol, 96%) of **DBAF** as red crystals. For further purification **DBAF** can be sublimed at a Kugelrohr oven ($<1\times10^{-3}$ mbar, 300 °C) over several days.

M.p.: 365-368 °C (dec.).

^{1}H NMR (600 MHz, o-DCB-d_4, 323 K,): δ = 9.02 (s, 2H, H-8), 8.99 (d, *J* = 8.6 Hz, 2H, H-13), 8.32 (s, 2H, H-1), 8.10 (d, *J* = 6.6 Hz, 2H, H-5), 8.06 (d, *J* = 8.4 Hz, 2H, H-16), 7.94 (d, *J* = 8.3 Hz, 2H, H-3), 7.72-7.68 (m, 2H, H-14), 7.64 (dd, *J* = 8.3, 6.5 Hz, 2H, H-4), 7.50-7.46 (m, 2H, H-15). ppm.

^{13}C-NMR (101 MHz, o-DCB-d_4, 323 K): δ = 139.6 (C_{quart}), 139.4 (C_{quart}), 137.6 (C_{quart}), 131.30 (C-16), 128.06 (C-14), 128.06 (C-1), 127.9 (C-3), 127.8 (C-4) 125.3 (C-15), 124.8 (C-13), 120.7 (C-5), 117.8 (C-8) ppm.

Note: Due to the low solubility of compound **DBAF**, the signal to noise ratio does not allow further signal assignment, especially due to overlap with dominant solvent signals (see Figure S26).

MS (HR-MALDI$^+$): *m/z* calculated for $[M]^+$: 426.141, found: 426.149.

FTIR (neat, ATR): $\tilde{\nu}$ = 3063 (w), 3036 (w), 1940 (vw), 1913 (w), 1892 (vw), 1855 (vw), 1799 (w), 1778 (vw), 1744 (w), 1707 (vw), 1676 (vw), 1624 (w), 1583 (w), 1526 (w), 1462 (m), 1439 (m),

1420 (m), 1375 (w), 1354 (w), 1331 (w), 1254 (w), 1217 (w), 1178 (w), 1157 (m), 1113 (w), 1078 (w), 1018 (w), 957 (w), 926 (w), 899 (w), 866 (vs), 833 (m), 798 (w), 773 (s), 744 (m), 729 (s), 708 (vs), 667 (m), 633 (w), 609 (w) cm^{-1}.

UV-Vis (DCM) λ_{abs} (log ε) = 340 (4.31), 350 (4.50), 378 (3.83), 460 (3.92), 495 (4.13), 520 (4.04), 556 (3.82, sh) nm.

Emission (DCM) λ_{em}(λ_{ex}) = 570 nm (351).

Elemental Analysis calculated for $C_{34}H_{18}$: C (95.86%), H (4.14%), found: C (95.70%), H (4.21%).

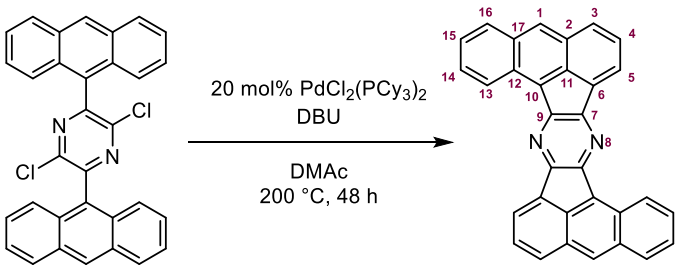

6 **DBAF-N_2**

Dichloride **6** (100 mg, 200 µmol) and $PdCl_2(PCy_3)_2$ (30 mg, 40.0 µmol, 20 mol%) were suspended in degassed *N,N*-dimethylacetamide (DMAc) (2.5 mL) under argon atmosphere. DBU (0.48 mL, 3.22 mmol) was added dropwise to the solution and the reaction mixture was stirred for 48 h at 200 °C. After cooling to room temperature, MeOH (15 mL) was added to the solution and stirred until a precipitate formed. The precipitate was isolated by filtration and washed with MeOH (10 mL). The crude product was purified by recrystallization from *o*-DCB to give 47.0 mg (110 µmol, 55%) of **DBAF-N_2** as red crystals. For further purification **DBAF-N_2** can be sublimed at a Kugelrohr oven (<1×10^{-3} mbar, 300 °C) over several days.

M.p.: >400 °C.

^{1}H NMR (*o*-DCB-d_4, 700 MHz, 393 K): δ = 9.79 (d, *J* = 8.47 Hz, 2H), 8.47 (d, *J* = 6.58 Hz, 2H), 8.44 (s, 2H, H-1), 8.04 (t, *J* = 7.74 Hz, 4H), 7.72 (t, *J* = 7.46 Hz, 2H), 7.69 (t, *J* = 7.46 Hz, 2H), 7.49 (t, *J* = 7.49 Hz, 2H) ppm.

^{13}C NMR (*o*-DCB-d_4, 171 MHz, 393 K): δ = 151.9, 150.8, 134.5, 133.3, 130.6, 129.2, 127.9, 125.9, 125.5, 123.2 ppm.

Note: Due to the low solubility of compound **DBAF-N_2** , the signal to noise ratio does not allow further assign carbon nuclei even at 171 MHz and 10240 scans, especially due to overlap with dominant solvent signals (see Figure S32).

MS (HRMALDI+) *m/z* calculated for M+: 428.131, found: 428.219;

FTIR (neat, ATR) $\tilde{\nu}$ = 1454 (w), 1443 (w), 1313 (w), 1271 (m), 1259 (m), 1134 (w), 1109 (m), 1013 (w), 947 (w), 883 (w), 841 (w), 783 (m), 731 (vs), 702 (w), 677 (w), 629 (w).

UV-Vis (DCM) λ_{abs} (log ε) =375 (4.28), 400 (4.22), 468 (3.77) nm.

Emission (DCM) λ_{em}(λ_{ex}) 577 nm (374).

Elemental Analysis calculated for $C_{32}H_{16}N_2 \cdot H_2O$: C (86.28%), H (4.06%), N (6.27%), found: C (86.33%), H (3.94%), N (6.31%)

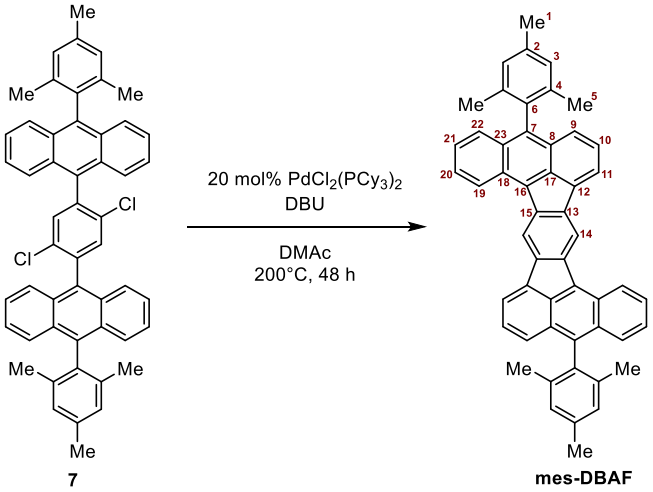

Dichloride **7** (39.8 mg, 50.0 µmol) and $PdCl_2(PCy_3)_2$ (7.4 mg, 10.0 µmol, 20 mol%) were dissolved in degassed *N,N*-dimethylacetamide (DMAc) (2 mL) under argon atmosphere. DBU (0.12 mL, 806 µmol) was added dropwise to the solution and the reaction mixture was stirred for 48 h at 200 °C. After cooling to room temperature, DCM (100 mL) was added, the phases separated and the organic phase washed with water (2×100 mL) and brine (2×100 mL) and dried over $MgSO_4$. The solvent was removed under reduced pressure. The crude product was purified by column chromatography (SiO_2, PE/DCM 15:1, R_f = 0.43, 0.34 (**mes-DBAF**), 0.00).and washed with warm n-pentane (60 mL). Drying on a Kugelrohr oven (150 °C, 1.5×10^{-1} mbar) over night gave **mes-DBAF** (11.0 mg, 16.6 µmol, 33%) as a red solid.

M.p.: 379-382 °C (dec.).

^{1}H NMR (400 MHz, 323 K, $CDCl_3$): δ = 9.07-9.03 (m, 4H, H-14/H-19), 8.25 (dd, *J* = 6.5, 0.7 Hz, 2H, H-11), 7.78-7.74 (m, 2H, H-20), 7.74-7.71 (m, 2H, H-22), 7.63-7.60 (m, 2H, H-10), 7.53 (d, *J* = 8.5 Hz, 2H, H-9), 7.46-7.41 (m, 2H, H-21), 7.13 (s, 4H, H-3), 2.49 (s, 6H, H-1), 1.83 (s, 12H, H-5) ppm.

^{13}C-NMR (101 MHz, 323 K, $CDCl_3$): δ = 139.2 (C_{quart}), 139.1 (C_{quart}), 138.4 (C-7), 137.8 (C_{quart}), 137.7 (C_{quart}), 137.4 (C_{quart}), 134.0 (C-6), 132.5 (C-23), 131.3 (C-17), 131.1 (C_{quart}), 129.4 (C_{quart}), 128.1 (C-3/22), 128.1 (C-3/22), 127.4 (C-10), 127.2 (C-20), 127.0 (C-), 126.0 (C-9), 125.1 (C-21), 124.8 (C-19), 120.1 (C-11), 117.2 (C-14), 21.1 (C-1), 20.2 (C-5) ppm.

Note: Due to overlapping signals in 2-dimensional NMR measurements, the quaternary carbon nuclei could not be further assigned.

MS (HR-MALDI$^+$, DCTB): *m/z* calculated for $[M]^+$: 662.297, found: 662.258.

IR (neat, ATR): $\tilde{\nu}$ = 2986 (m), 2972 (m), 2908 (m), 1462 (m), 1439 (m), 1379 (m), 1076 (s), 1030 (m), 878 (m), 852 (m), 812 (m), 781 (s), 760 (s), 712 (s), 681 (vs) cm^{-1}.

UV-Vis (DCM): λ_{abs} (log ε) = 248 (4.84), 350 (4.55), 493 (4.23), 526 (4.21), 563 (4.09) nm.

Emission (DCM, 298 K): λ_{em} (λ_{ex}) = 588 , 630 (493) nm.

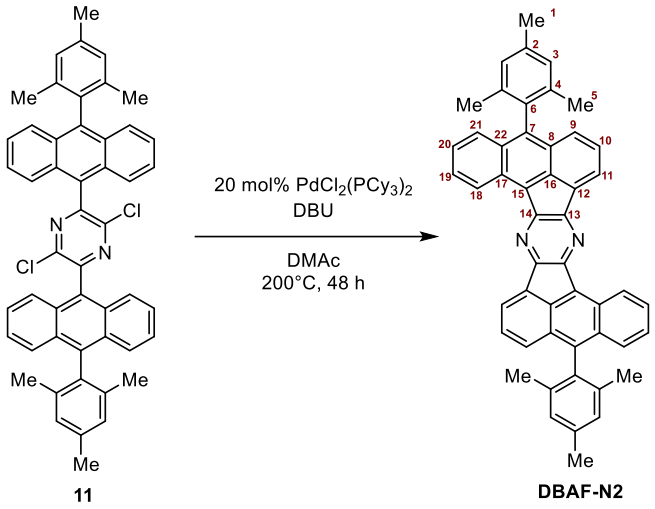

Dichloropyrazine **11** (73.7 mg, 100 µmol) and $PdCl_2(PCy_3)_2$ (14.8 mg, 20.0 µmol, 20 mol%) were dissolved in degassed *N,N*-dimethylacetamide (DMAc) (1 mL) under argon atmosphere. DBU (0.24 mL, 1.61 mmol) was added dropwise to the solution and the reaction mixture was stirred for 48 h at 200 °C. After cooling the mixture to room temperature, the solution was diluted with DCM (100 mL), washed with water (2×100 mL) and brine (2×100 mL), dried over $MgSO_4$ and the solvent was removed under reduced pressure. The crude product was purified by column chromatography (SiO_2, PE/EA 20:1, R_f = 0.50, 0.26 (**DBAF-N2**), 0.19, 0.00) and dried on a Kugelrohr oven (150 °C, 1.6×10^{-3} mbar) for 6 h to give **DBAF-N2** in 69% yield (45.9 mg, 69 µmol) as a red solid.

M.p.: 380 °C (dec.).

^{1}H NMR (THF-d_8, 600MHz, 323 K): δ = 9.85 (d, *J* = 8.5 Hz, 2H, H-18), 8.60 (d, *J* = 6.4 Hz, 2H, H-11), 7.81 (ddd, *J* = 8.3, 6.4, 1.1 Hz, 2H, H-19), 7.77 (dd, *J* = 8.6, 6.4 Hz, 2H, H-10), 7.71 (t, *J* = 7.9 Hz, 4H, H-21/9), 7.51 (ddd, *J* = 8.8, 6.4, 1.3 Hz, 2H, H-20), 7.16 (s, 4H, H-3), 2.47 (s, 6H, H-1), 1.82 (s, 12H, H-5) ppm.

^{13}C NMR (THF-d_8, 151MHz, 323 K): δ = 152.0 (Cq-14/16), 151.0 (Cq-12), 141.3 (Cq-7/8/22), 137.9 (Cq-2), 137.5 (Cq-6), 133.9 (Cq-13), 133.7 (Cq-4), 132.6 (Cq-17), 130.7 (Cq-7/8/22), 130.2 (Cq-15), 128.4 (C-3), 128.4 (C-21/9), 128.3 (C-19), 128.0 (C-10), 127.4 (C-21/9), 126.7 (Cq), 126.7 (Cq), 126.4 (C-18), 126.4 (C-20), 123.2 (C-11), 20.6 (C-1), 19.7 (C-5) ppm.

MS (HR-MALDI$^+$, DCTB): *m/z* calculated for $[M]^+$: 664.288, found: 664.272.

IR (neat, ATR): $\tilde{\nu}$ = 3061 (w), 2988 (m), 2970 (m), 2914 (m), 2860 (w), 1610 (w), 1379 (m), 1433 (s), 1416 (m), 638 (m), 1171 (m), 1269 (w), 725 (vs), 1157 (s), 1128 (m), 1302 (m), 1022 (m), 986 (m), 928 (m), 849 (s), 816 (m), 781 (s), 760 (s), 1215 (m), 681 (s), 1572 (m) cm^{-1}.

UV-Vis (DCM): λ_{abs} (log ε) = 251 nm (4.83), 372 (4.50), 400 (4.52), 468 (4.06), 528 (4.01), 565 (3.88) nm.

Emission: (DCM, 298 K) λ_{em} (λ_{ex}) = 594, 642 (400) nm.

3. NMR Spectroscopy

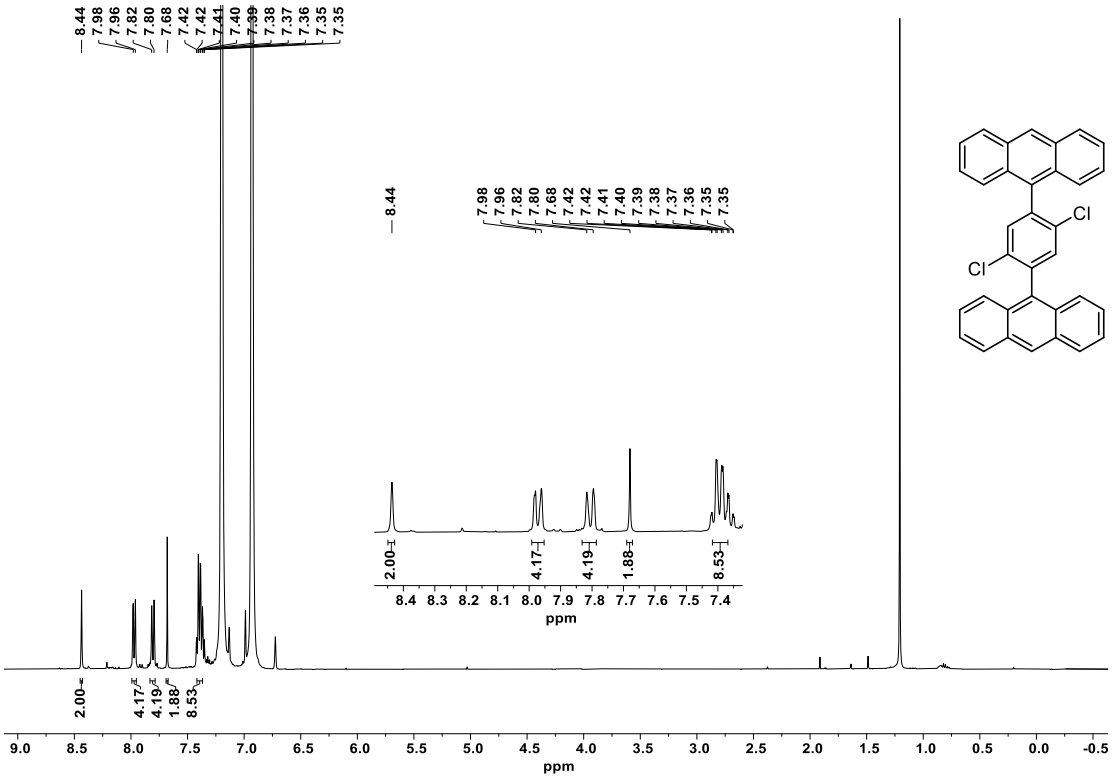

Figure S1: ^{1}H NMR spectrum of compound **5** (400 MHz, 343 K, *o*-DCB-d_4).

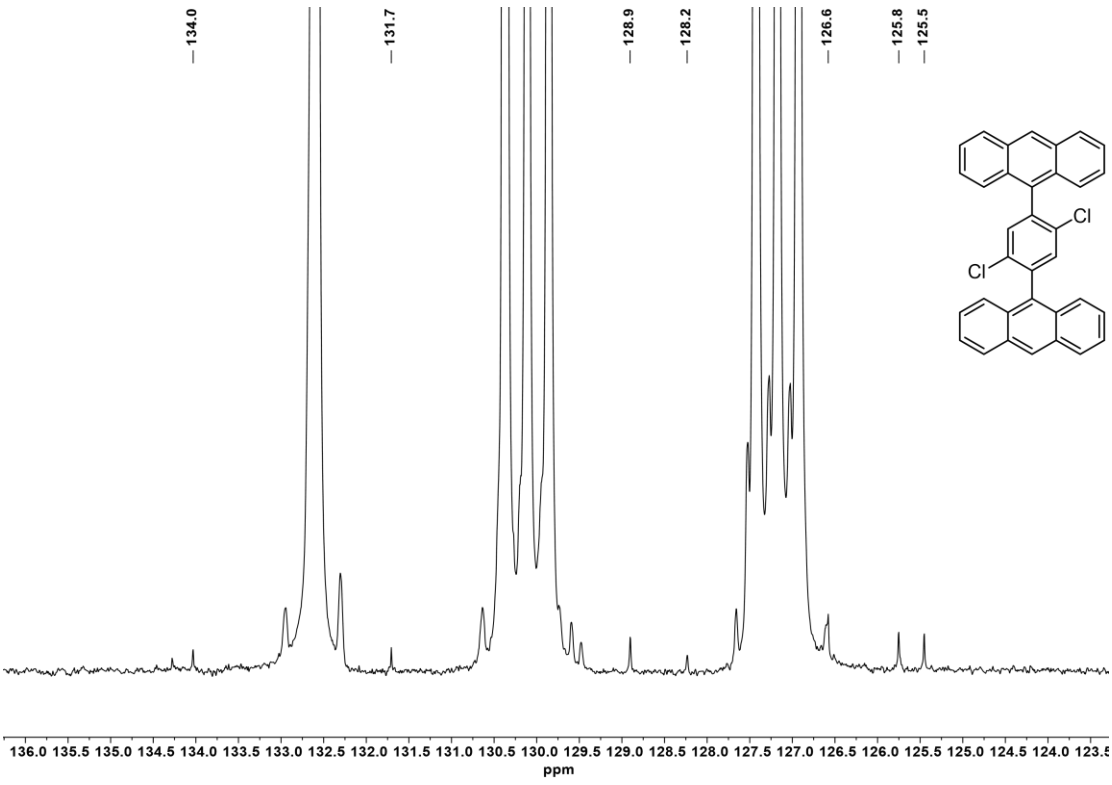

Figure S2: ^{13}C NMR spectrum of compound **5** (101 MHz, 343 K, *o*-DCB-d_4).

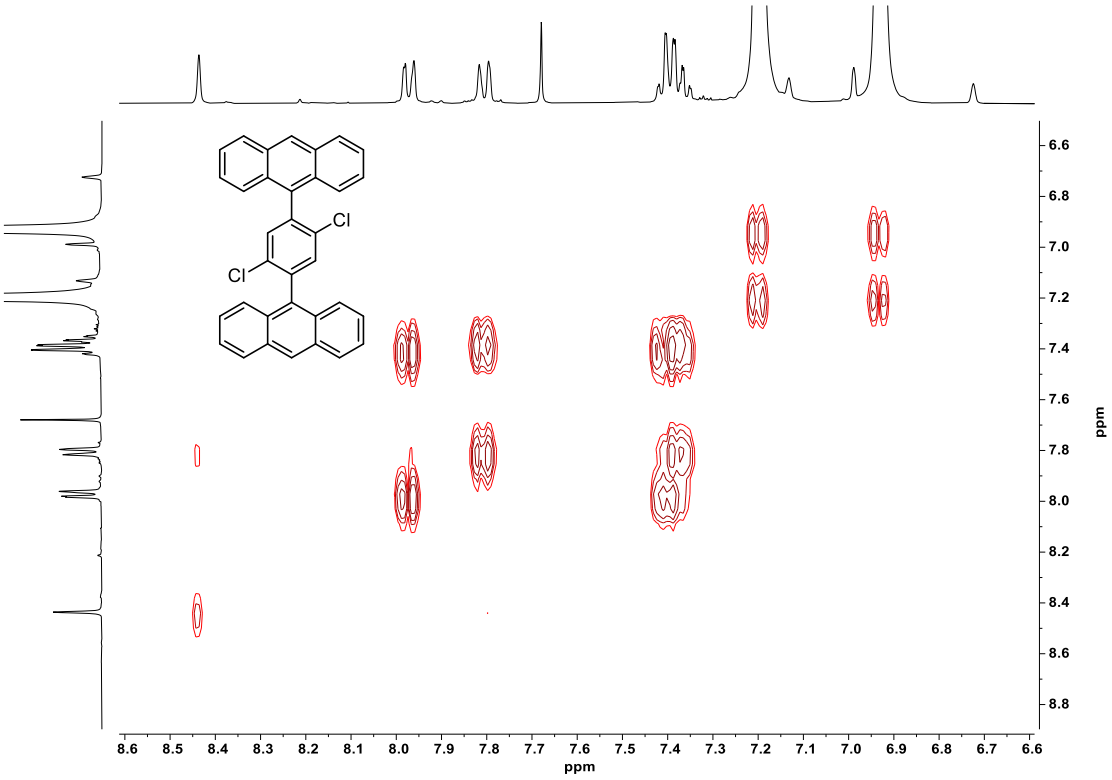

Figure S3: ^{1}H,^{1}H COSY NMR spectrum of compound **5** (400/400 MHz, 343 K, *o*-DCB-d_4).

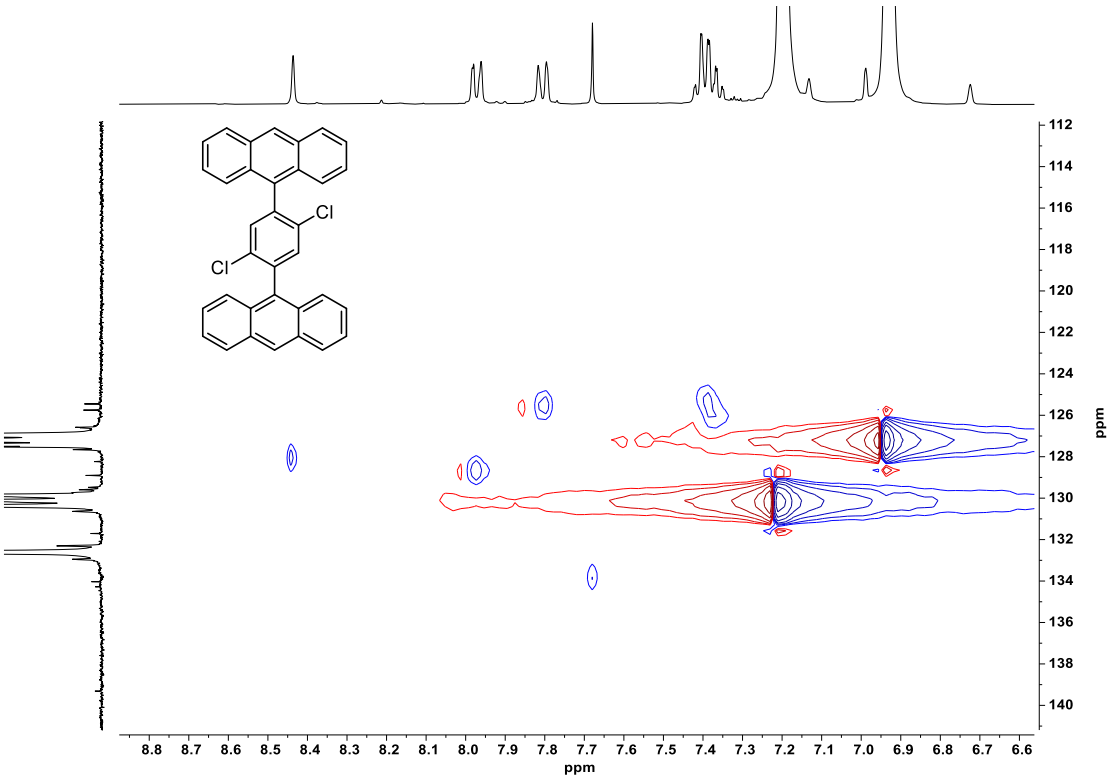

Figure S4: ^{1}H,^{13}C-HSQC NMR spectrum of compound **5** (400/101 MHz, 343 K, *o*-DCB-d_4).

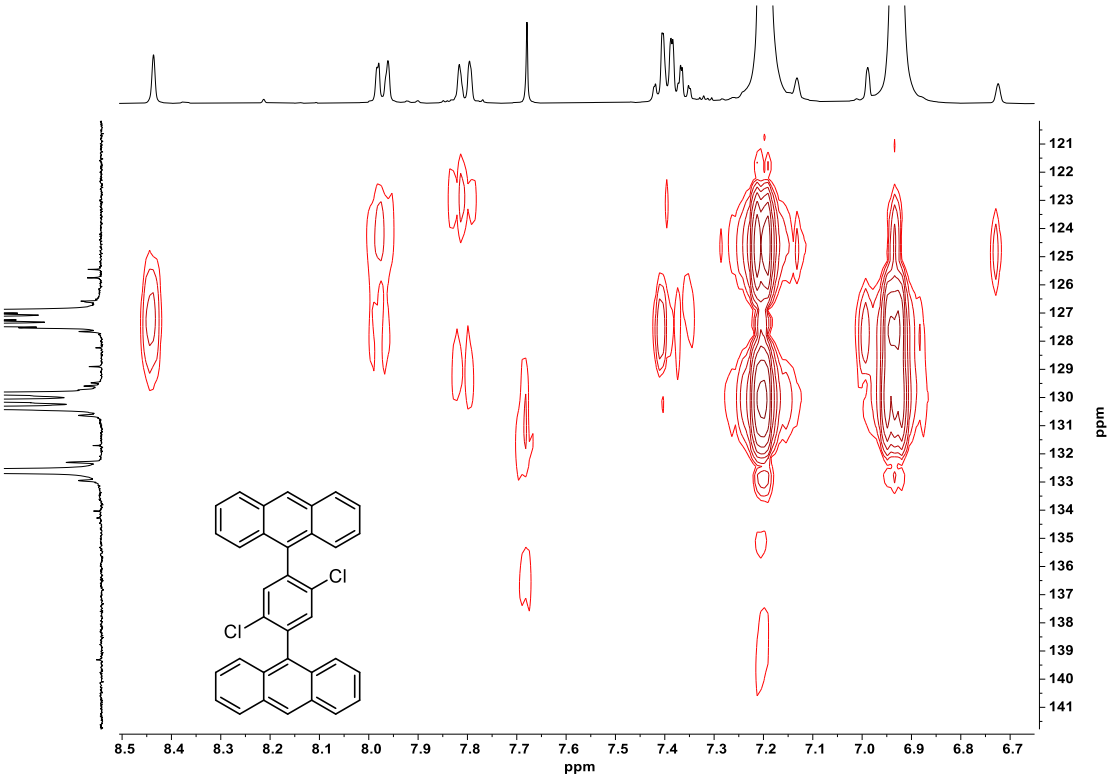

Figure S5: $^{1}H,^{13}C$-HMBC NMR spectrum of compound **5** (400/101 MHz, 343 K, *o*-DCB-d_4).

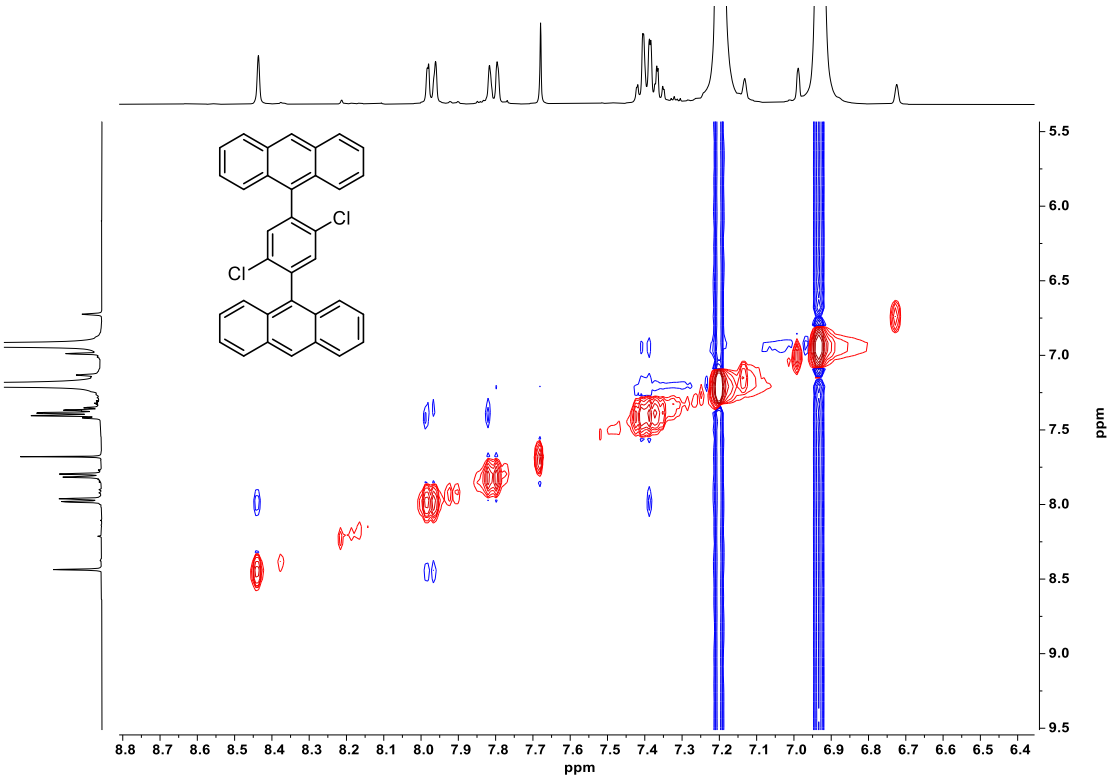

Figure S6: $^{1}H,^{1}H$-NOESY NMR spectrum of compound **5** (400/400 MHz, 343 K, *o*-DCB-d_4).

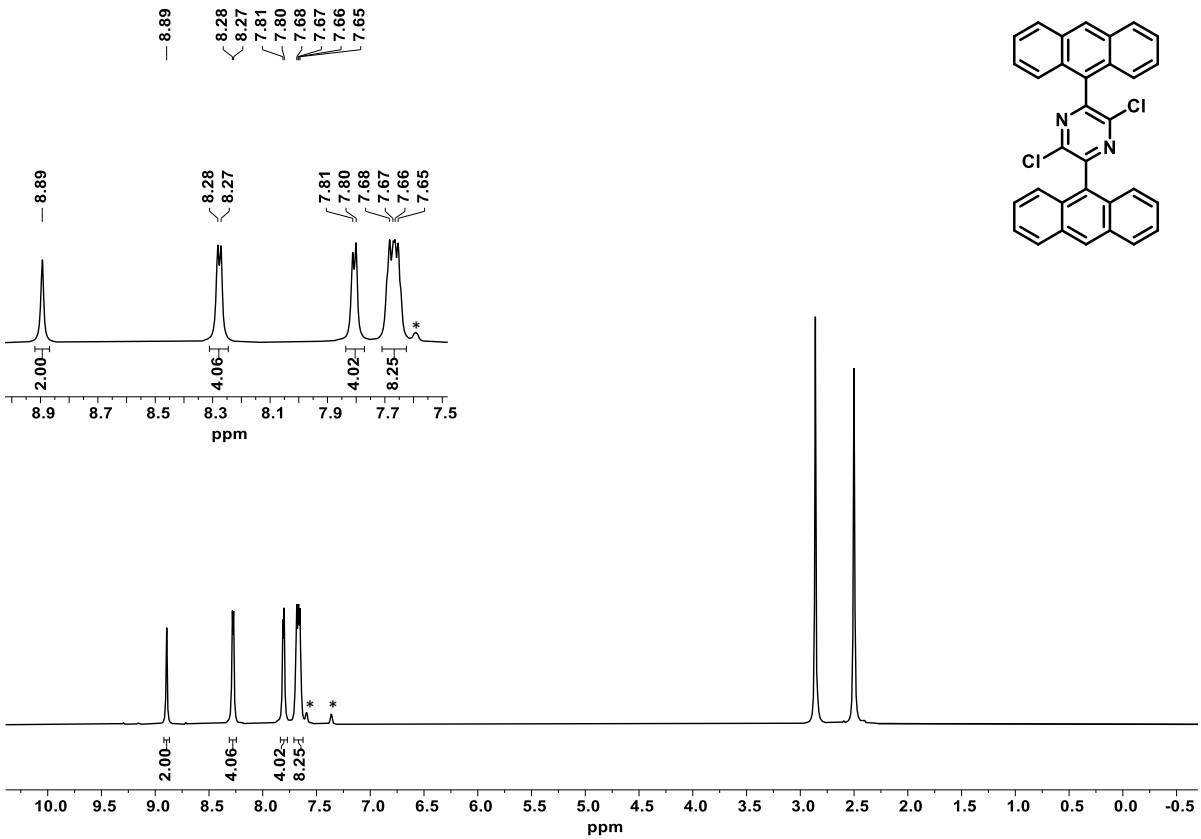

Figure S7: ^{1}H-NMR spectrum of compound **6** (700 MHz, 393 K, DMSO-d_6). The asterisks mark an unidentified impurity.

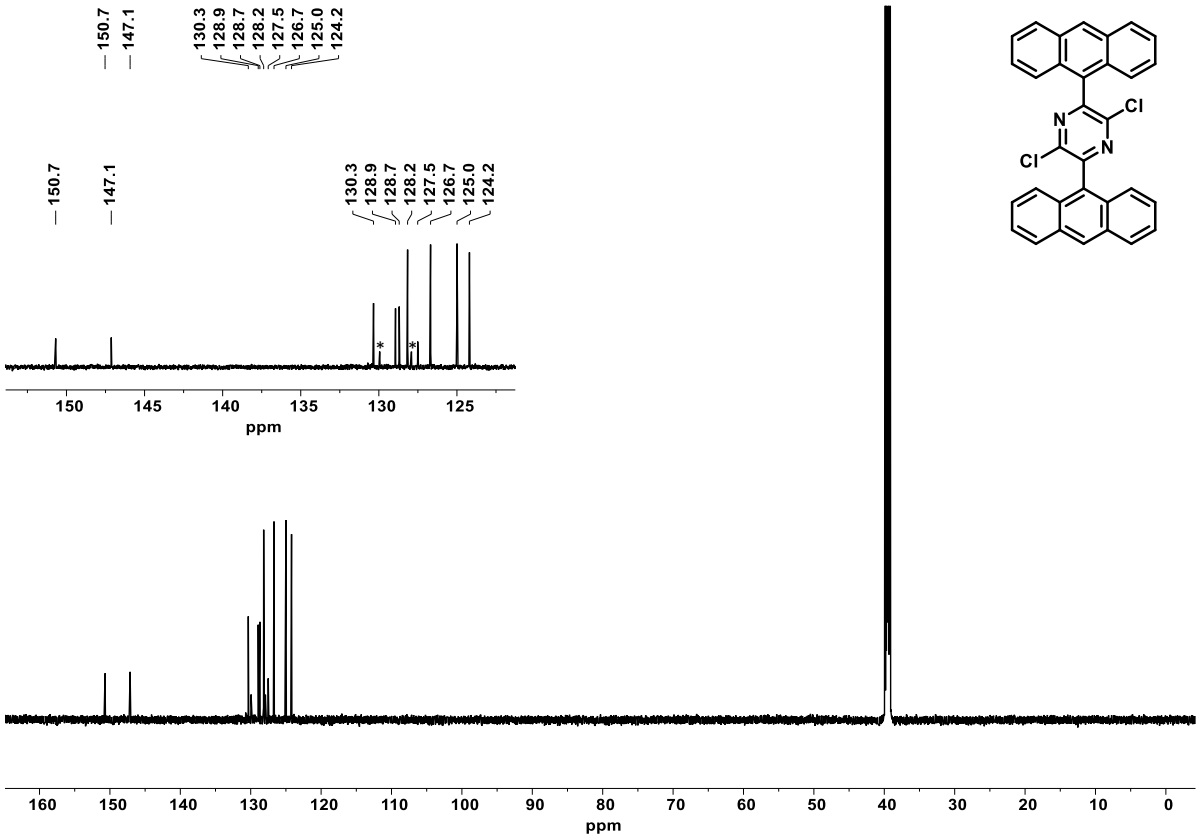

Figure S8: ^{13}C-NMR spectrum of compound **6** (171 MHz, 393 K, DMSO-d_6). The asterisks mark an unidentified impurity.

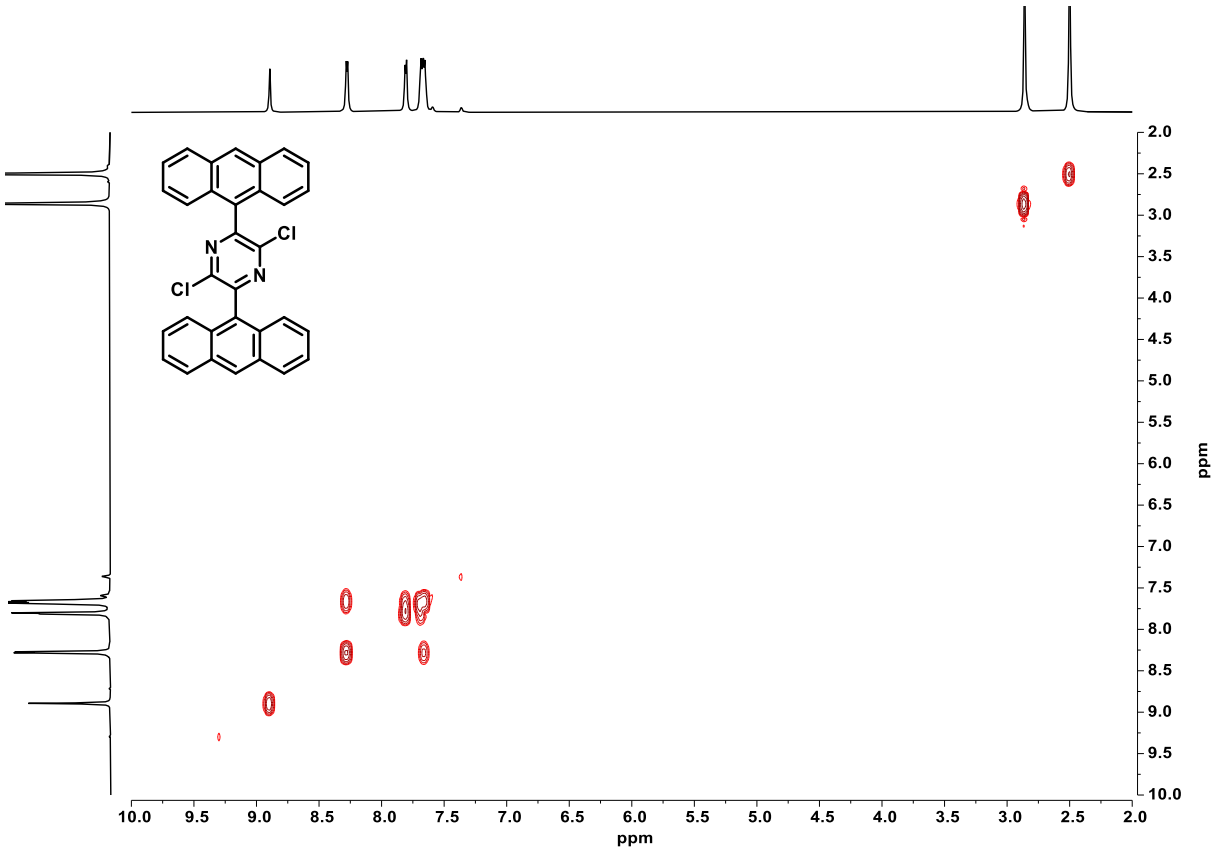

Figure S9: ^{1}H,^{1}H COSY NMR spectrum of compound **6** (700/700 MHz, 393 K, DMSO-d_6).

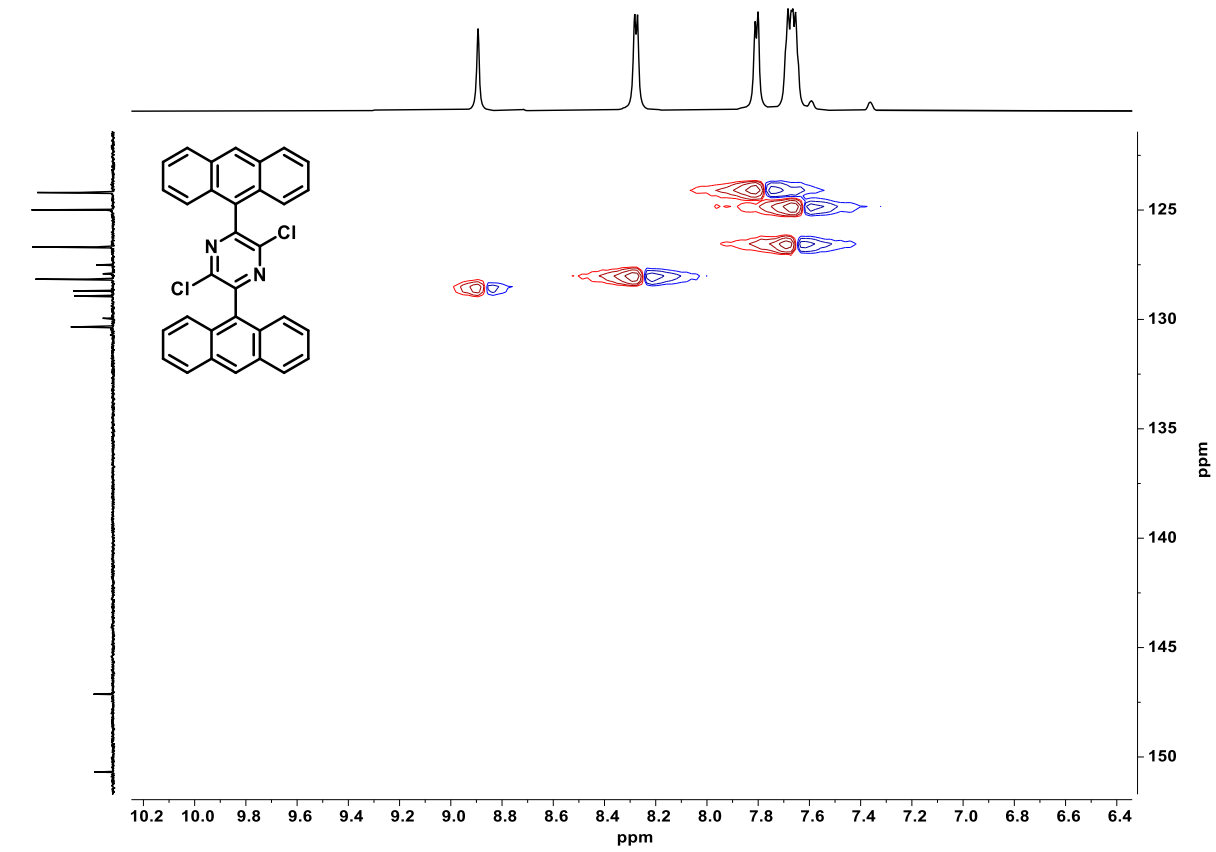

Figure S10: ^{1}H,^{13}C-HSQC NMR spectrum of compound **6** (700/171 MHz, 393 K, DMSO-d_6).

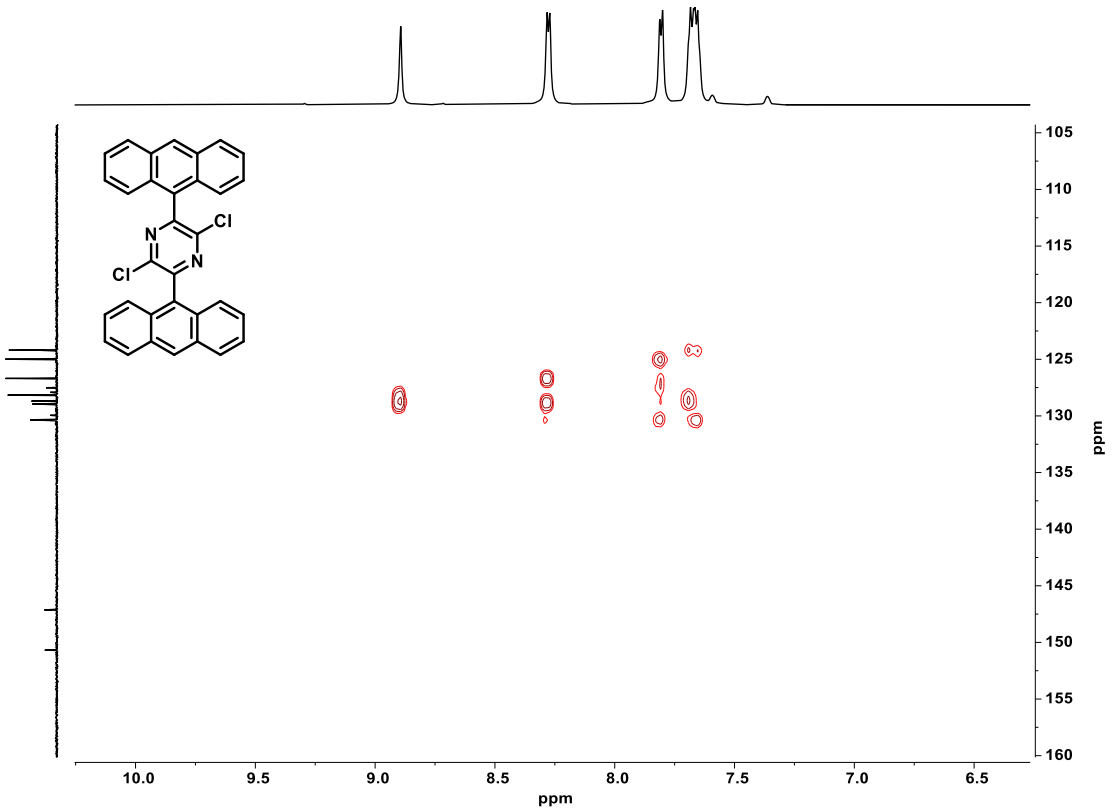

Figure S11: ^{1}H,^{13}C-HMBC NMR spectrum of compound **6** (700/171 MHz, 393 K, DMSO-d_6).

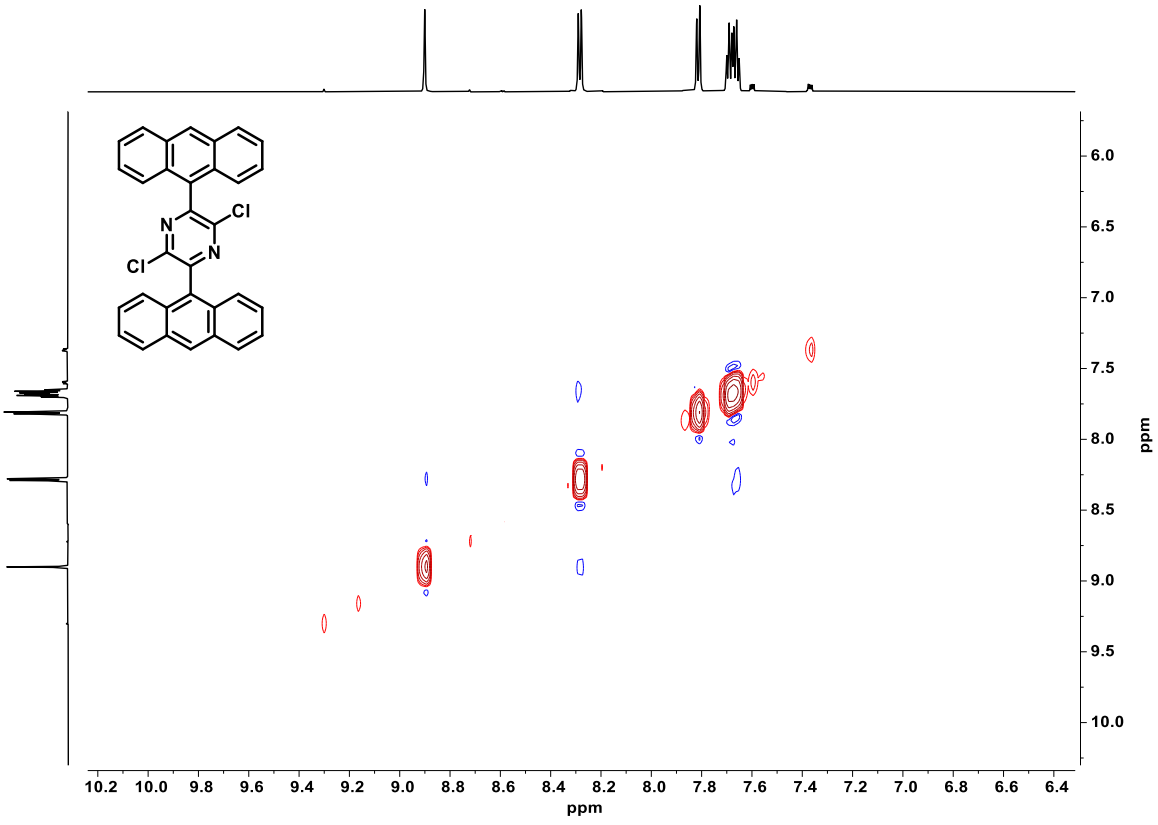

Figure S12: ^{1}H,^{1}H-NOESY NMR spectrum of compound **6** (700/700 MHz, 393 K, DMSO-d_6).

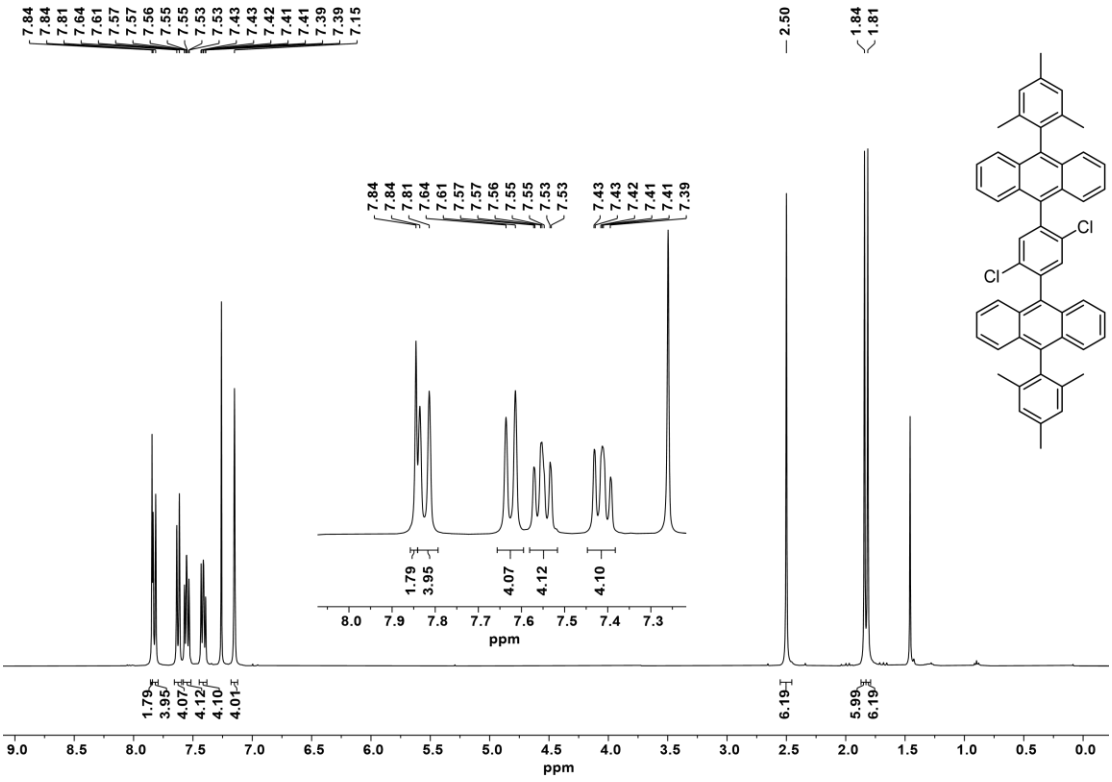

Figure S13: ^{1}H-NMR spectrum of compound **7** (400 MHz, 323 K, $CDCl_3$).

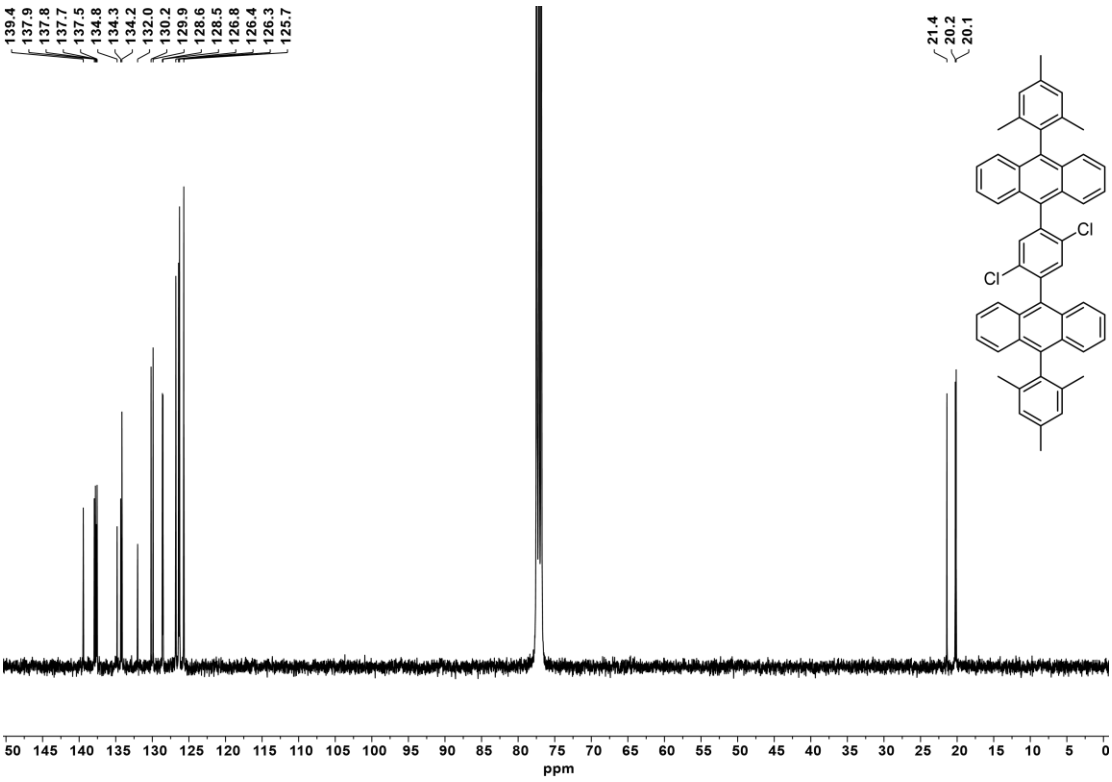

Figure S14: ^{13}C-NMR spectrum of compound **7** (101 MHz, 323 K, $CDCl_3$).

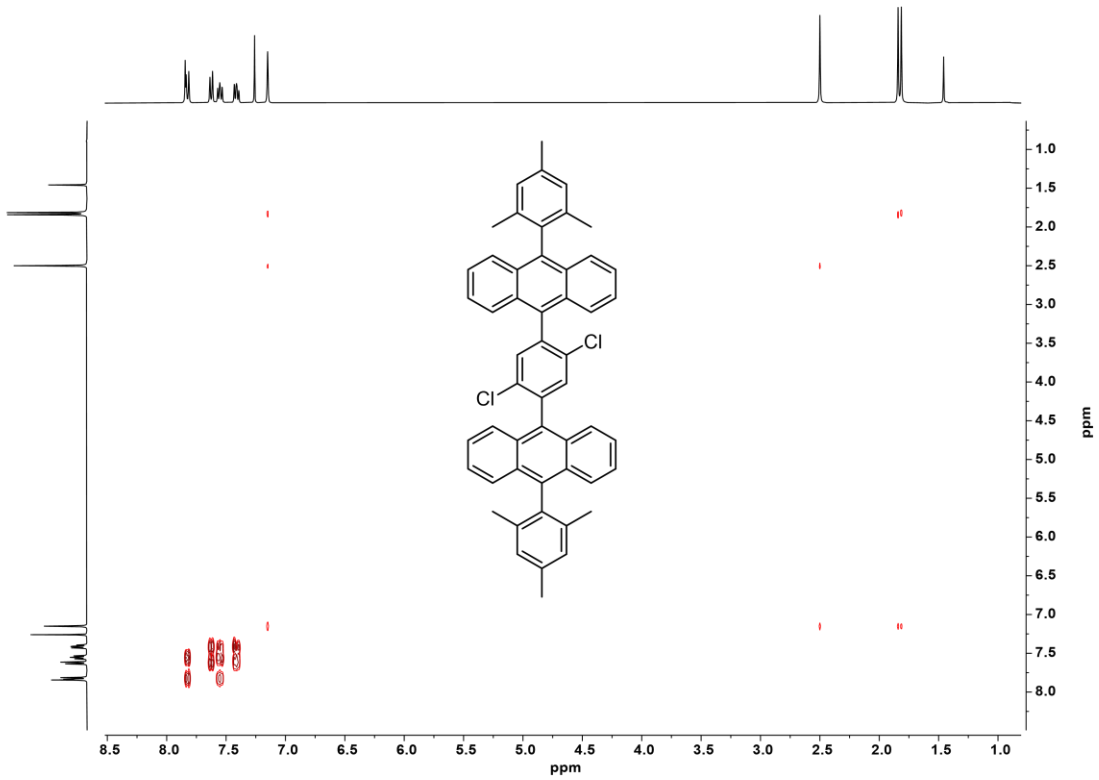

Figure S15: ^{1}H,^{1}H-COSY NMR spectrum of compound **7** (400/400 MHz, 323 K, $CDCl_3$).

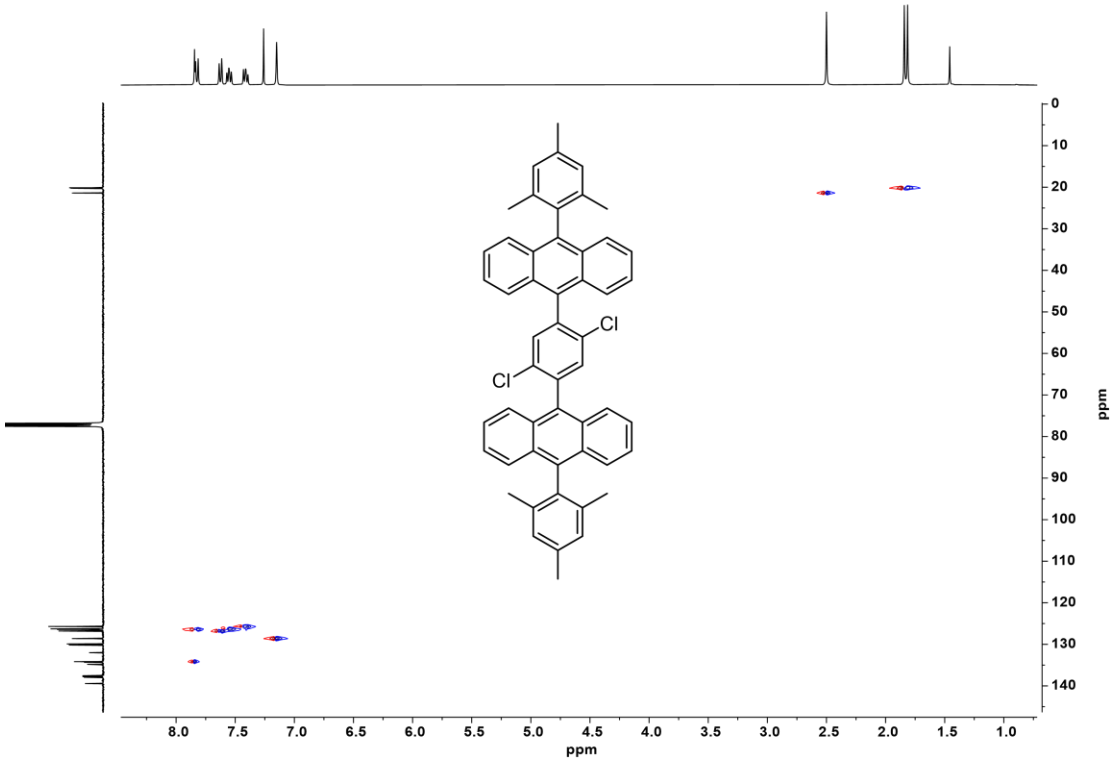

Figure S16: ^{1}H,^{13}C-HSQC NMR spectrum of compound **7** (400/101 MHz, 323 K, $CDCl_3$).

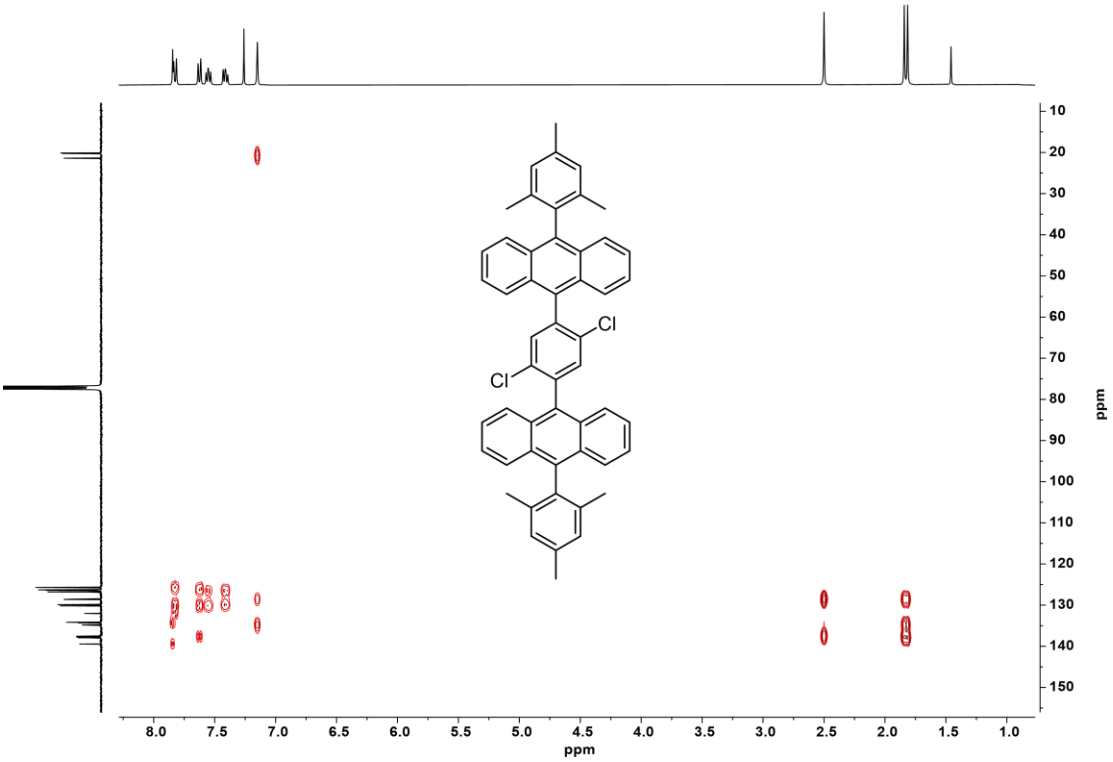

Figure S17: $^{1}H,^{13}C$-HSQC NMR spectrum of compound **7** (400/101 MHz, 323 K, $CDCl_3$).

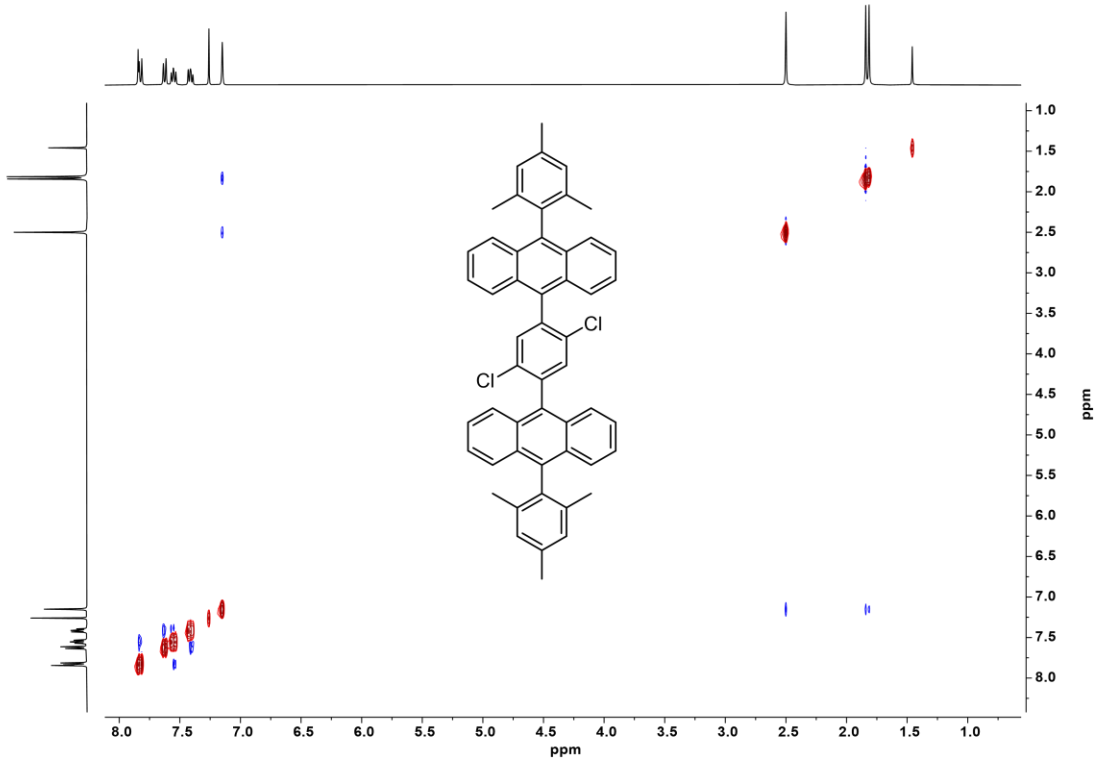

Figure S18: $^{1}H,^{1}H$-NOESY NMR spectrum of compound **7** (400/400 MHz, 323 K, $CDCl_3$).

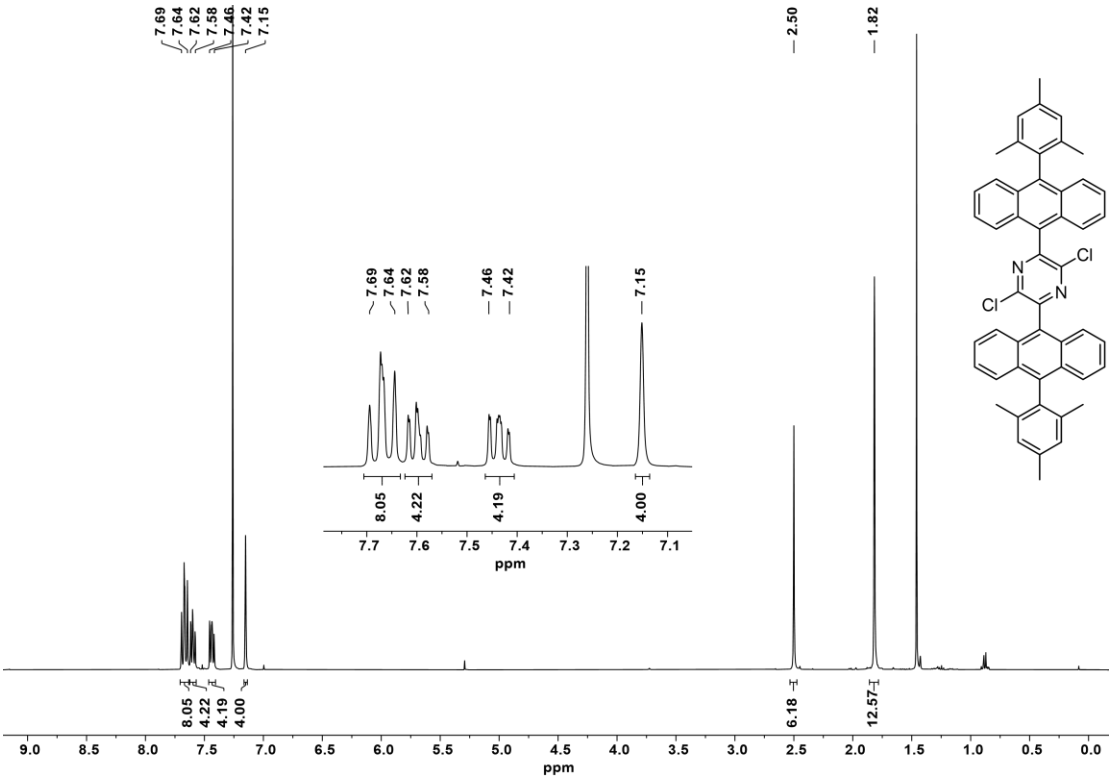

Figure S19: ^{1}H NMR spectrum of compound **8** (400 MHz, 323 K, $CDCl_3$).

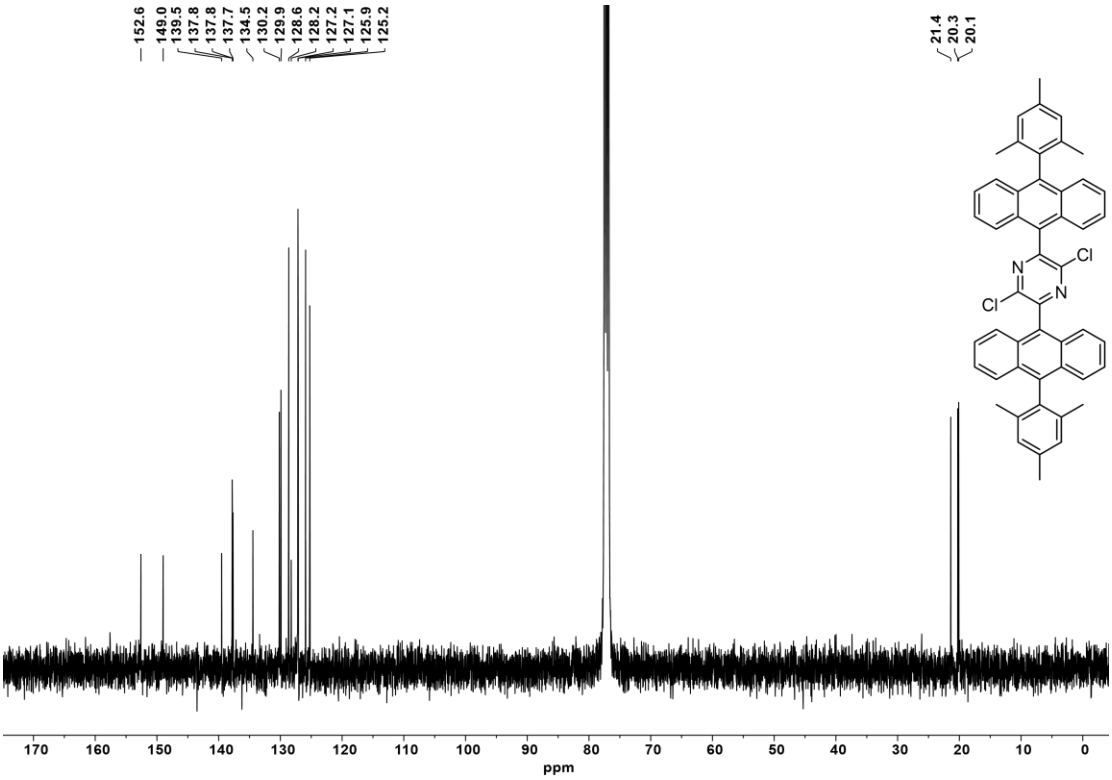

Figure S20: ^{13}C NMR spectrum of compound **8** (101 MHz, 323 K, $CDCl_3$).

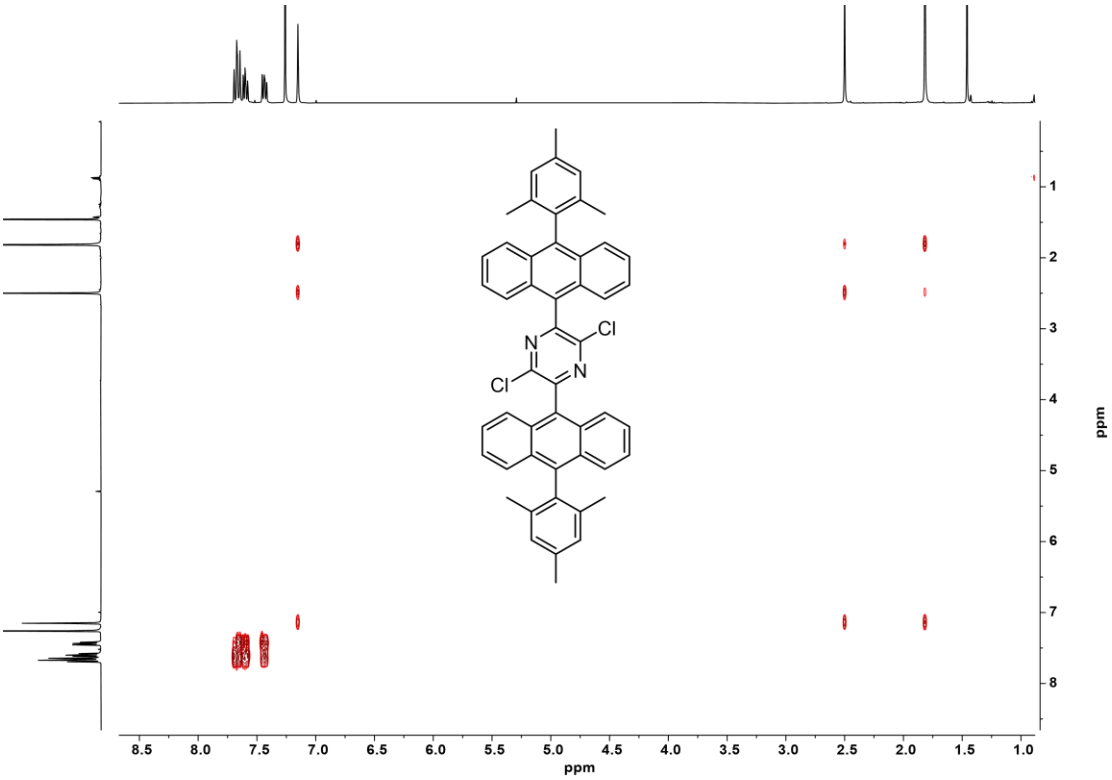

Figure S21: ^{1}H,^{1}H-COSY NMR spectrum of compound **8** (400/400 MHz, 323 K, $CDCl_3$).

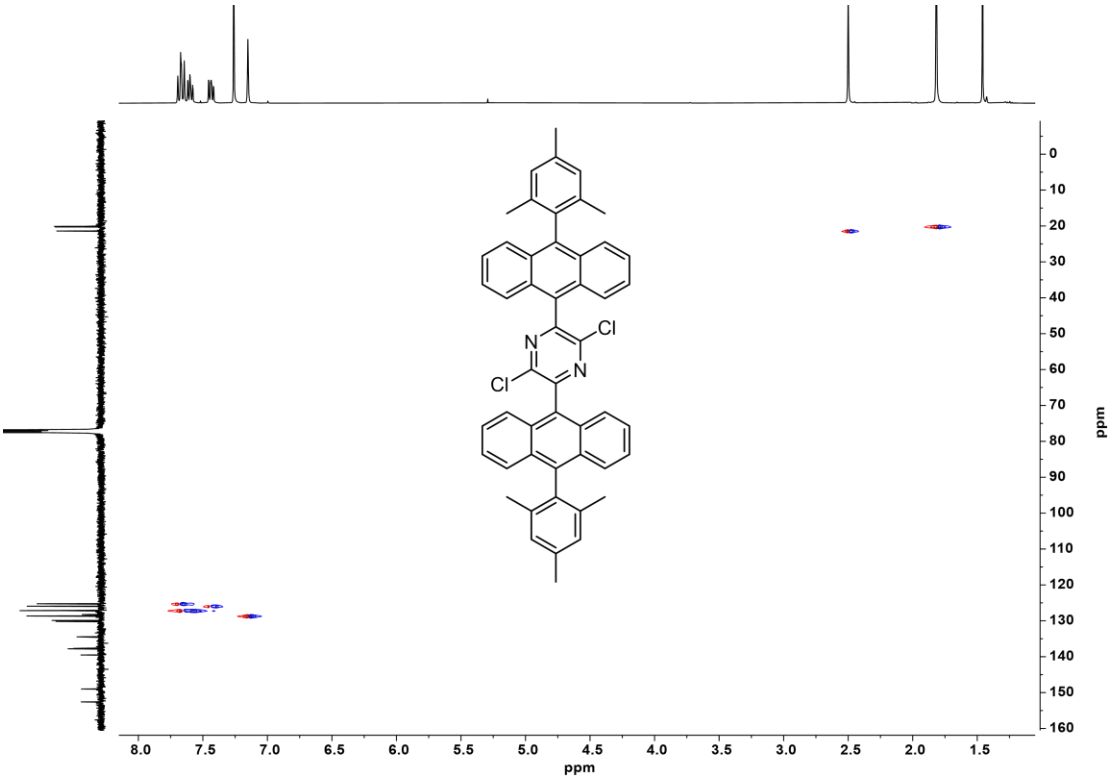

Figure S22: ^{1}H,^{13}C-HSQC NMR spectrum of compound **8** (400/101 MHz, 323 K, $CDCl_3$).

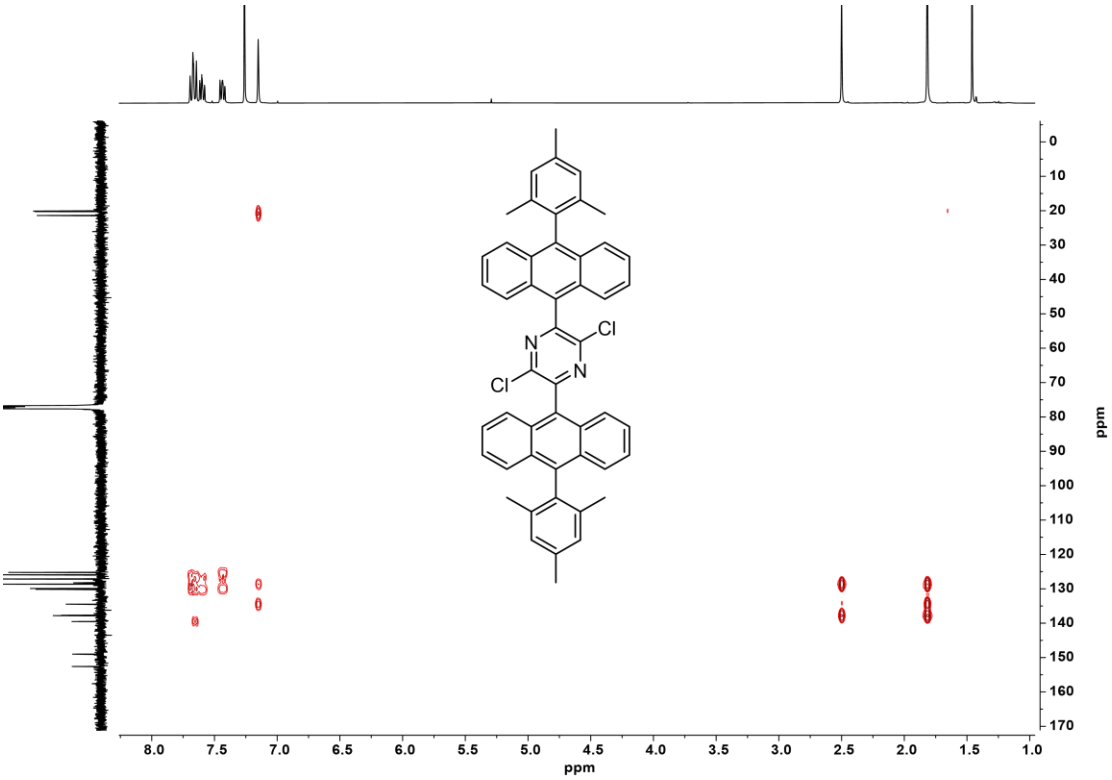

Figure S23: $^{1}H,^{13}C$-HMBC NMR spectrum of compound **8** (400/101 MHz, 323 K, $CDCl_3$).

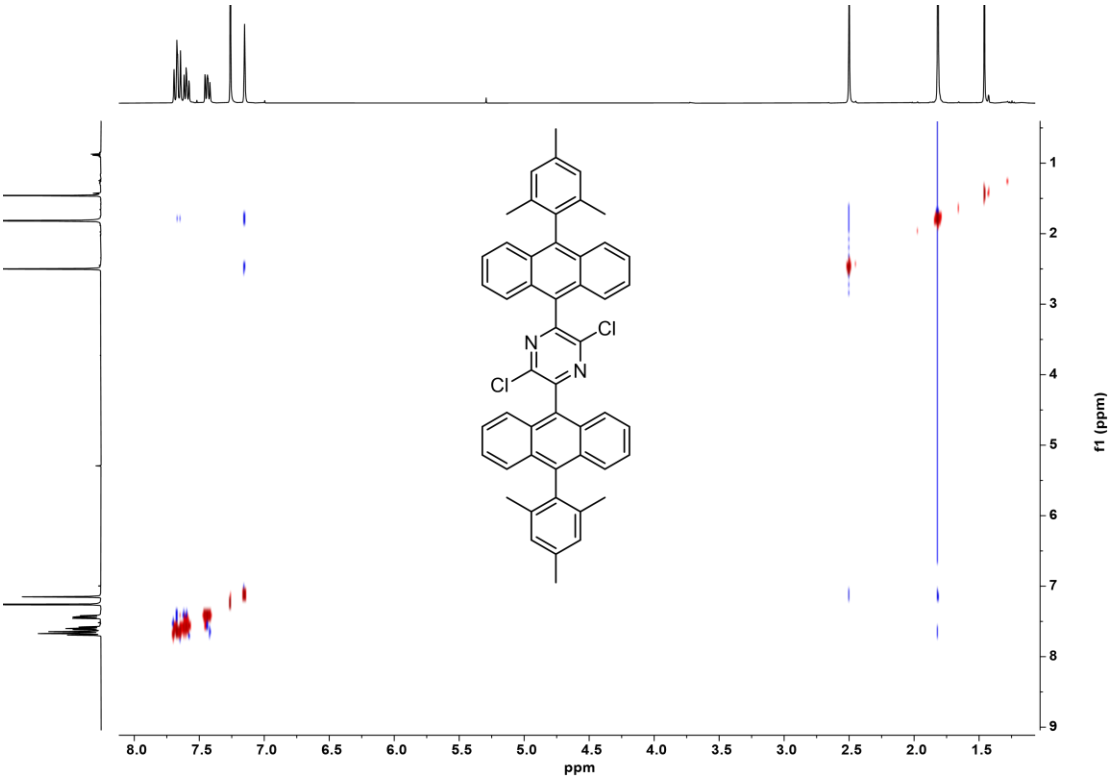

Figure S24: $^{1}H,^{1}H$-NOESY NMR spectrum of compound **8** (400/400 MHz, 323 K, $CDCl_3$).

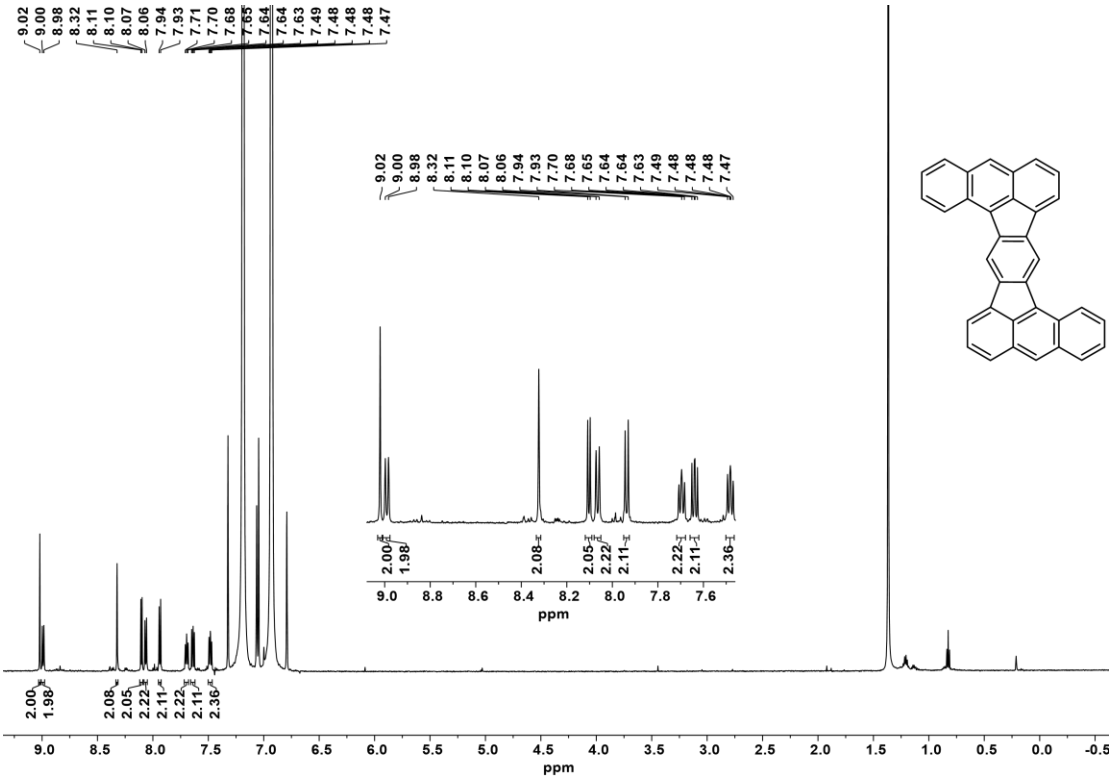

Figure S25: ^{1}H NMR spectrum of compound **DBAF** (600 MHz, *o*-DCB-d_4).

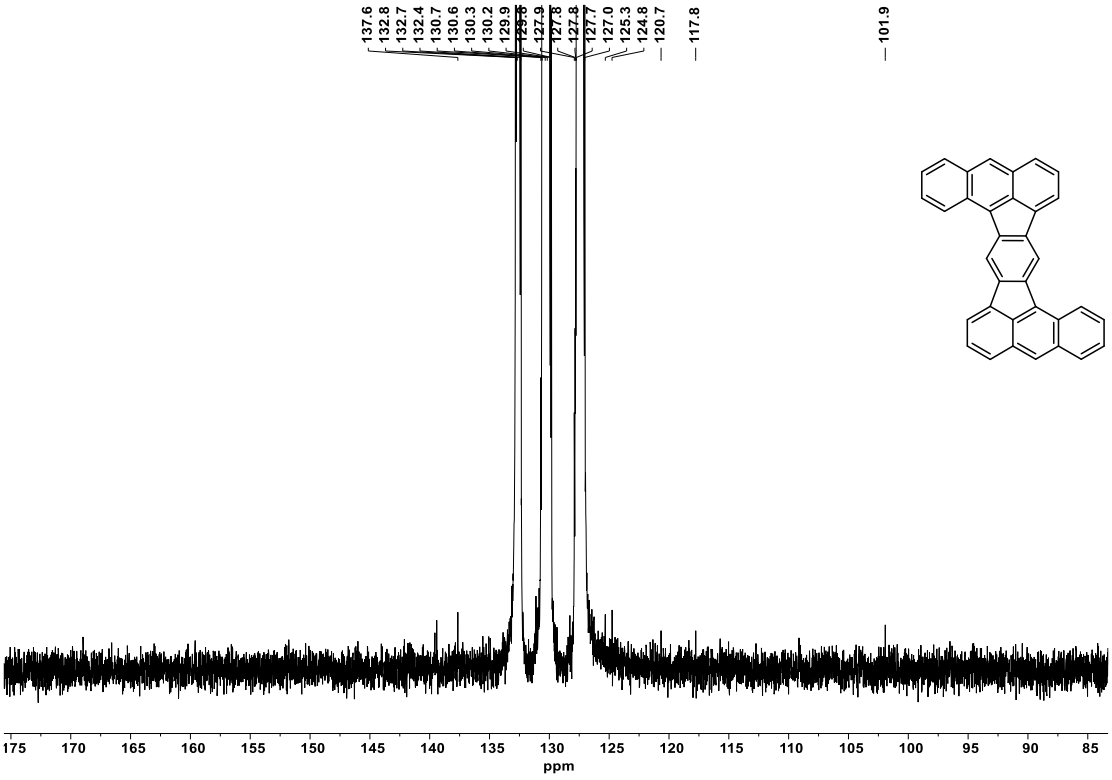

Figure S26: ^{13}C-NMR spectrum of compound **DBAF** (151 MHz, *o*-DCB-d_4).

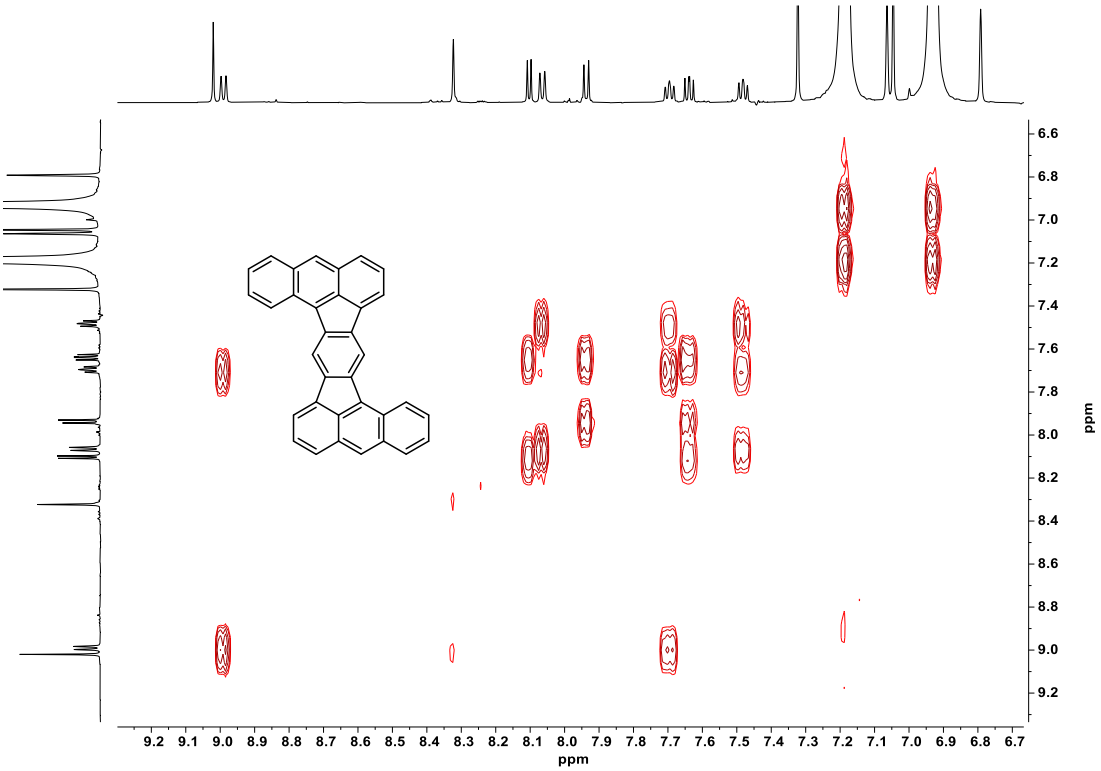

Figure S27:: ^{1}H,^{1}H-COSY NMR spectrum of compound **DBAF** (600/600 MHz, *o*-DCB-d_4).

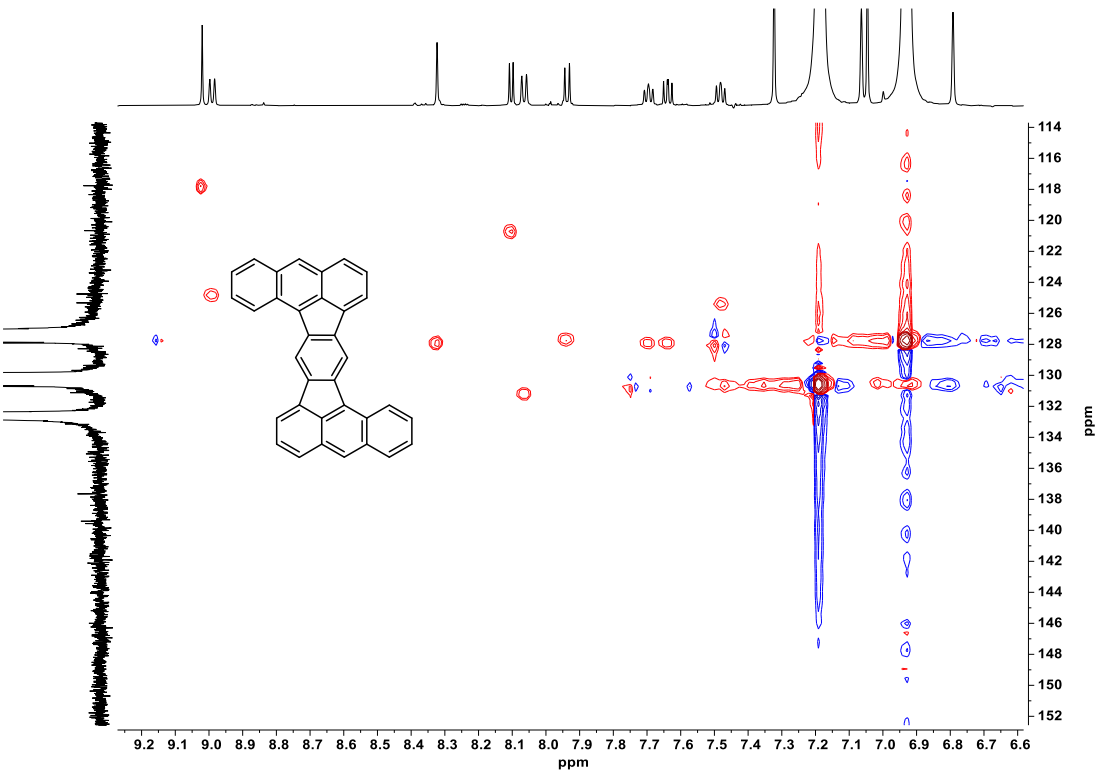

Figure S28: ^{1}H,^{13}C-HSQC NMR spectrum of compound **DBAF** (600/151 MHz, *o*-DCB-d_4).

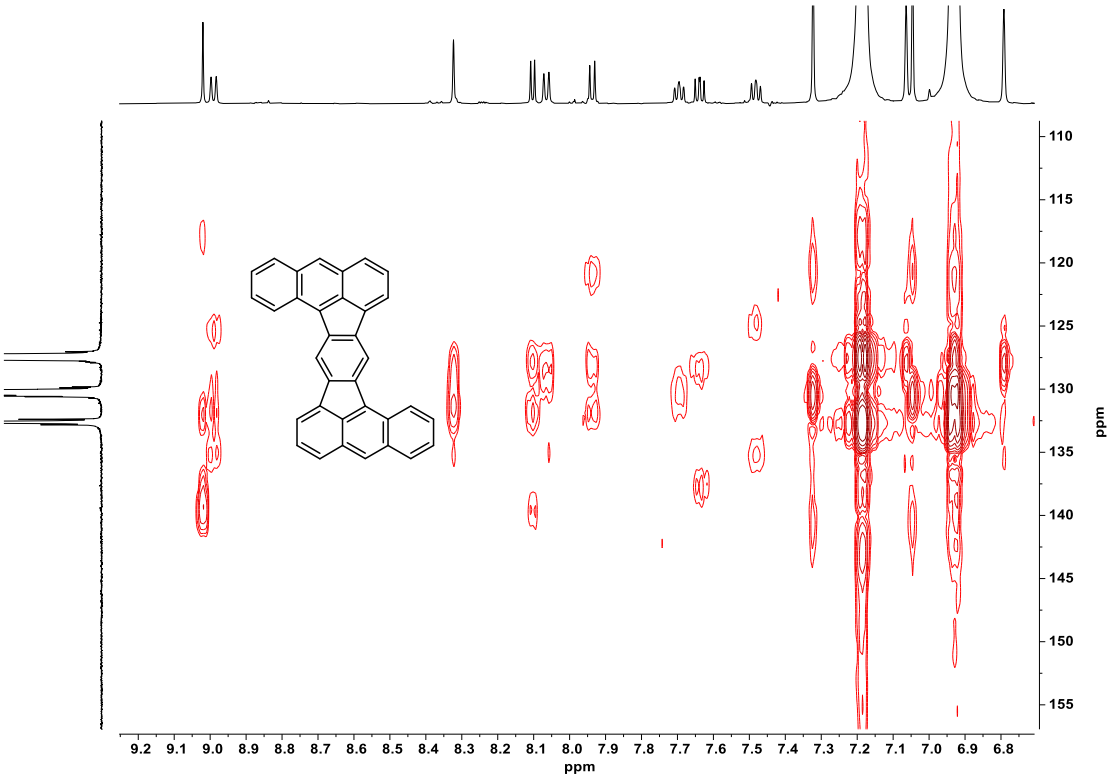

Figure S29: ^{1}H,^{13}C-HMBC NMR spectrum of compound **DBAF** (600/151 MHz, *o*-DCB-d_4).

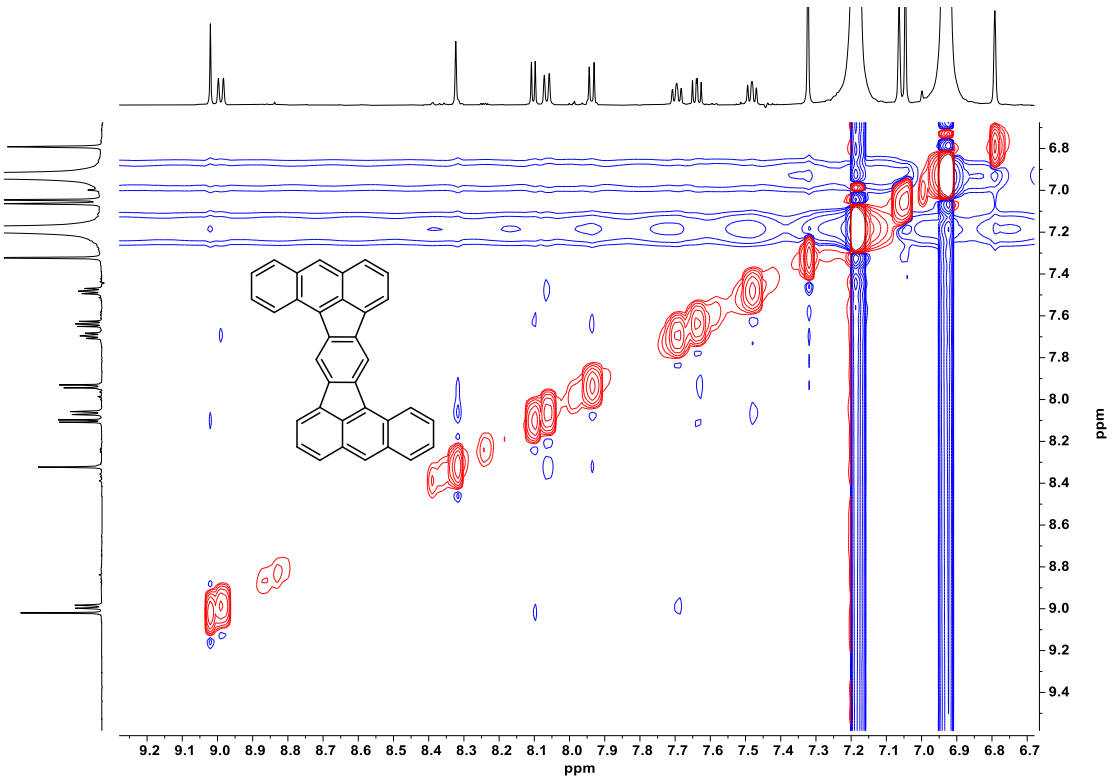

Figure S30: ^{1}H,^{1}H-NOESY NMR spectrum of compound **DBAF** (600/600 MHz, *o*-DCB-d_4).

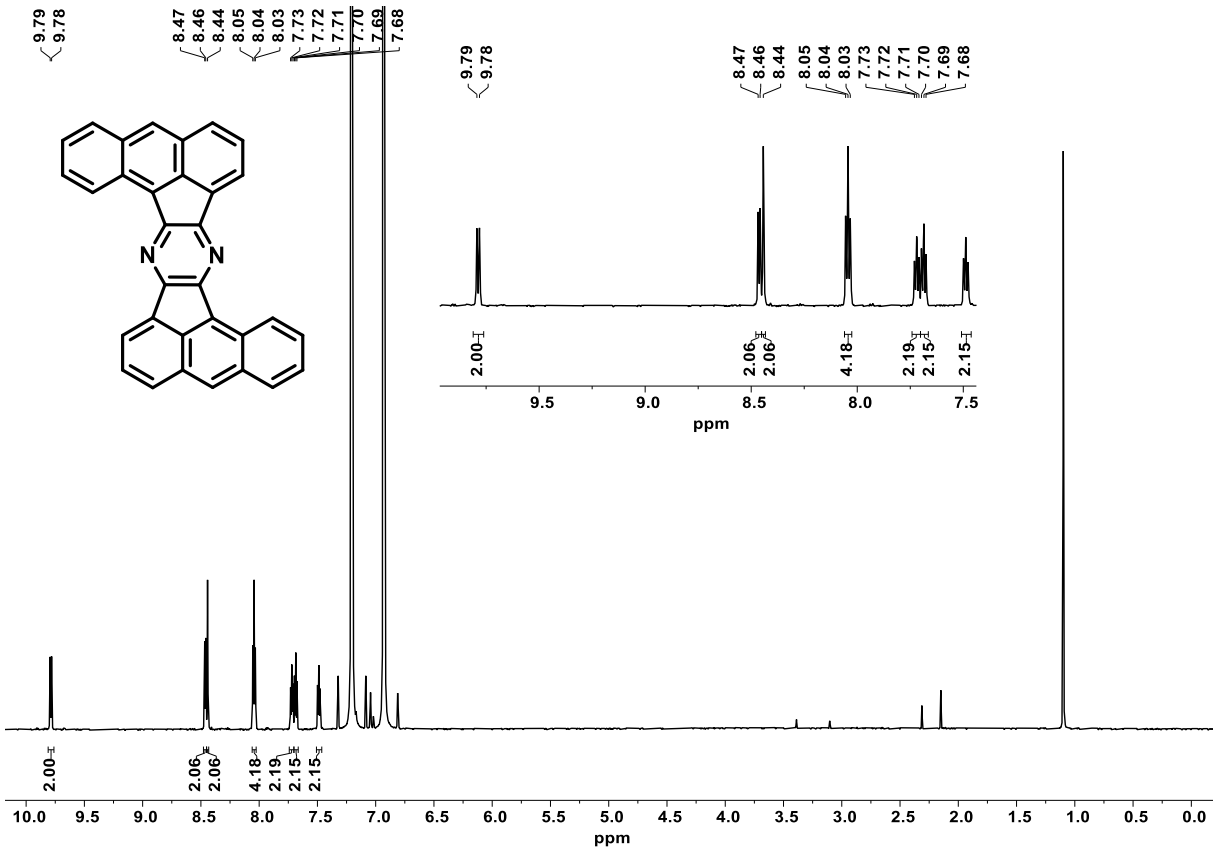

Figure S31: ^{1}H NMR spectrum of compound **DBAF-N_2** (700 MHz, *o*-DCB-d_4, 393 K).

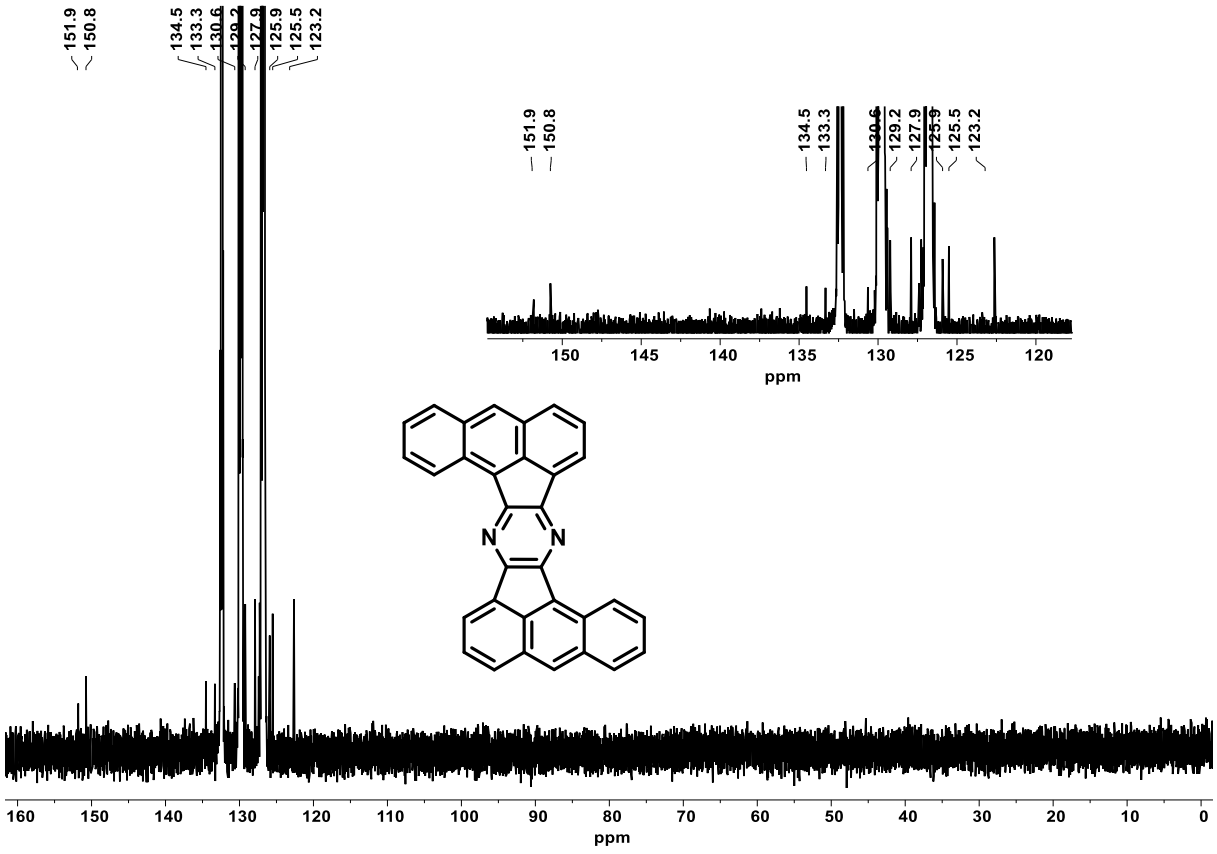

Figure S32: ^{13}C-NMR spectrum of compound **DBAF-N_2** (171 MHz, *o*-DCB-d_4, 393 K, 10240 scans).

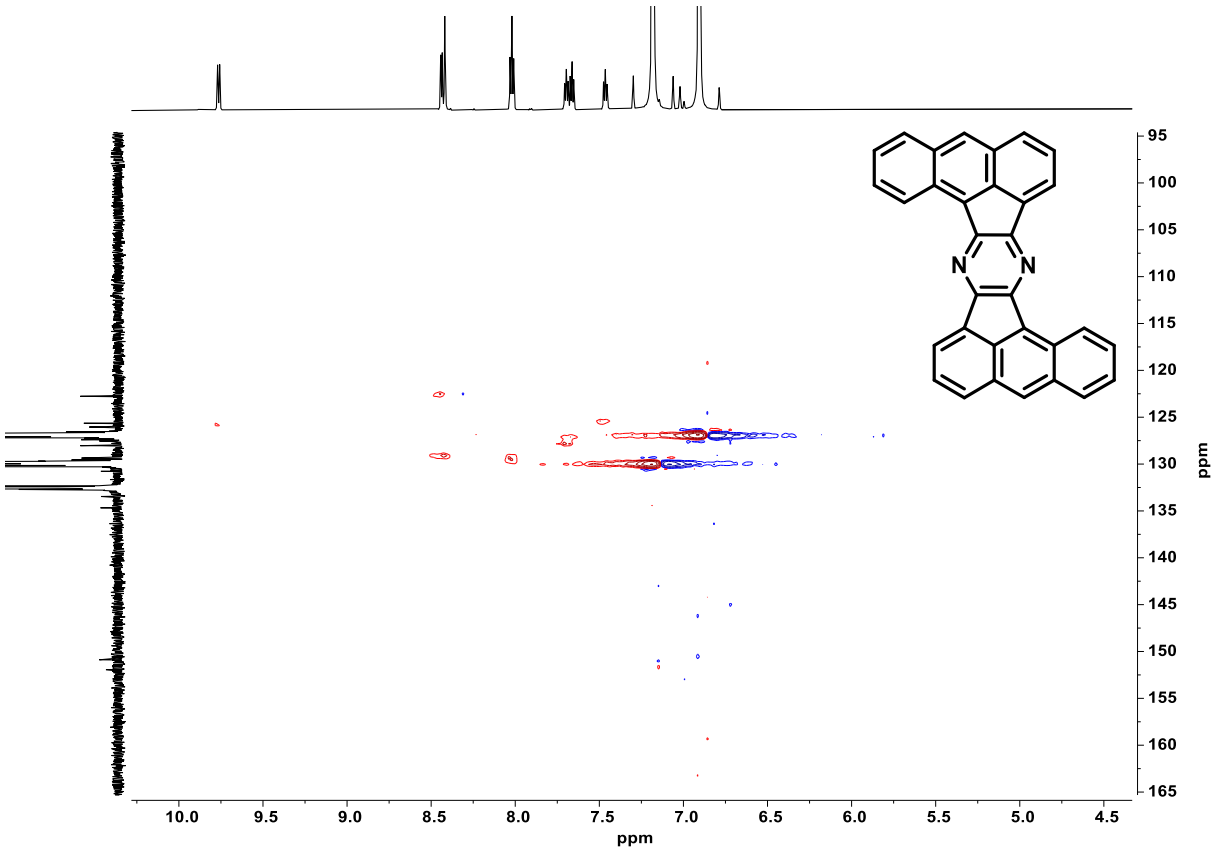

Figure S33: ^{1}H,^{1}H-COSY NMR spectrum of compound **DBAF-N$_2$** (600/600 MHz, *o*-DCB-d_4, 393 K).

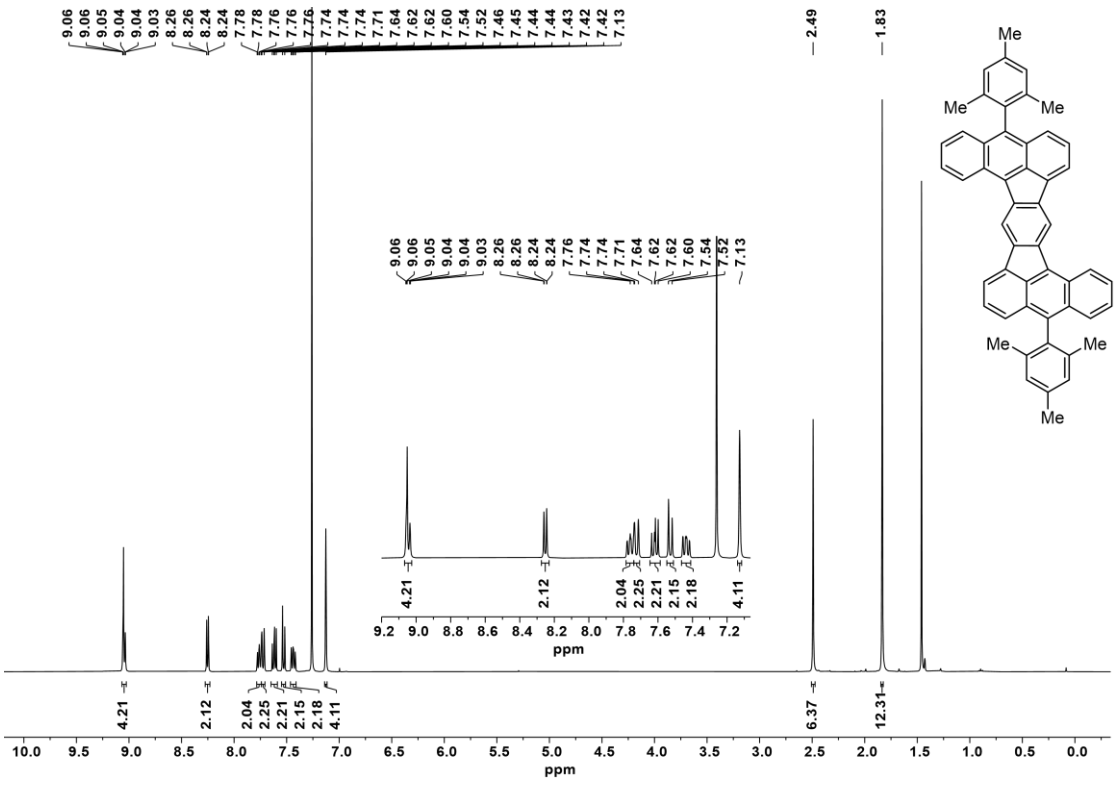

Figure S34: ^{1}H NMR spectrum of compound **mes-DBAF** (400 MHz, 323 K, $CDCl_3$).

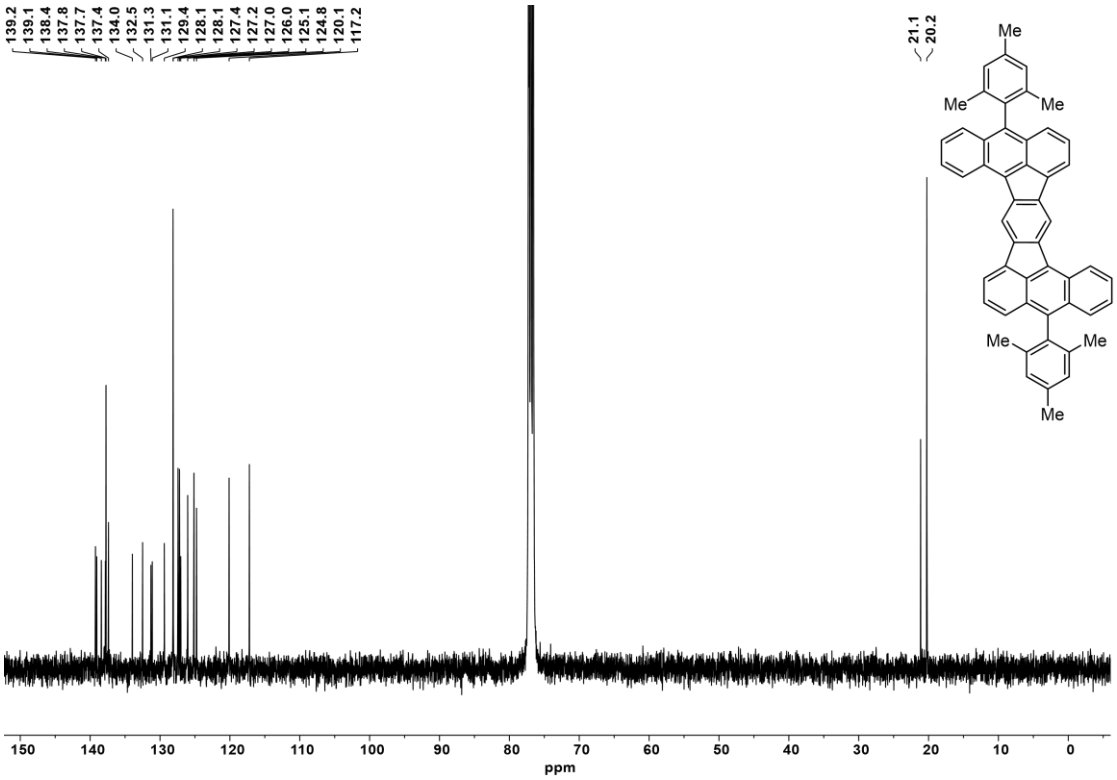

Figure S35: ^{13}C NMR spectrum of compound **mes-DBAF** (101 MHz, 323 K, $CDCl_3$).

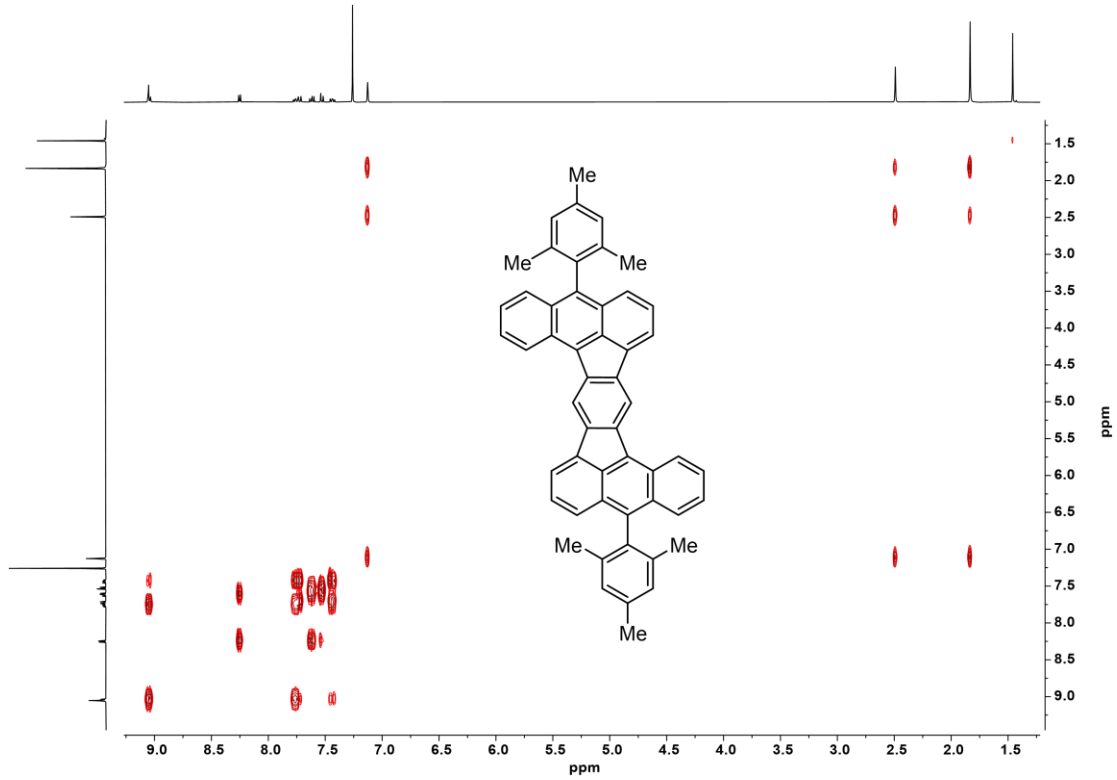

Figure S36: $^{1}H,^{1}H$-COSY NMR spectrum of compound **mes-DBAF** (400/400 MHz, 323 K, $CDCl_3$).

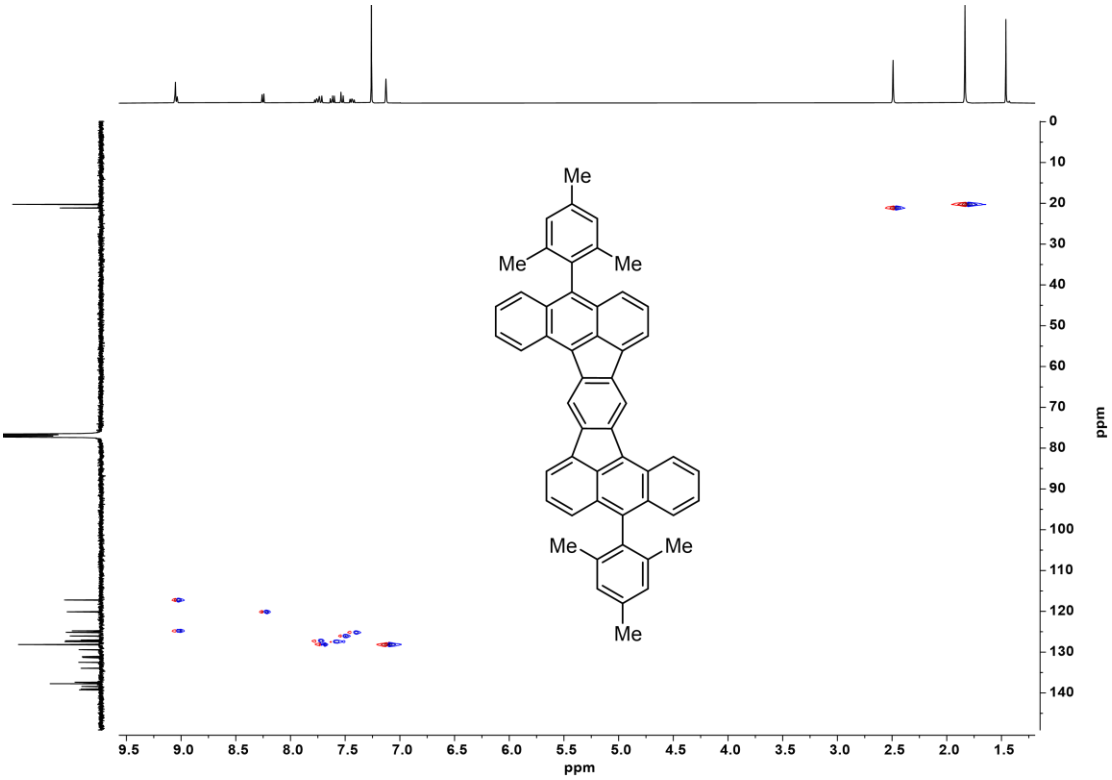

Figure S37: $^{1}H,^{13}C$-HSQC spectrum of compound **mes-DBAF** (400/101 MHz, 323 K, $CDCl_3$).

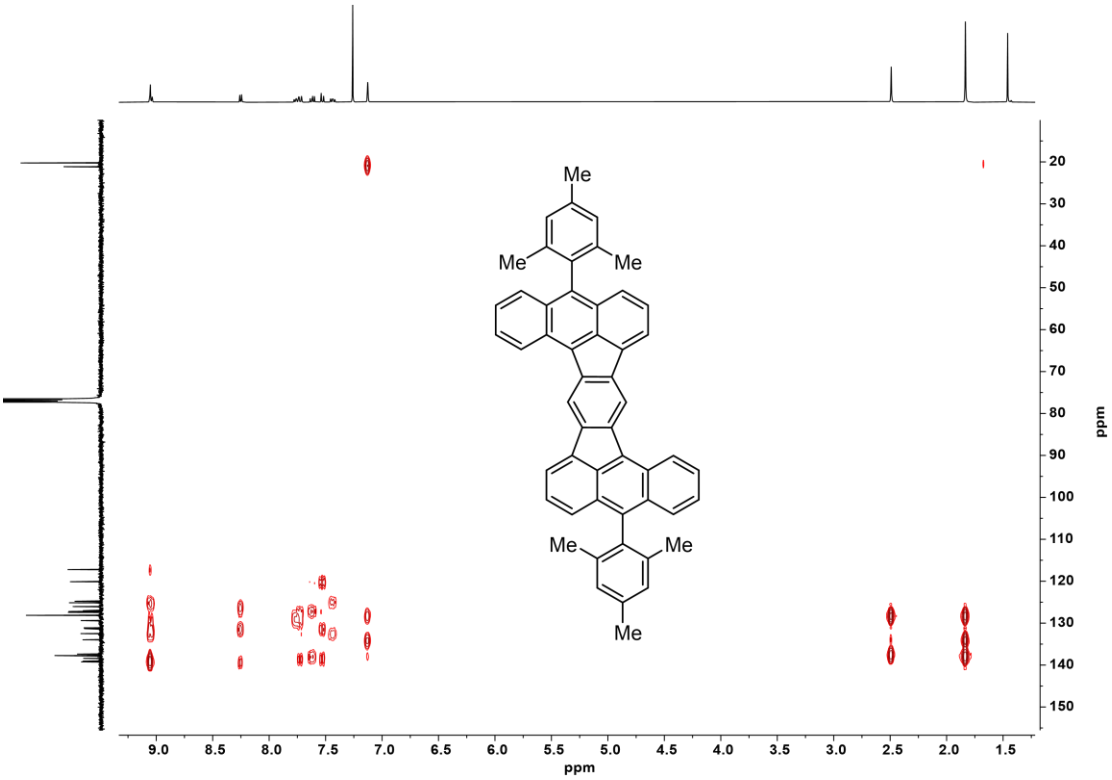

Figure S38: $^{1}H,^{13}C$-HMBC NMR spectrum of compound **mes-DBAF** (400/101 MHz, 323 K, $CDCl_3$).

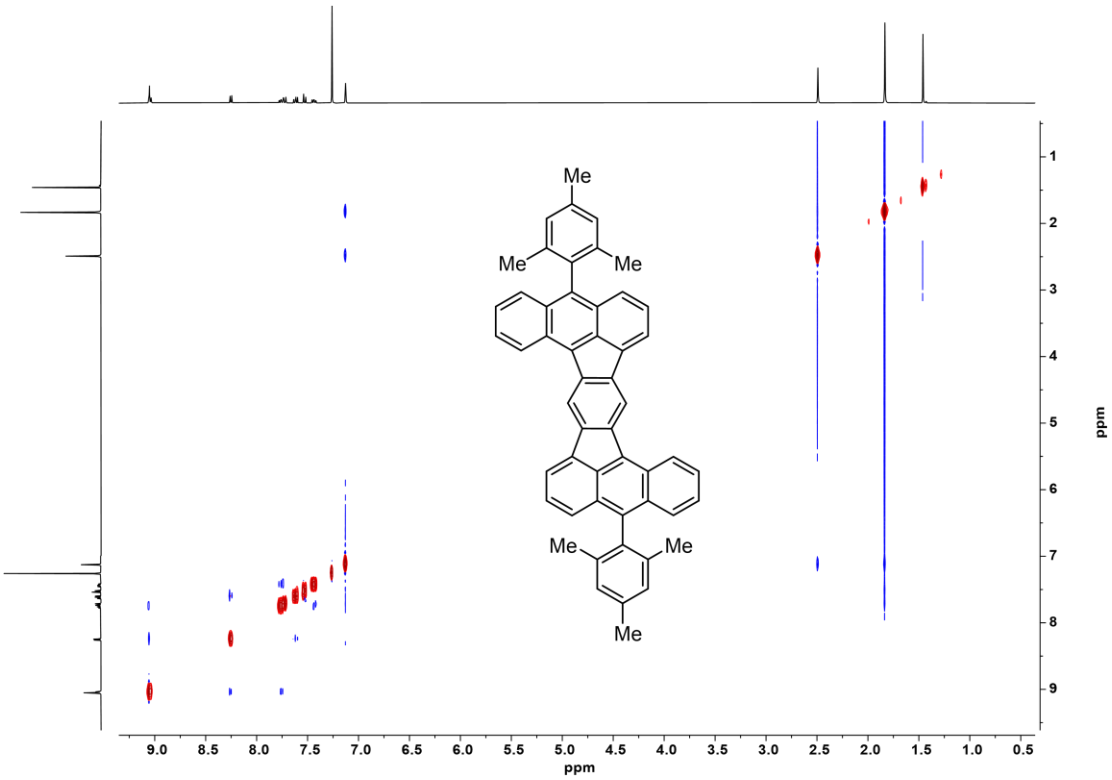

Figure S39: ^{1}H,^{1}H-NOESY NMR spectrum of compound **mes-DBAF** (400/400 MHz, 323 K, $CDCl_3$).

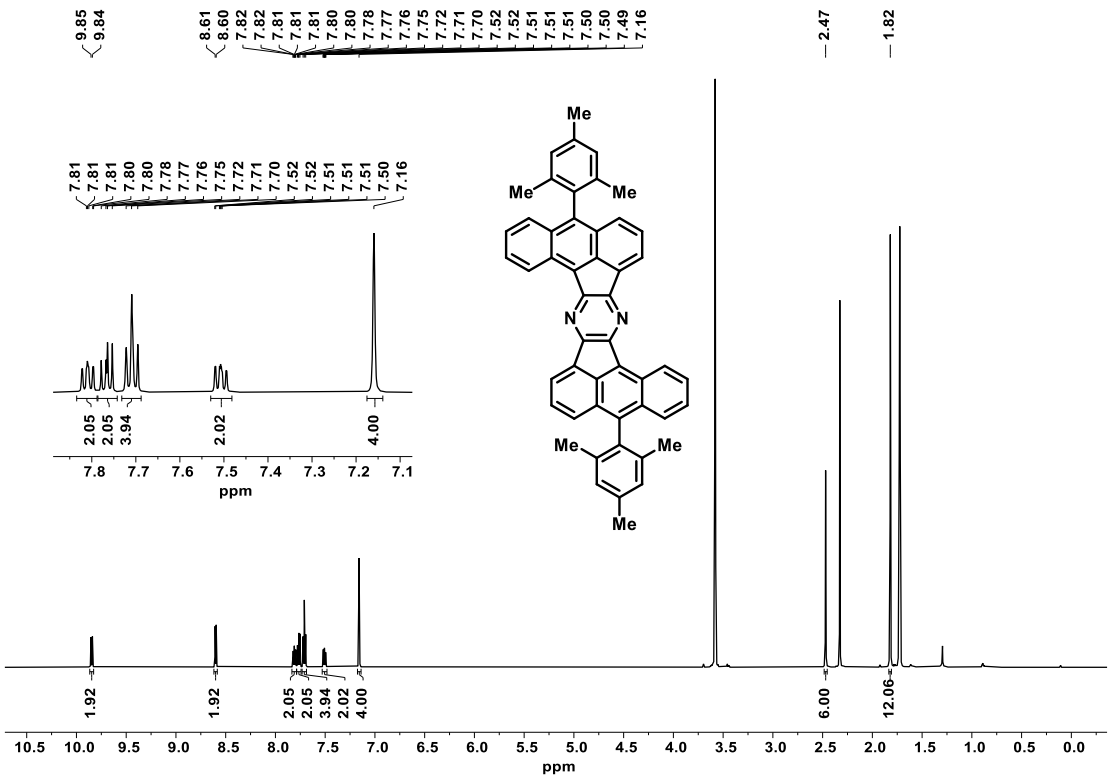

Figure S40: ^{1}H NMR spectrum of **mes-DBAF-N_2** (600 MHz, 323 K, THF-d_8).

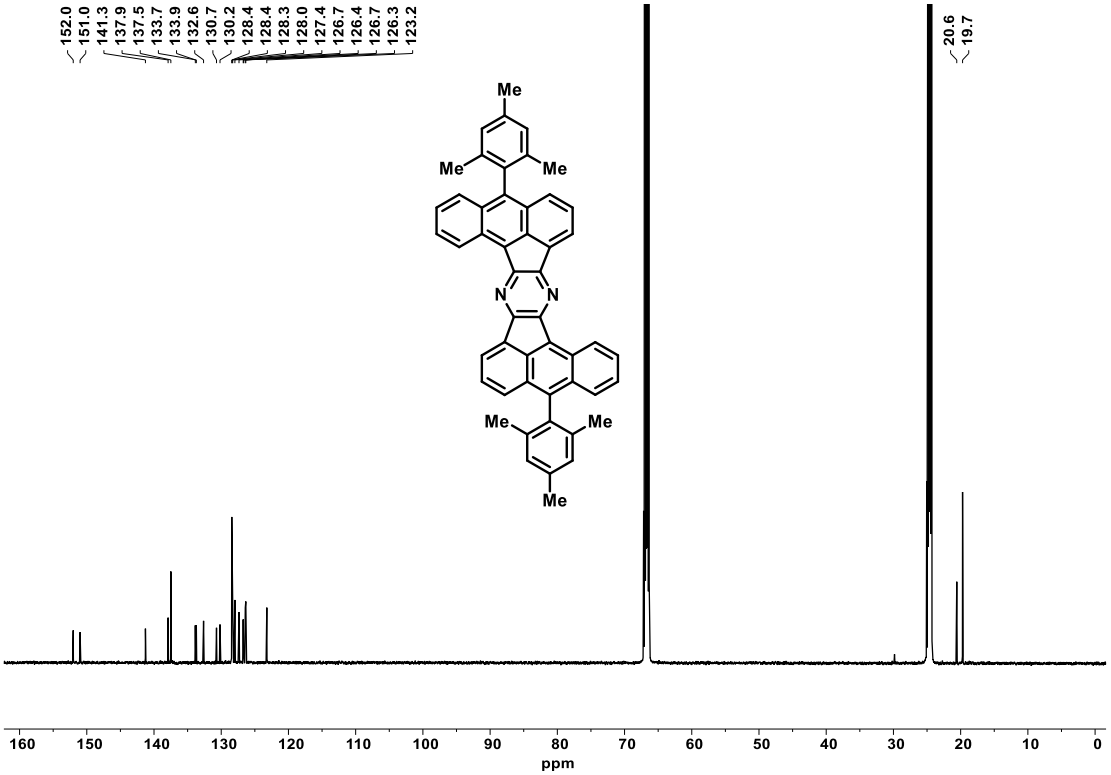

Figure S41: ^{13}C NMR spectrum of **mes-DBAF-N$_2$** (151 MHz, 323 K, THF-d_8).

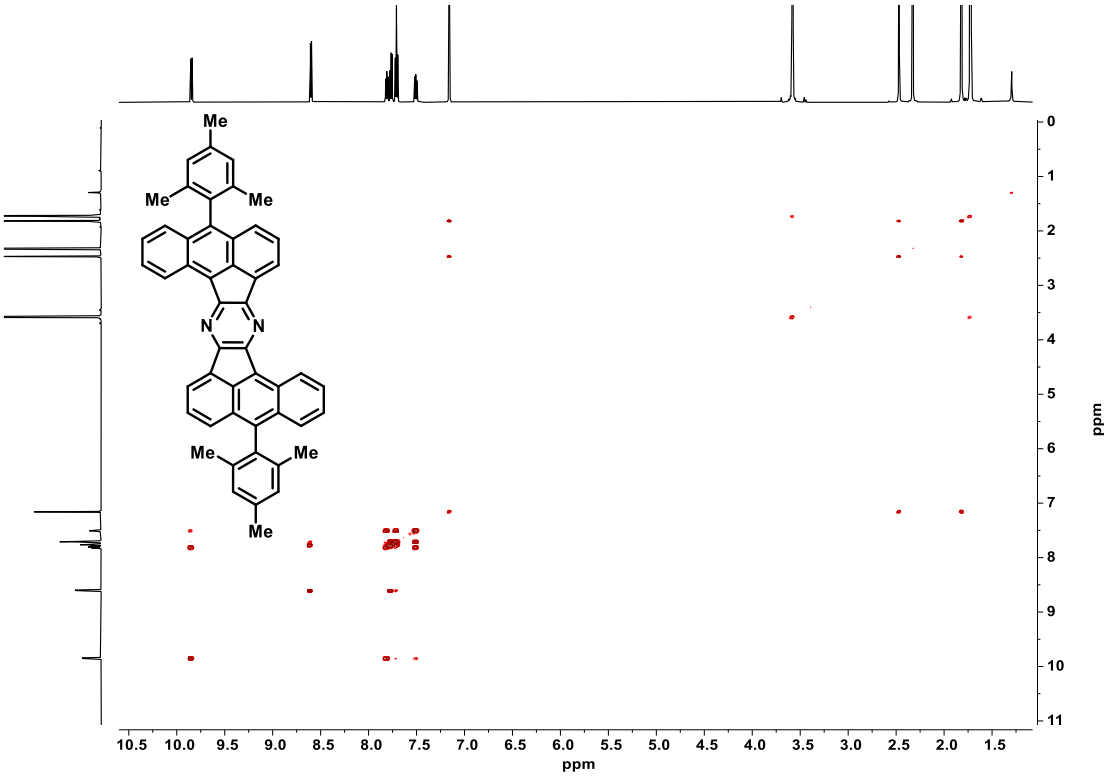

Figure S42: ^{1}H,^{1}H NMR spectrum of **mes-DBAF-N$_2$** (600/600 MHz, 323 K, THF-d_8).

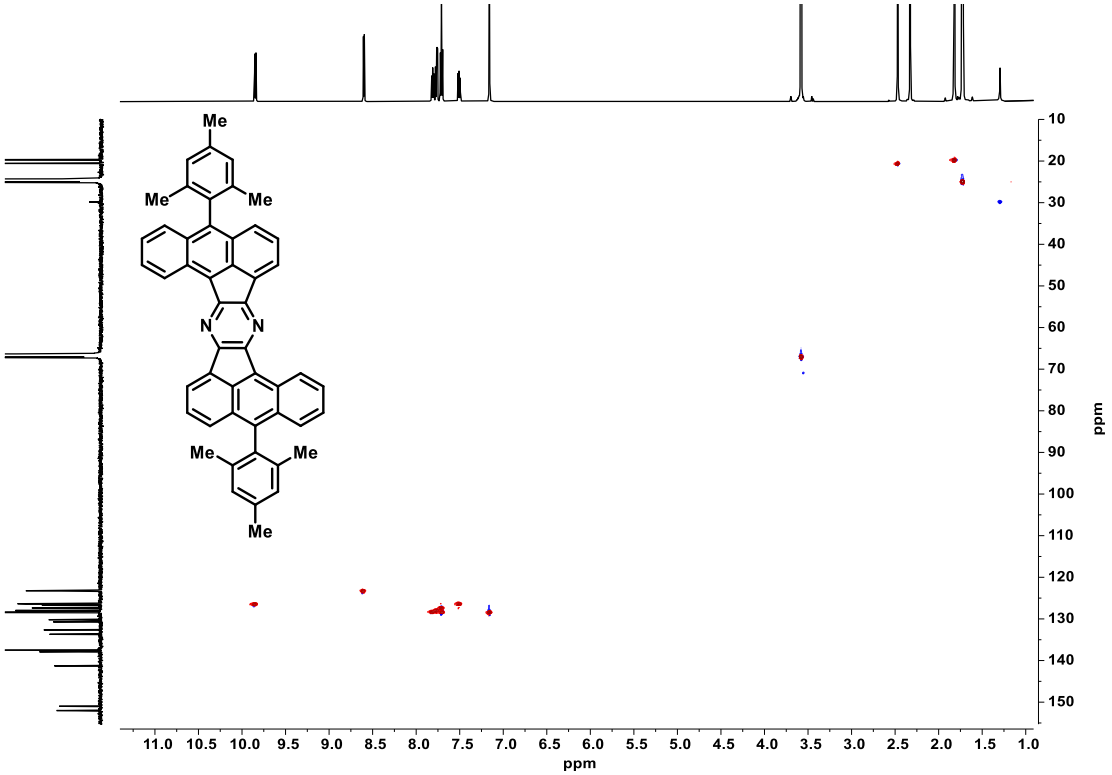

Figure S43: ^{1}H,^{13}C-HSQC NMR spectrum of **mes-DBAF-N$_2$** (600/151 MHz, 323 K, THF-d_8).

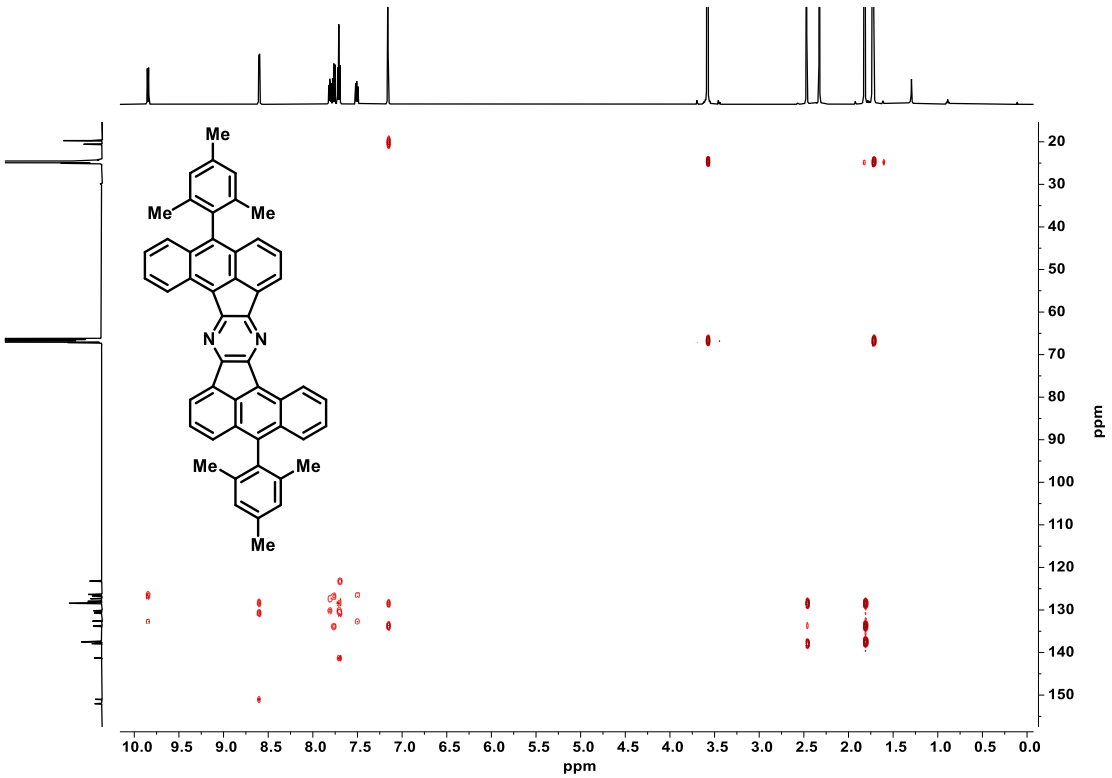

Figure S44: ^{1}H,^{13}C-HMBC NMR spectrum of **mes-DBAF-N$_2$** (600/151 MHz, 323 K, THF-d_8).

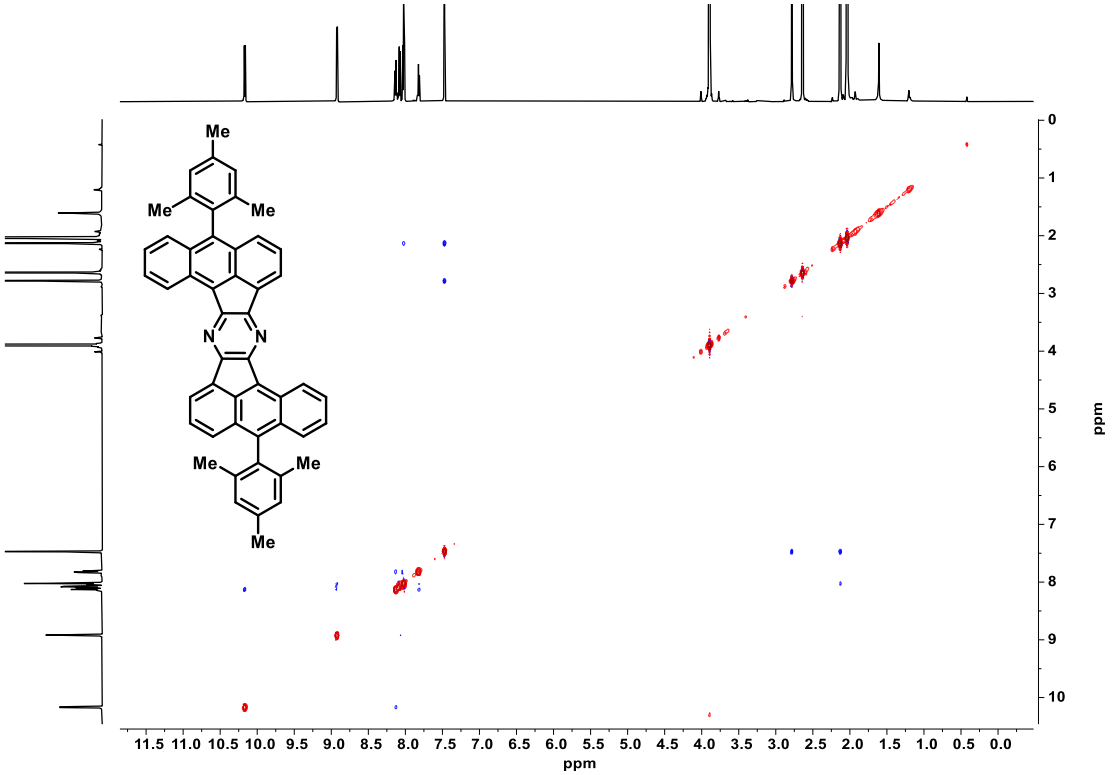

Figure S45: ^{1}H,^{1}H-NOESY NMR spectrum of **mes-DBAF-N$_2$** (600/600 MHz, 323 K, THF-d_8).

4. FTIR Spectroscopy

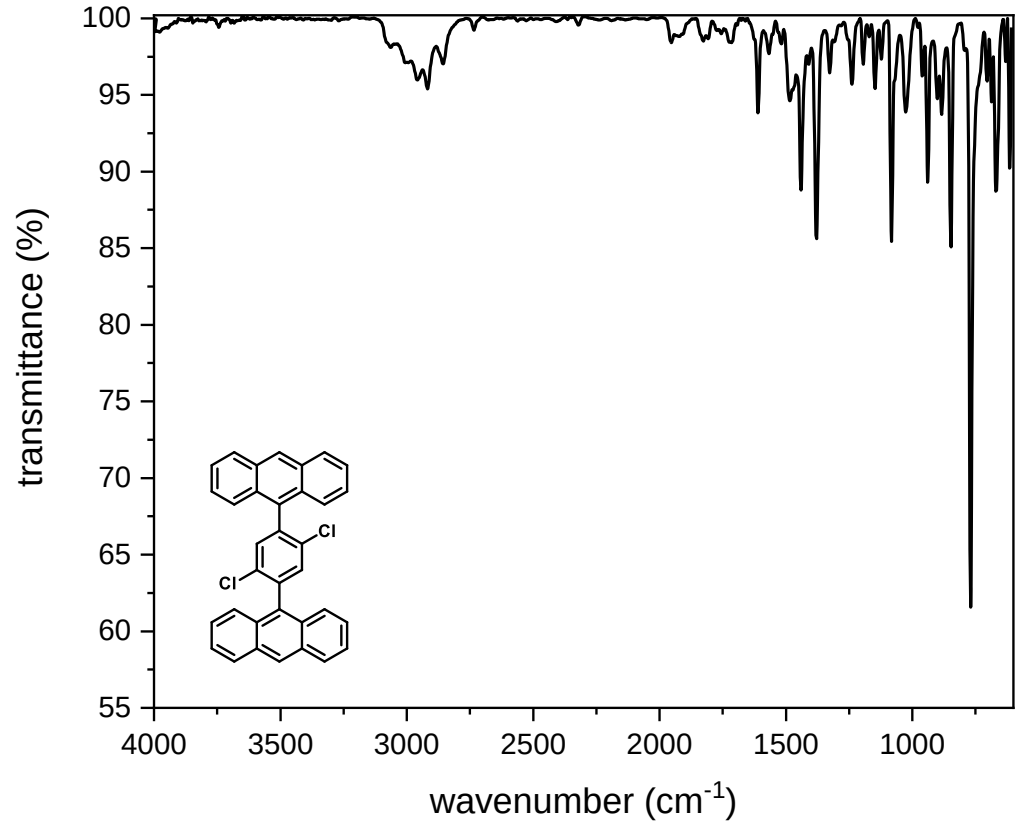

Figure S46: FT-IR spectrum of compound **5** (ATR, ZnSe).

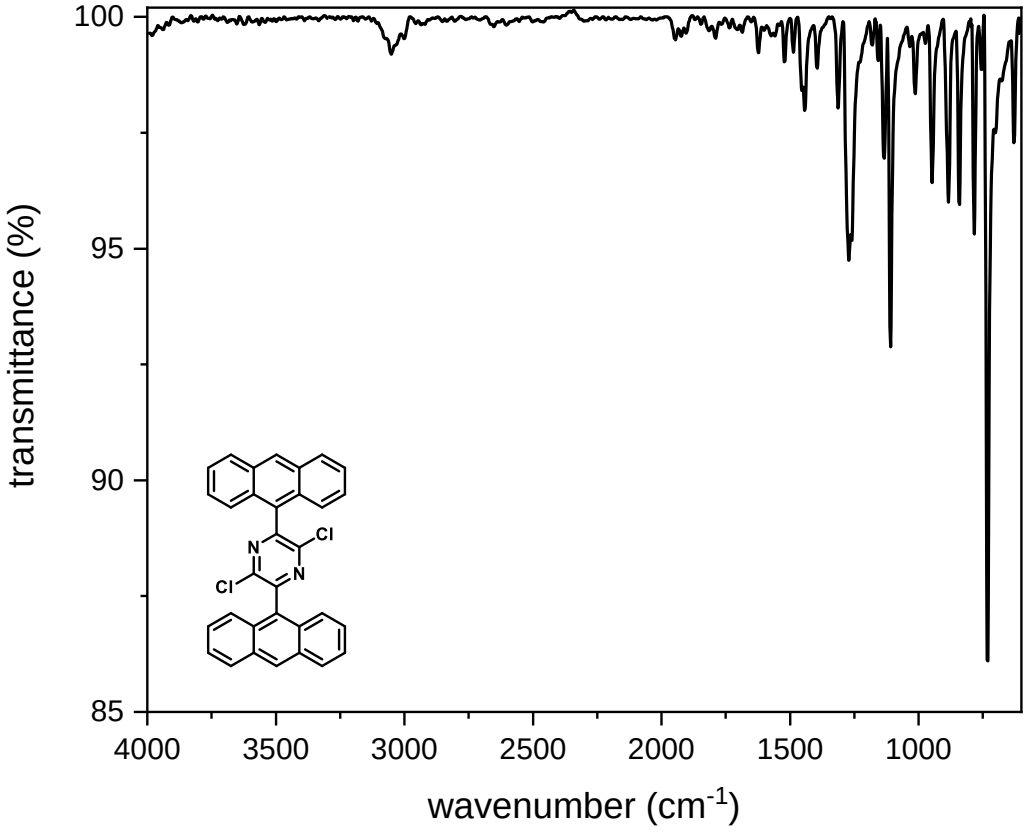

Figure S47: FT-IR spectrum of compound **6** (ATR, ZnSe).

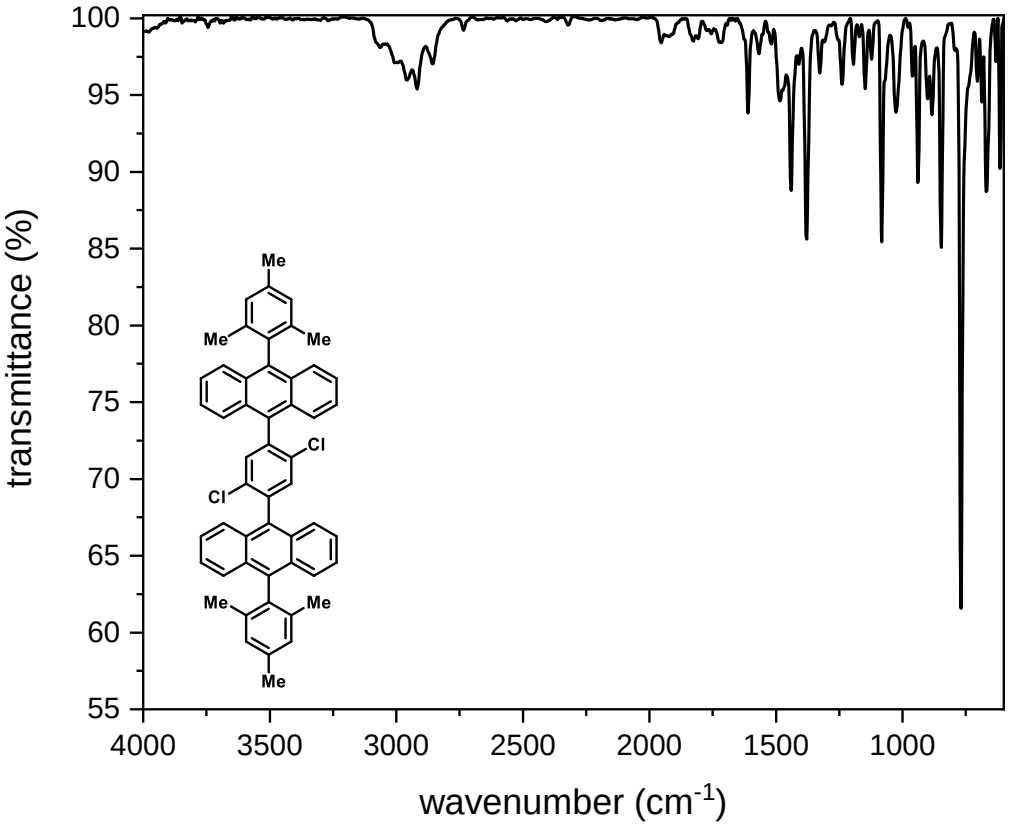

Figure S48: FT-IR spectrum of compound **7** (ATR, ZnSe).

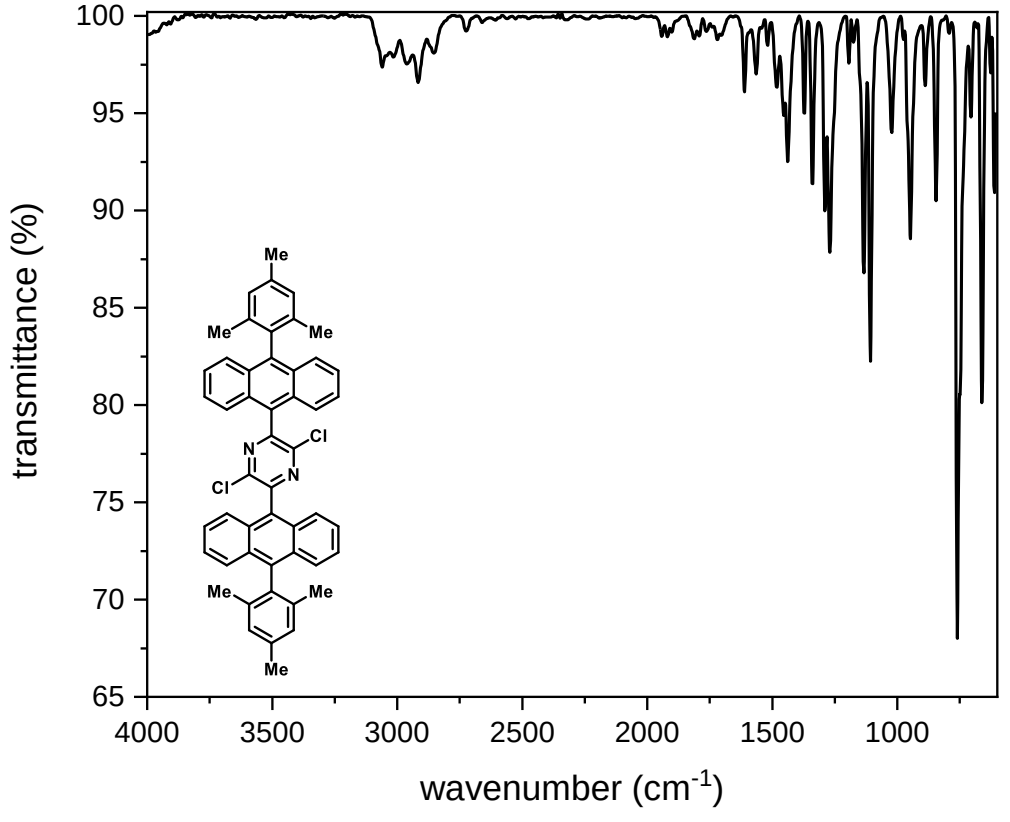

Figure S49: FT-IR spectrum of compound **8** (ATR, ZnSe).

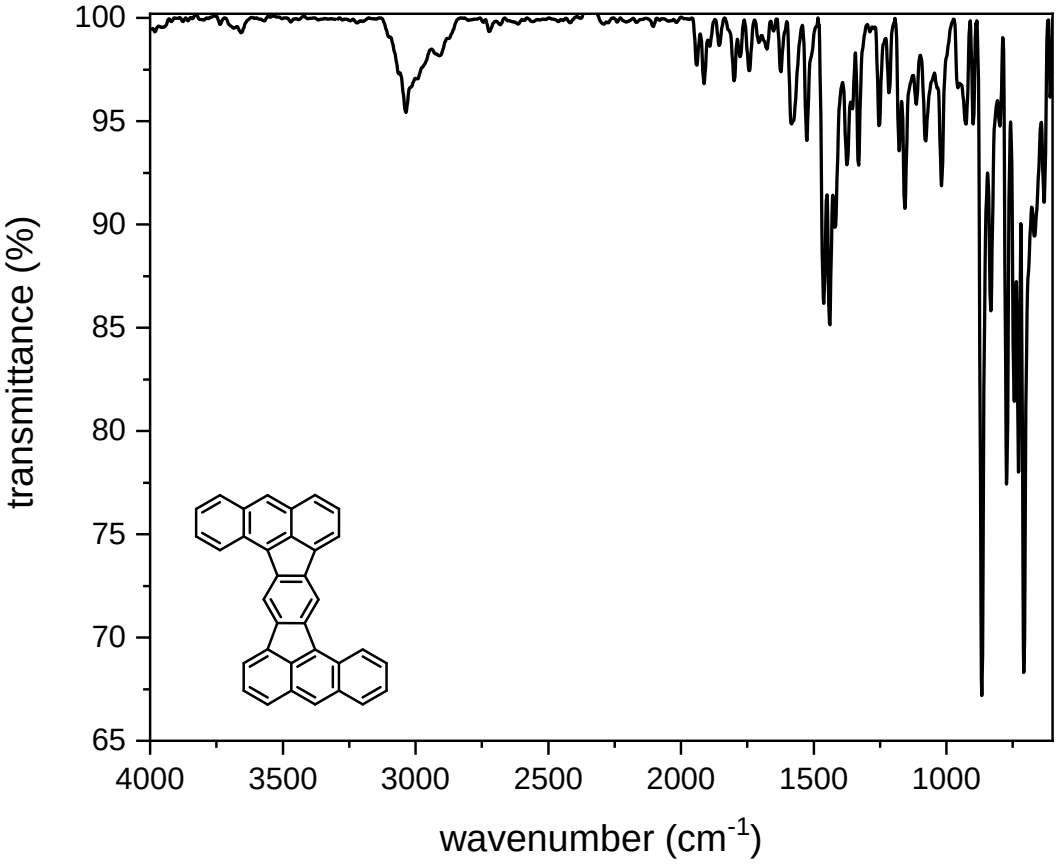

Figure S50: FT-IR spectrum of **DBAF** (ATR, ZnSe).

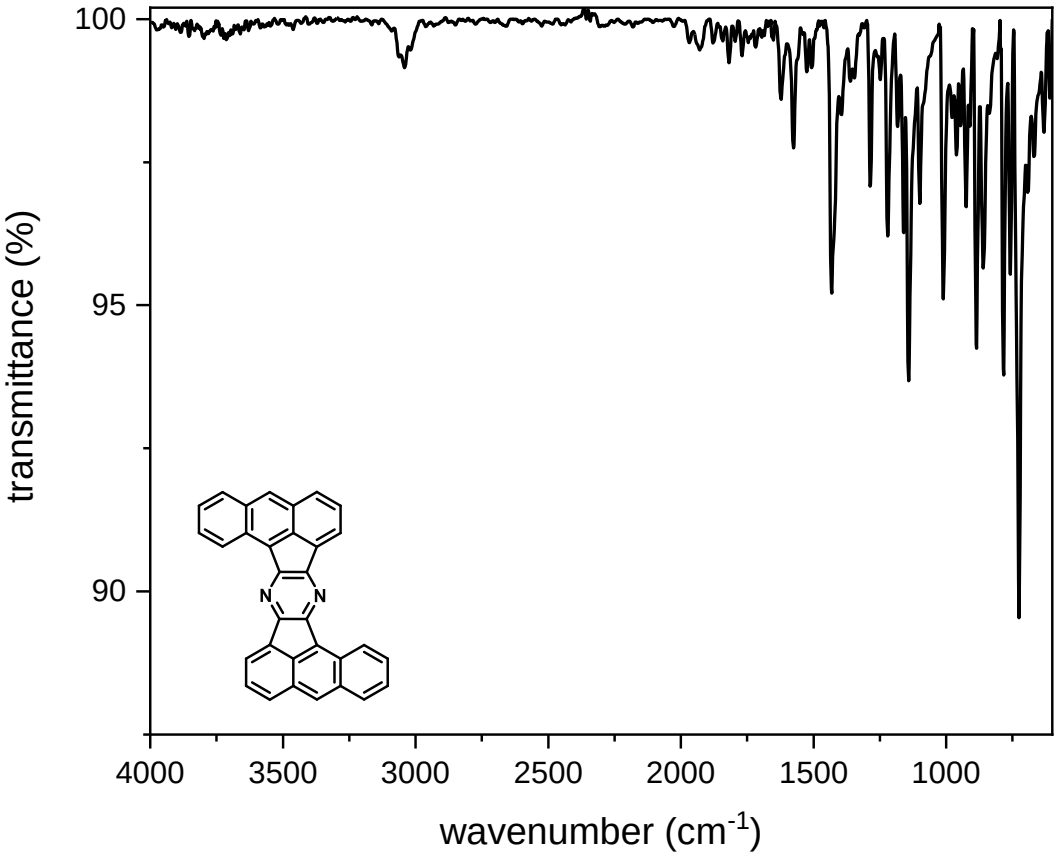

Figure S51: FT-IR spectrum of **DBAF-N_2** (ATR, ZnSe).

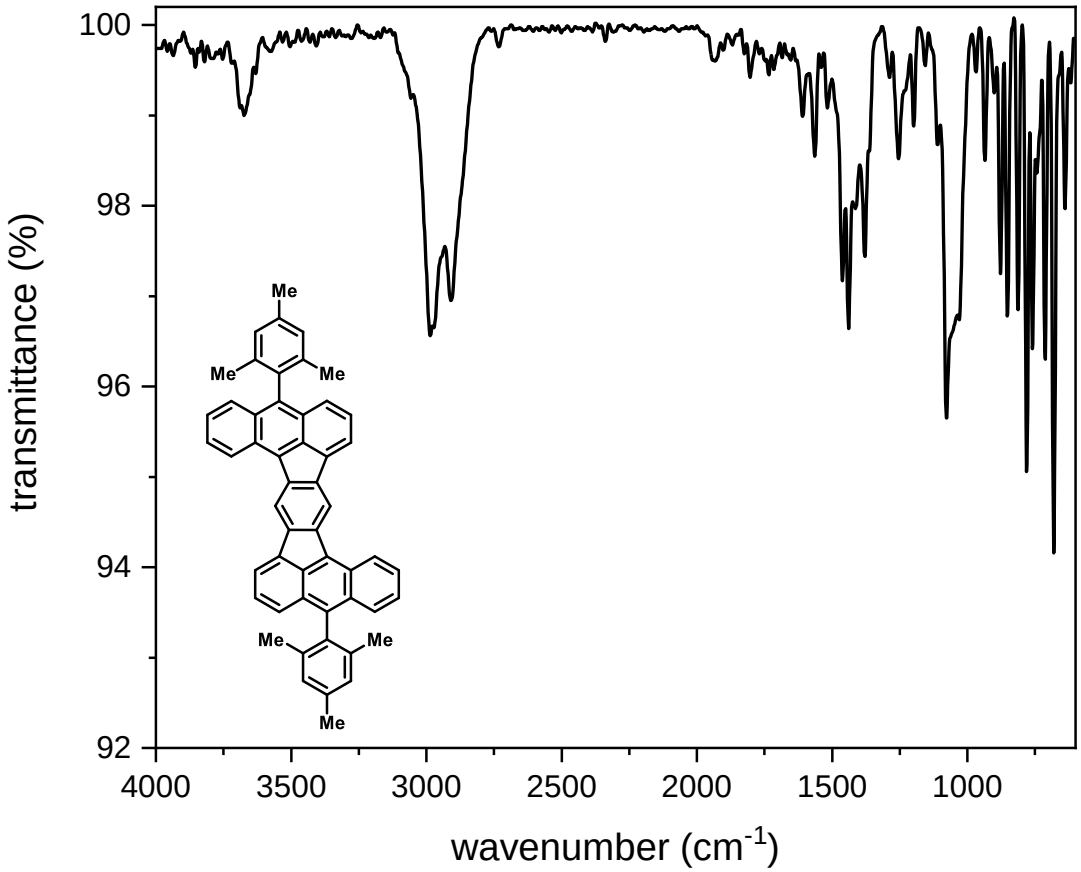

Figure S52: FT-IR spectrum of **mes-DBAF** (ATR, ZnSe).

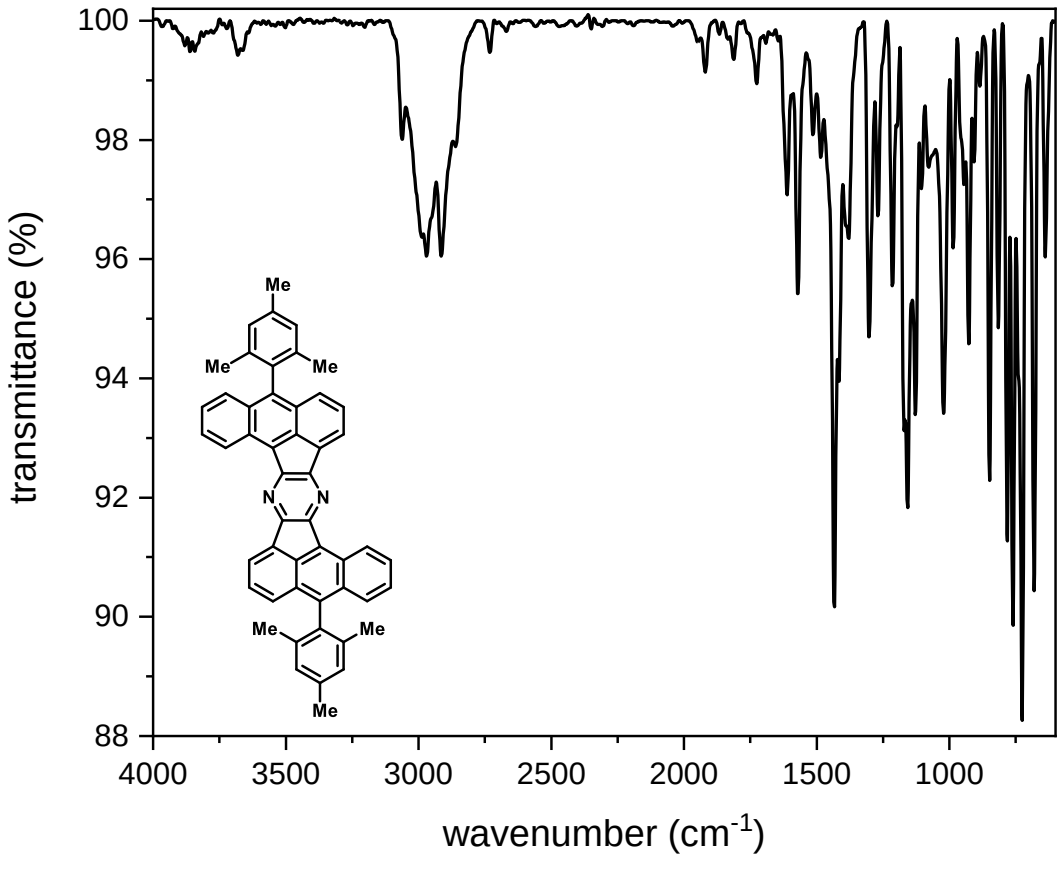

Figure S53: FT-IR spectrum of **mes-DBAF-N_2** (ATR, ZnSe).

5. Mass Spectrometry

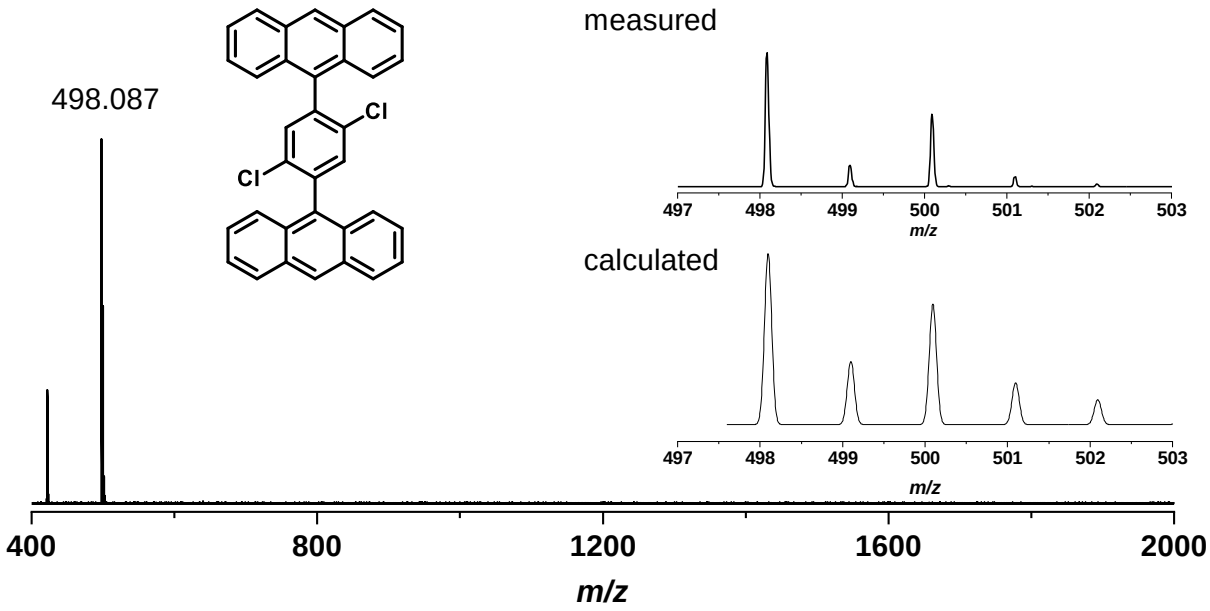

Figure S54: MALDI-TOF mass spectrum (pos. DCTB) of compound **5**.

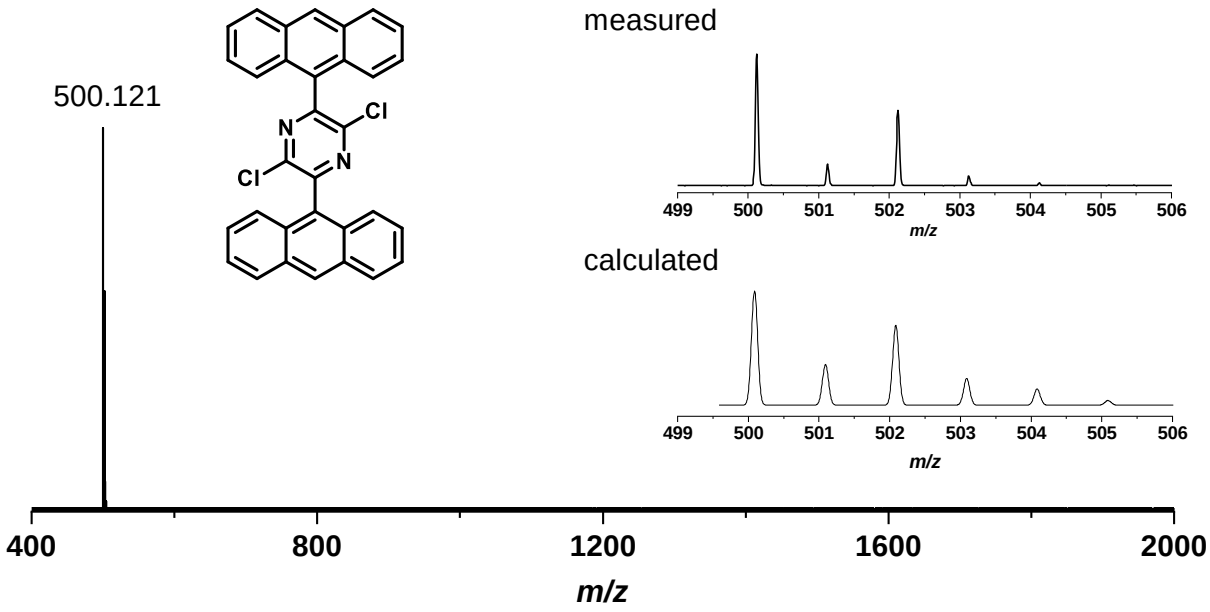

Figure S55: MALDI-TOF mass spectrum (pos. DCTB) of compound **6**.

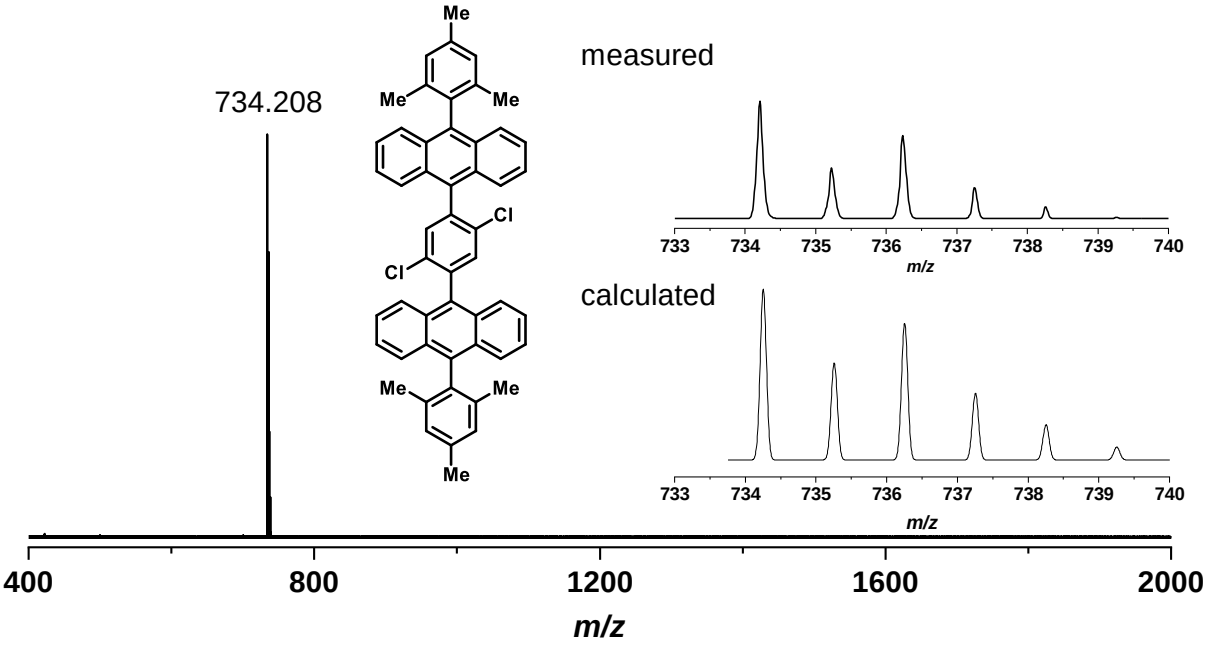

Figure S56: MALDI-TOF mass spectrum (pos. DCTB) of compound **7**.

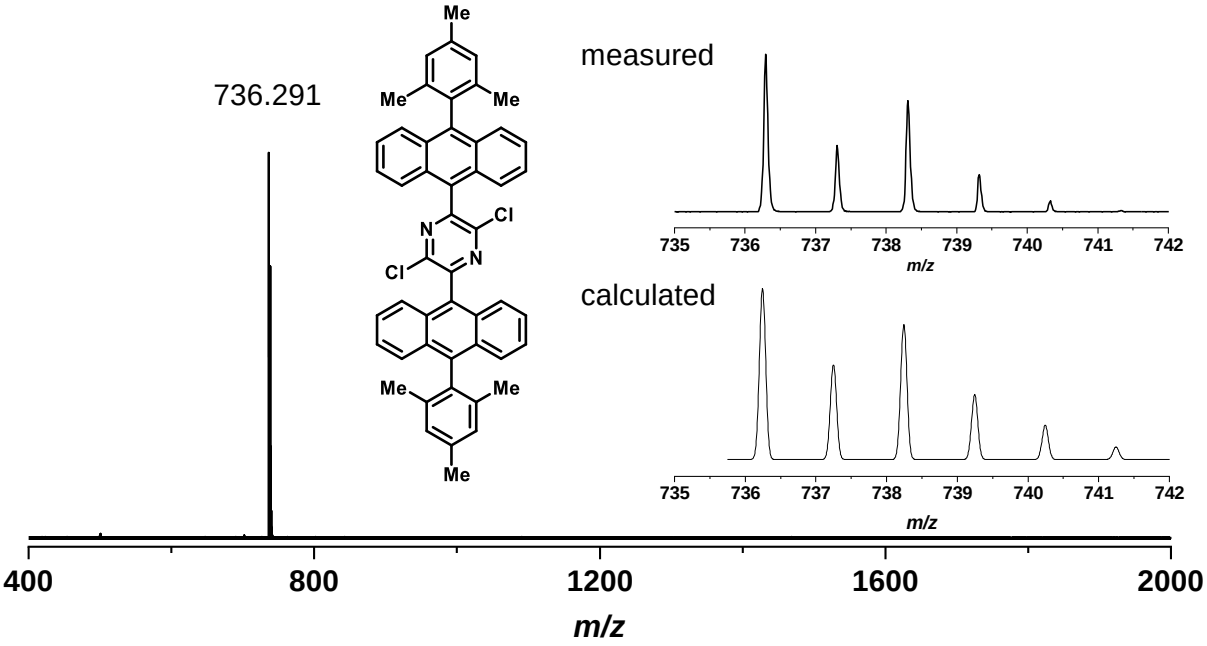

Figure S57: MALDI-TOF mass spectrum (pos. DCTB) of compound **8**.

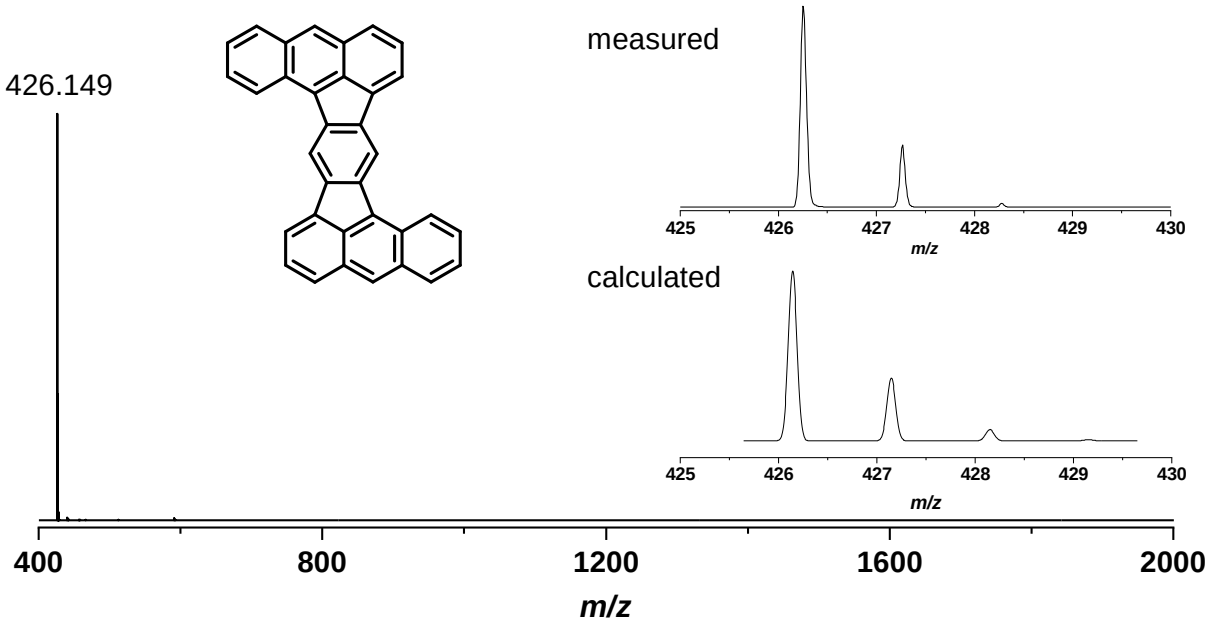

Figure S58: MALDI-TOF mass spectrum (pos. DCTB) of **DBAF**.

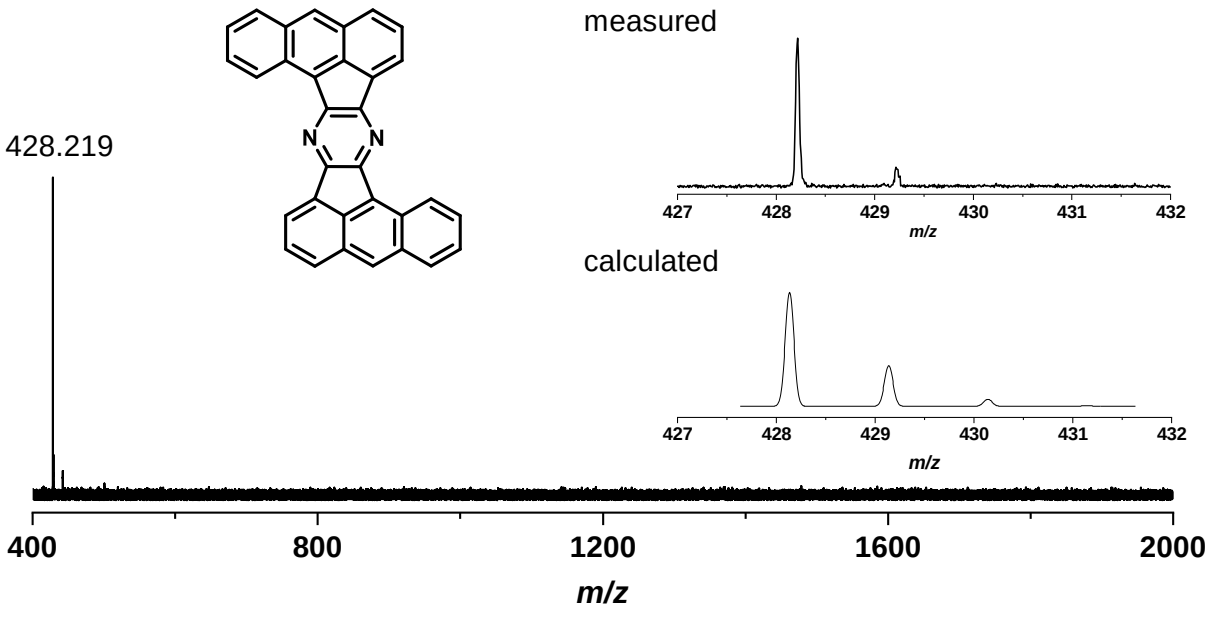

Figure S59: MALDI-TOF mass spectrum (pos. DCTB) of **DBAF-N_2**.

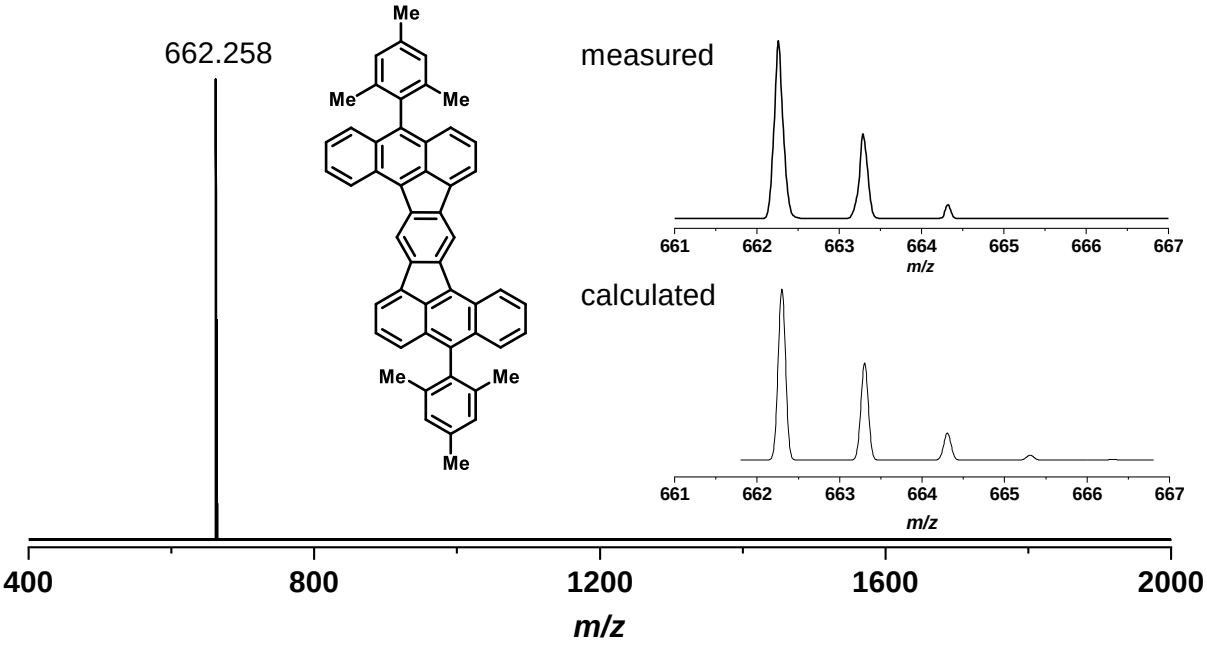

Figure S60: MALDI-TOF mass spectrum (pos. DCTB) of **mes-DBAF**.

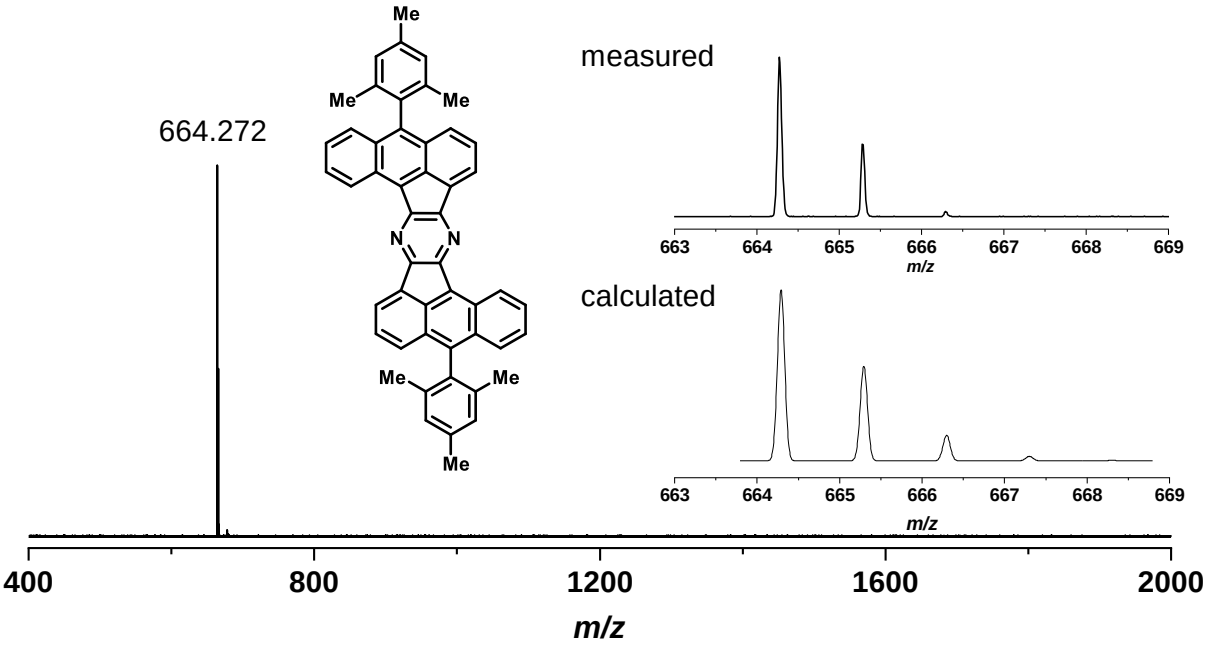

Figure S61: MALDI-TOF mass spectrum (pos. DCTB) of **mes-DBAF-N_2**.

6. UV/vis and Fluorescence Spectrometry

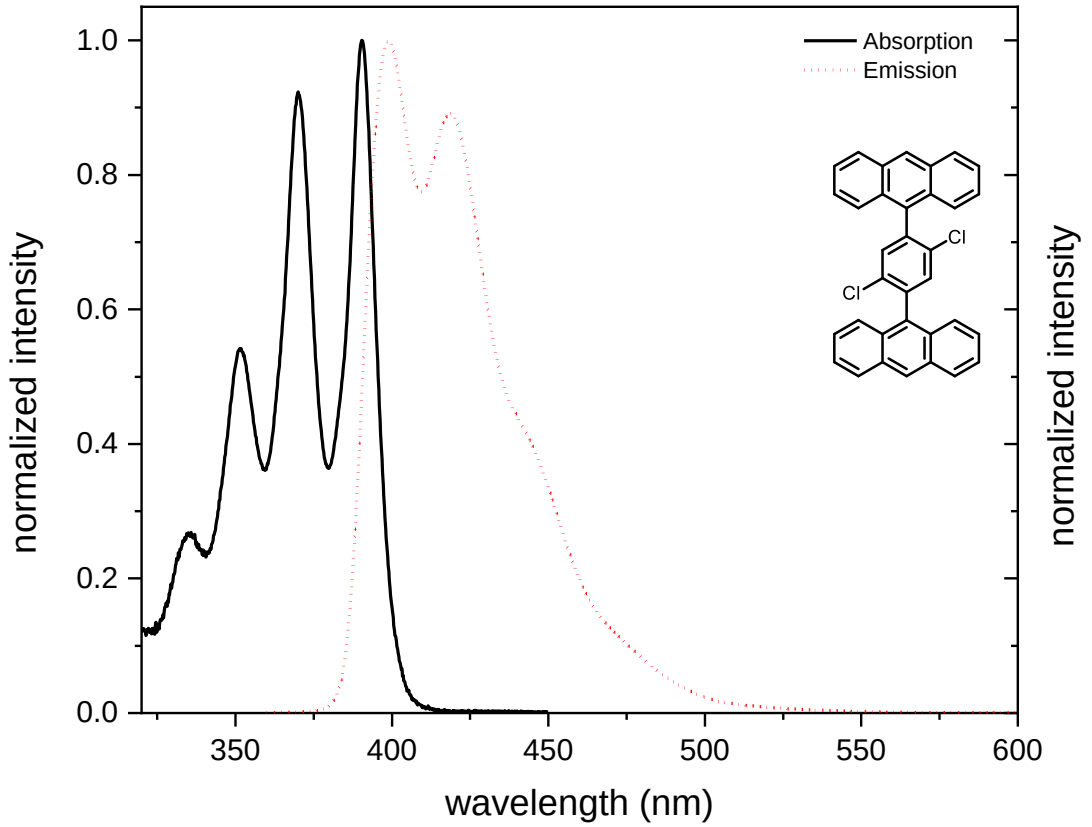

Figure S62: UV/vis (black) and emission (red) spectra of compound **5** measured in oDCB at room temperature.

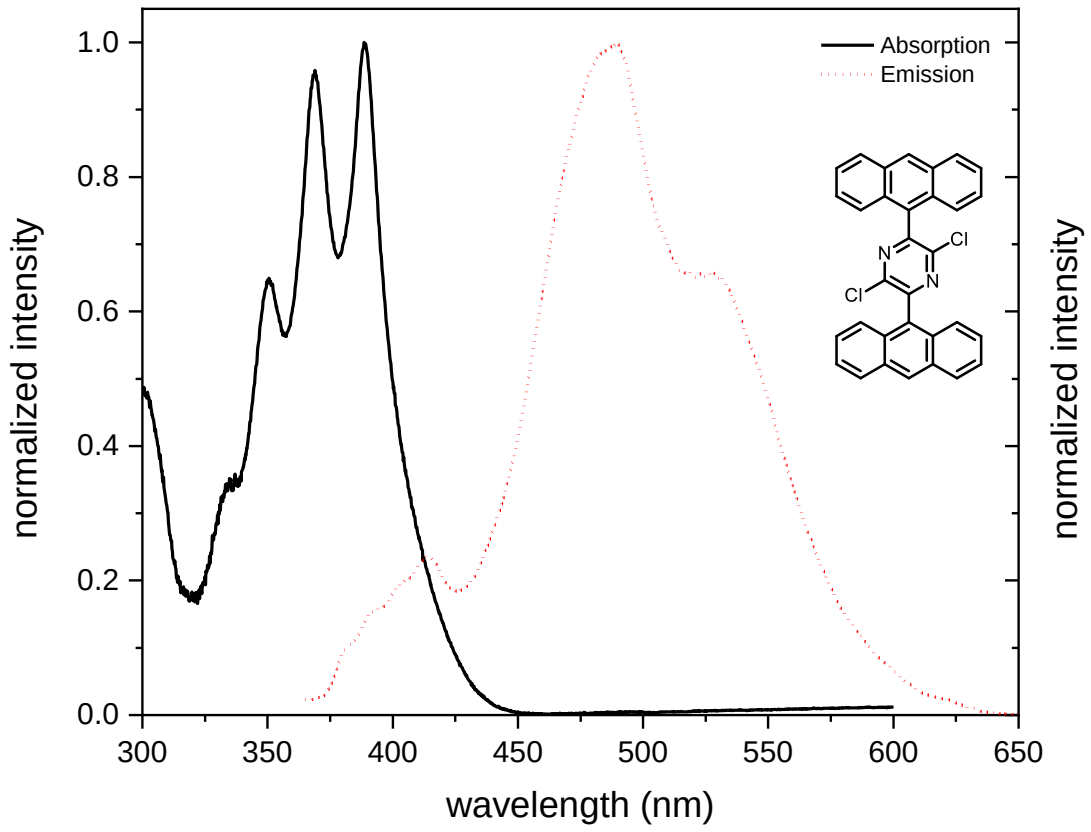

Figure S63: UV/vis (black) spectra of compound **6** measured in CH_2Cl_2 at room temperature.

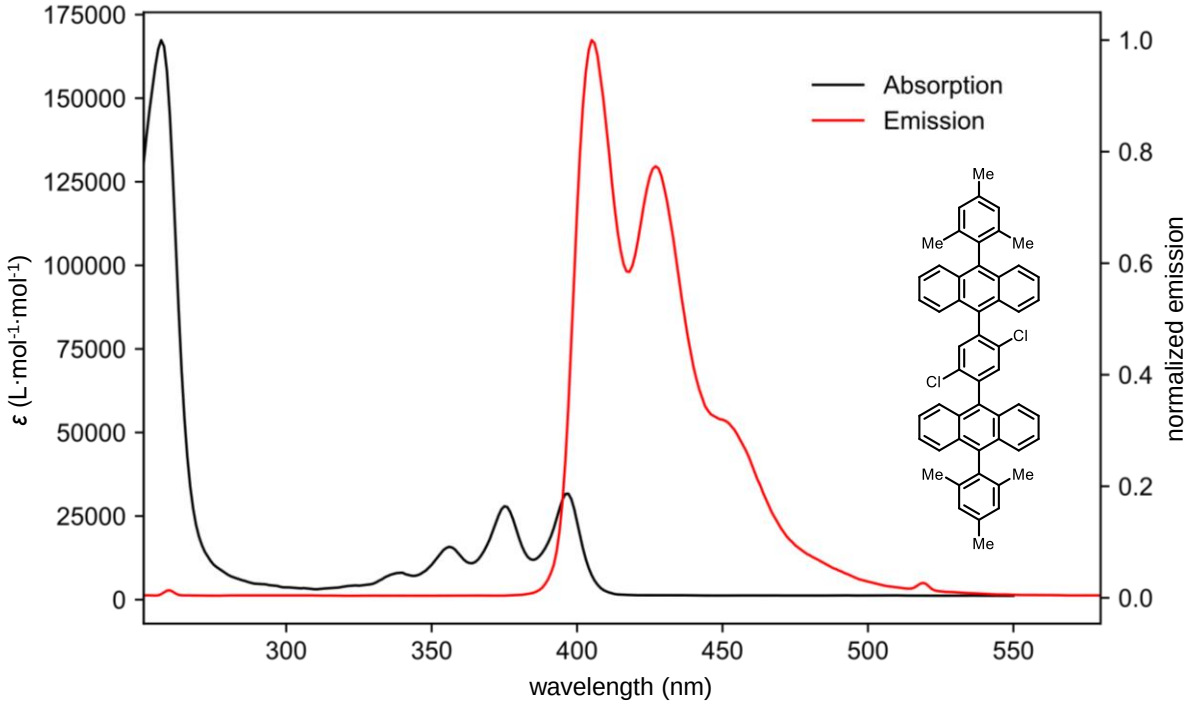

Figure S64: UV/vis (black) and emission (red) spectra of compound **7** measured in CH_2Cl_2 at room temperature.

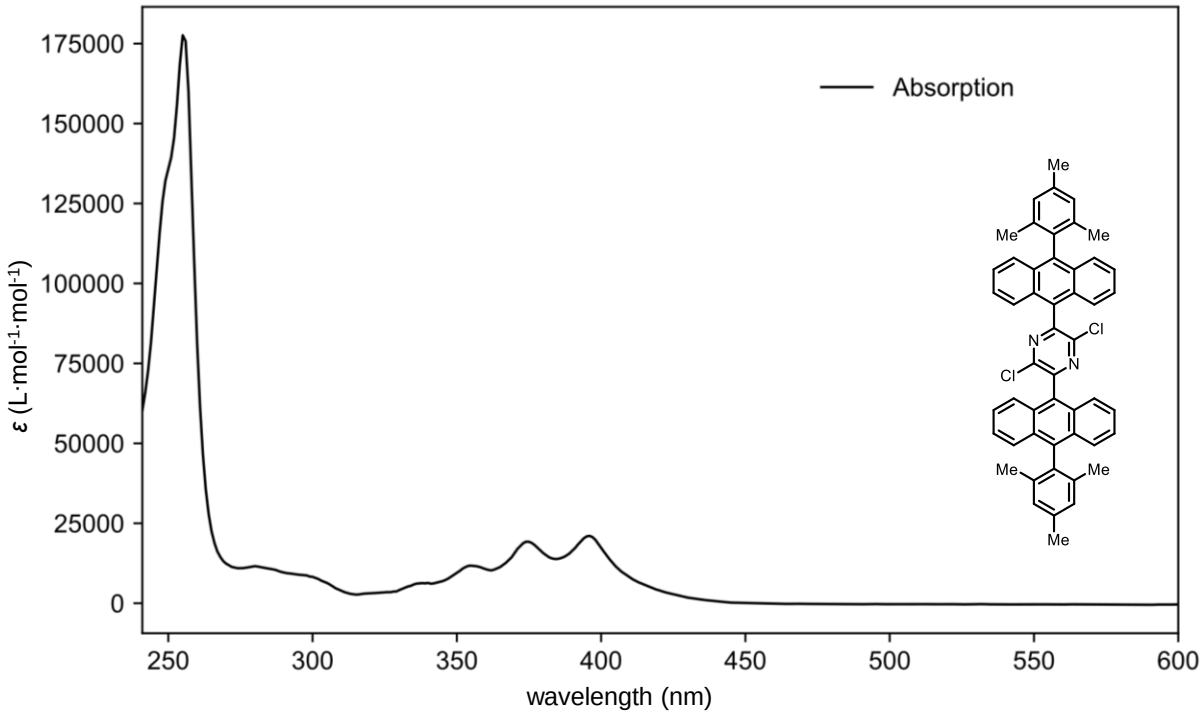

Figure S65: UV/vis (black) spectra of compound **8** measured in CH_2Cl_2 at room temperature.

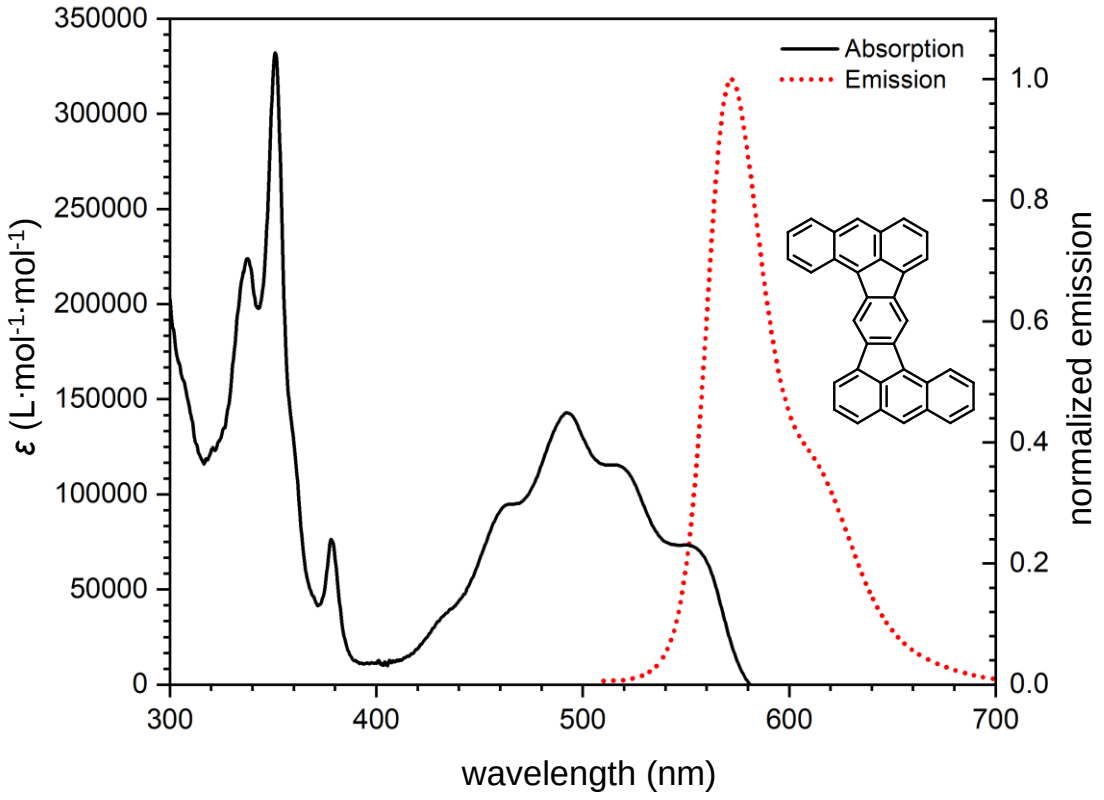

Figure S66: UV/vis (black) and emission (red, dotted) spectra of compound **DBAF** measured in oDCB at room temperature.

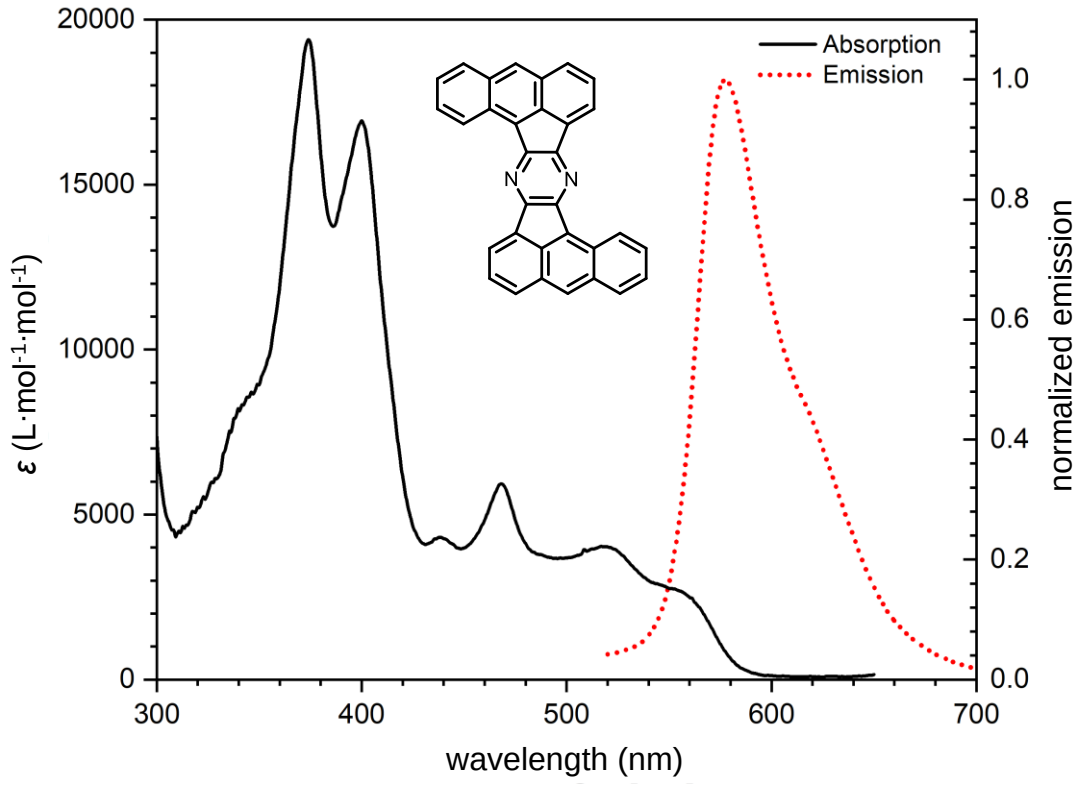

Figure S67: UV/vis (black) and emission (red, dotted) spectra of compound **DBAF-N_2** measured in oDCB at room temperature.

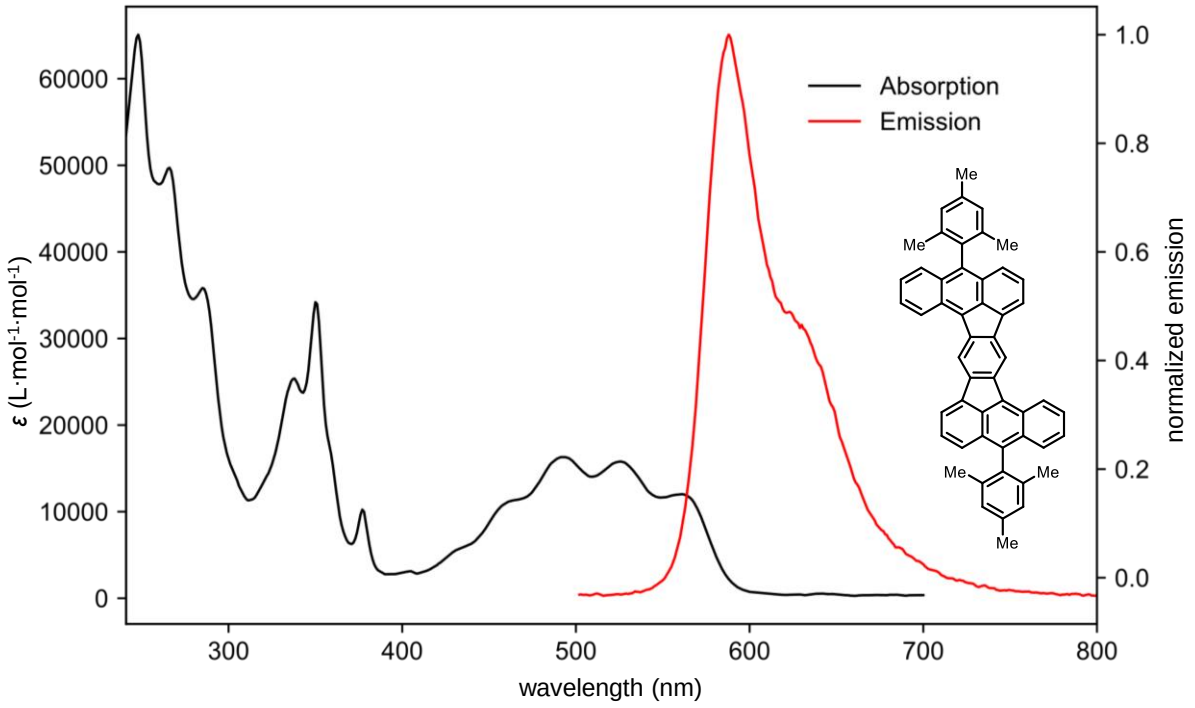

Figure S68: UV/vis (black) and emission (red) spectra of compound **mes-DBAF** measured in CH_2Cl_2 at room temperature.

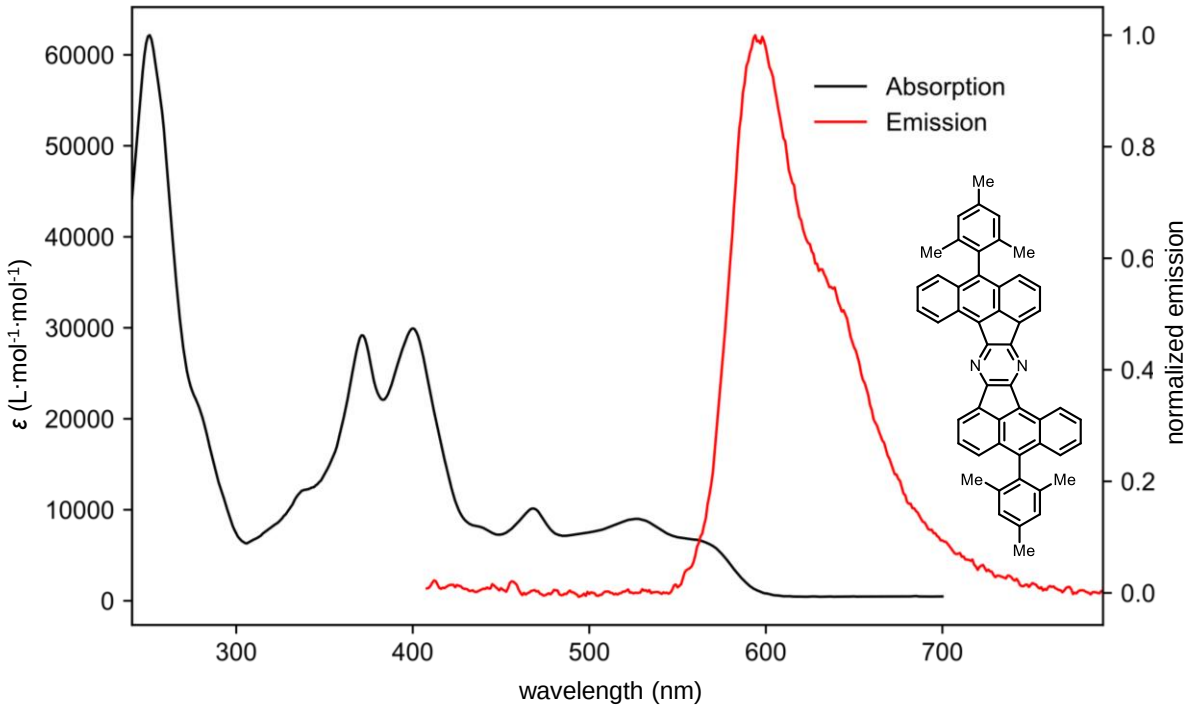

Figure S69: UV/vis (black) and emission (red) spectra of compound **mes-DBAF-N_2** measured in CH_2Cl_2 at room temperature.

7. Crystallographic Data

7.1. Compound 5

Crystals of **5** suitable for single crystal X-ray diffraction were obtained by thermal recrystallization from oDCB.

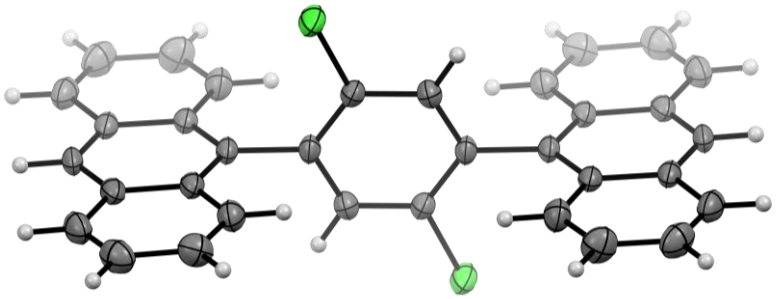

CCDC-number	2353527	
Empirical formula	$C_{34}H_{20}Cl_2$	
Formula weight	499.40	
Temperature	200(2) K	
Wavelength	0.71073 Å	
Crystal system	monoclinic	
Space group	$P2_1/n$	
Z	2	
Unit cell dimensions	a = 11.3543(14) Å	α = 90 deg.
	b =7.0091(9) Å	β =91.237(3) deg.
	c = 14.5933(18) Å	γ = 90 deg.
Volume	1161.1(3) Å^3	
Density (calculated)	1.43 g/cm^3	
Absorption coefficient	0.30 mm^{-1}	
Crystal shape	prism	
Crystal size	0.155 x 0.120 x 0.038 mm^3	
Crystal colour	yellow	
Theta range for data collection	2.2 to 28.4 deg.	
Index ranges	-15≤h≤14, -9≤k≤8, -19≤l≤19	
Reflections collected	12148	
Independent reflections	2667 (R(int) = 0.0539)	
Observed reflections	1862 (I > 2σ(I))	
Absorption correction	Semi-empirical from equivalents	
Max. and min. transmission	0.96 and 0.92	
Refinement method	Full-matrix least-squares on F^2	
Data/restraints/parameters	2667 / 0 / 163	
Goodness-of-fit on F^2	1.04	
Final R indices (I>2sigma(I))	R1 = 0.047, wR2 = 0.092	
Largest diff. peak and hole	0.30 and -0.26 eÅ^{-3}	

7.2. Compound 6

Crystals of **6** suitable for single crystal X-ray diffraction were obtained by vapour phase diffusion of hexane in into a saturated chloroform solution of **6**.

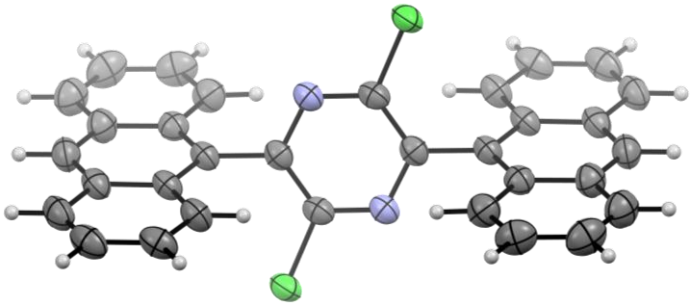

CCDC-number	2353528	
Empirical formula	$C_{32}H_{18}Cl_2N_2$	
Formula weight	501.38	
Temperature	200(2) K	
Wavelength	1.54178 Å	
Crystal system	monoclinic	
Space group	$P2_1/n$	
Z	2	
Unit cell dimensions	a =8.4735(5) Å	α = 90 deg.
	b =8.1885(3) Å	β =94.305(5) deg.
	c = 16.7772(10) Å	γ = 90 deg.
Volume	1160.81(11) $Å^3$	
Density (calculated)	1.43 g/cm^3	
Absorption coefficient	2.71 mm^{-1}	
Crystal shape	plank	
Crystal size	0.062 x 0.025 x 0.010 mm^3	
Crystal colour	yellow	
Theta range for data collection	6.0 to 68.9 deg.	
Index ranges	$-9\leq h\leq 10$, $-5\leq k\leq 9$, $-20\leq l\leq 17$	
Reflections collected	11856	
Independent reflections	2051 (R(int) = 0.1363)	
Observed reflections	1259 ($I > 2\sigma(I)$)	
Absorption correction	Semi-empirical from equivalents	
Max. and min. transmission	1.00 and 1.00	
Refinement method	Full-matrix least-squares on F^2	
Data/restraints/parameters	2051 / 157 / 173	
Goodness-of-fit on F^2	1.01	
Final R indices (I>2sigma(I))	R1 = 0.048, wR2 = 0.095	
Largest diff. peak and hole	0.17 and -0.20 $eÅ^{-3}$	

7.3. Compound 7

Crystals of **7** suitable for single crystal X-ray diffraction were obtained by evaporation of a saturated $CDCl_3$ solution of **7**.

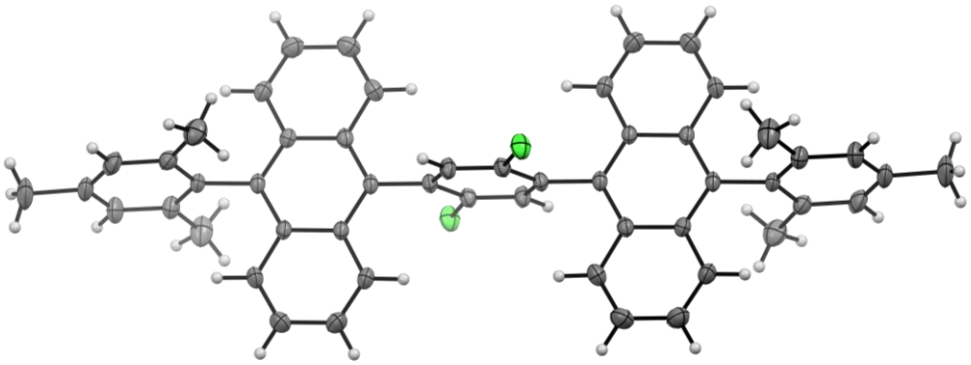

CCDC-number	2353529	
Empirical formula	$C_{54}H_{42}Cl_8$	
Formula weight	974.47	
Temperature	200(2) K	
Wavelength	0.71073 Å	
Crystal system	triclinic	
Space group	P $\bar{1}$	
Z	1	
Unit cell dimensions	a =8.4307(5) Å	α =101.3934(17) deg.
	b =8.8836(5) Å	β =100.9581(16) deg.
	c = 16.8457(10) Å	γ = 103.7267(16) deg.
Volume	1163.68(12) $Å^3$	
Density (calculated)	1.39 g/cm^3	
Absorption coefficient	0.52 mm^{-1}	
Crystal shape	plate	
Crystal size	0.230 x 0.062 x 0.028 mm^3	
Crystal colour	colourless	
Theta range for data collection	2.4 to 31.1 deg.	
Index ranges	$-12 \le h \le 12$, $-12 \le k \le 12$, $-23 \le l \le 24$	
Reflections collected	25481	
Independent reflections	7120 (R(int) = 0.0531)	
Observed reflections	4428 ($I > 2\sigma(I)$)	
Absorption correction	Semi-empirical from equivalents	
Max. and min. transmission	0.96 and 0.92	
Refinement method	Full-matrix least-squares on F^2	
Data/restraints/parameters	7120 / 0 / 283	
Goodness-of-fit on F^2	1.03	
Final R indices (I>2sigma(I))	R1 = 0.056, wR2 = 0.125	
Largest diff. peak and hole	0.77 and -0.80 $eÅ^{-3}$	

7.4. Compound 8

Crystals of **8** suitable for single crystal X-ray diffraction were obtained by evaporation of a saturated $CDCl_3$ solution of **8**.

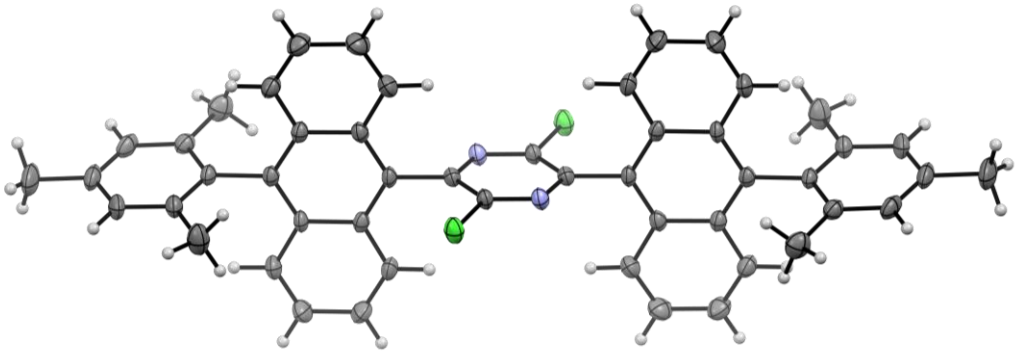

CCDC-number	2353530	
Empirical formula	$C_{52}H_{40}Cl_8N_2$	
Formula weight	976.46	
Temperature	200(2) K	
Wavelength	0.71073 Å	
Crystal system	triclinic	
Space group	P $\bar{1}$	
Z	1	
Unit cell dimensions	a =8.3208(10) Å	α = 102.240(3) deg.
	b =8.8810(11) Å	β =99.833(3) deg.
	c = 16.692(2) Å	γ =103.716(3) deg.
Volume	1138.9(2) $Å^3$	
Density (calculated)	1.42 g/cm^3	
Absorption coefficient	0.53 mm^{-1}	
Crystal shape	plate	
Crystal size	0.108 x 0.052 x 0.010 mm^3	
Crystal colour	colourless	
Theta range for data collection	1.3 to 27.0 deg.	
Index ranges	$-10 \le h \le 10$, $-11 \le k \le 11$, $-21 \le l \le 21$	
Reflections collected	20391	
Independent reflections	4907 (R(int) = 0.0713)	
Observed reflections	3003 ($I > 2\sigma(I)$)	
Absorption correction	Semi-empirical from equivalents	
Max. and min. transmission	0.96 and 0.92	
Refinement method	Full-matrix least-squares on F^2	
Data/restraints/parameters	4907 / 0 / 283	
Goodness-of-fit on F^2	1.02	
Final R indices (I>2sigma(I))	R1 = 0.054, wR2 = 0.105	
Largest diff. peak and hole	0.43 and -0.58 $eÅ^{-3}$	

7.5. DBAF

Crystals of **DBAF** suitable for single crystal X-ray diffraction were obtained by thermal recrystallization from oDCB.

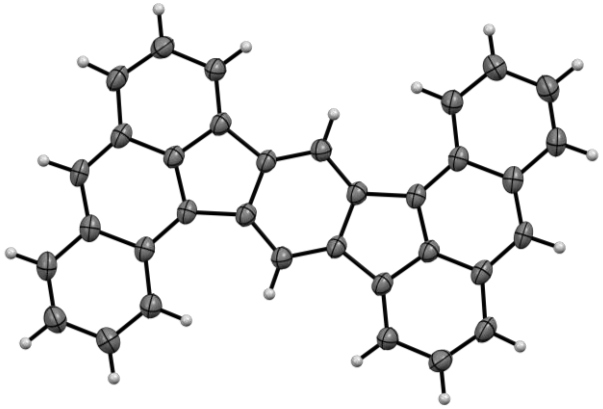

CCDC-number	2353531	
Empirical formula	$C_{34}H_{18}$	
Formula weight	426.48	
Temperature	200(2) K	
Wavelength	1.54178 Å	
Crystal system	monoclinic	
Space group	$P2_1/n$	
Z	2	
Unit cell dimensions	a =7.8885(4) Å	α = 90 deg.
	b = 12.3614(6) Å	β =98.462(4) deg.
	c = 10.6250(5) Å	γ = 90 deg.
Volume	1024.80(9) $Å^3$	
Density (calculated)	1.38 g/cm^3	
Absorption coefficient	0.60 mm^{-1}	
Crystal shape	prism	
Crystal size	0.048 x 0.036 x 0.020 mm^3	
Crystal colour	red	
Theta range for data collection	5.5 to 68.5 deg.	
Index ranges	$-9 \le h \le 5$, $-12 \le k \le 14$, $-10 \le l \le 12$	
Reflections collected	8017	
Independent reflections	1856 (R(int) = 0.0414)	
Observed reflections	1216 ($I > 2\sigma(I)$)	
Absorption correction	Semi-empirical from equivalents	
Max. and min. transmission	0.99 and 0.91	
Refinement method	Full-matrix least-squares on F^2	
Data/restraints/parameters	1856 / 0 / 154	
Goodness-of-fit on F^2	1.05	
Final R indices (I>2sigma(I))	R1 = 0.050, wR2 = 0.114	
Largest diff. peak and hole	0.19 and -0.17 $eÅ^{-3}$	

7.6. DBAF-N_2

Crystals of **DBAF-N_2** suitable for single crystal X-ray diffraction were obtained by sublimation at a kugelrohr apparatus (< $1 \cdot 10^{-3}$ mbar, 300 °C).

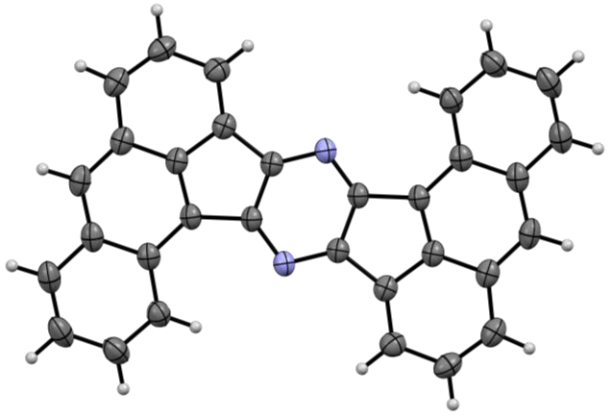

CCDC-number	2353532	
Empirical formula	$C_{32}H_{16}N_2$	
Formula weight	428.47	
Temperature	200(2) K	
Wavelength	0.71073 Å	
Crystal system	monoclinic	
Space group	$P2_1/n$	
Z	2	
Unit cell dimensions	a = 10.8037(16) Å	α = 90 deg.
	b =5.7081(9) Å	β =100.465(2) deg.
	c = 16.724(3) Å	γ = 90 deg.
Volume	1014.2(3) Å^3	
Density (calculated)	1.40 g/cm^3	
Absorption coefficient	0.08 mm^{-1}	
Crystal shape	irregular	
Crystal size	0.267 x 0.043 x 0.037 mm^3	
Crystal colour	orange	
Theta range for data collection	2.5 to 28.4 deg.	
Index ranges	$-14 \leq h \leq 14$, $-7 \leq k \leq 7$, $-22 \leq l \leq 22$	
Reflections collected	10502	
Independent reflections	2476 (R(int) = 0.0442)	
Observed reflections	1697 ($I > 2\sigma(I)$)	
Absorption correction	Semi-empirical from equivalents	
Max. and min. transmission	0.96 and 0.86	
Refinement method	Full-matrix least-squares on F^2	
Data/restraints/parameters	2476 / 0 / 154	
Goodness-of-fit on F^2	1.07	
Final R indices (I>2sigma(I))	R1 = 0.053, wR2 = 0.135	
Largest diff. peak and hole	0.20 and -0.16 eÅ^{-3}	

7.7. mes-DBAF

Crystals of **mes-DBAF** suitable for single crystal X-ray diffraction were obtained by evaporation of a saturated $CDCl_3$ solution of **mes-DBAF**.

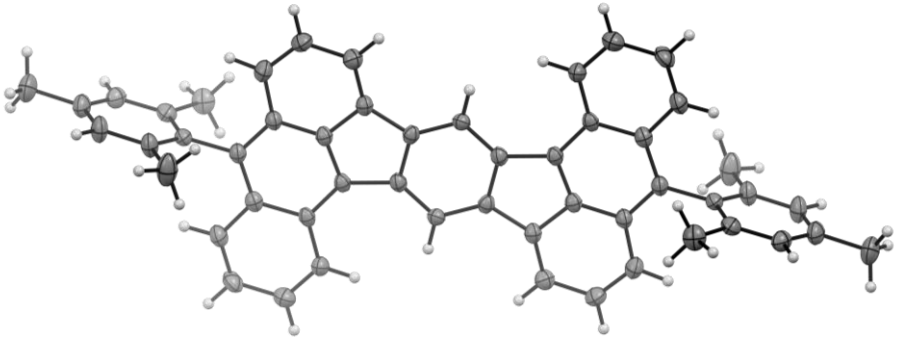

CCDC-number	2353533	
Empirical formula	$C_{54}H_{40}Cl_6$	
Formula weight	901.56	
Temperature	200(2) K	
Wavelength	0.71073 Å	
Crystal system	monoclinic	
Space group	$P2_1/n$	
Z	2	
Unit cell dimensions	a =9.1598(15) Å	α = 90 deg.
	b = 20.446(3) Å	β =104.773(4) deg.
	c = 12.1314(18) Å	γ = 90 deg.
Volume	2196.9(6) Å^3	
Density (calculated)	1.36 g/cm^3	
Absorption coefficient	0.43 mm^{-1}	
Crystal shape	column	
Crystal size	0.143 x 0.031 x 0.015 mm^3	
Crystal colour	red	
Theta range for data collection	2.0 to 22.7 deg.	
Index ranges	$-9\leq h\leq 9$, $-22\leq k\leq 22$, $-13\leq l\leq 13$	
Reflections collected	17113	
Independent reflections	2952 (R(int) = 0.0946)	
Observed reflections	1780 ($I > 2\sigma(I)$)	
Absorption correction	Semi-empirical from equivalents	
Max. and min. transmission	0.96 and 0.88	
Refinement method	Full-matrix least-squares on F^2	
Data/restraints/parameters	2952 / 342 / 291	
Goodness-of-fit on F^2	1.01	
Final R indices (I>2sigma(I))	R1 = 0.058, wR2 = 0.128	
Largest diff. peak and hole	0.42 and -0.43 eÅ^{-3}	

7.8. mes-DBAF-N_2

Crystals of **mes-DBAF-N_2** suitable for single crystal X-ray diffraction were obtained by vapor phase diffusion of hexane in into a saturated chloroform solution of **mes-DBAF-N_2**.

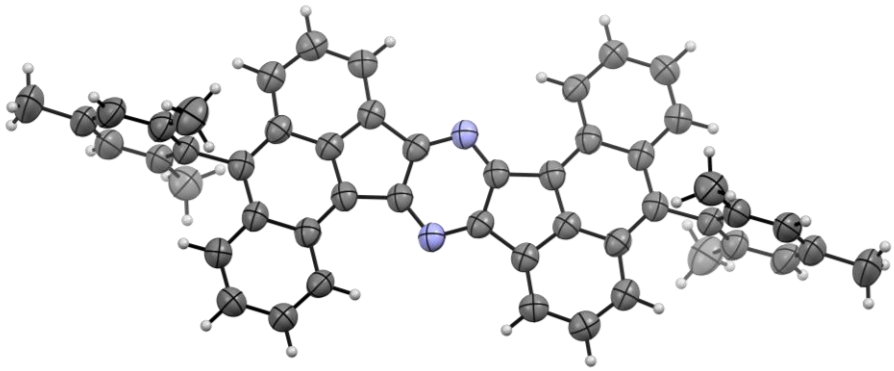

CCDC-number	2353534	
Empirical formula	$C_{51}H_{37}Cl_3N_2$	
Formula weight	784.17	
Temperature	200(2) K	
Wavelength	1.54178 Å	
Crystal system	triclinic	
Space group	$P\bar{1}$	
Z	2	
Unit cell dimensions	a =7.5160(3) Å	α =94.217(3) deg.
	b = 15.7823(6) Å	β =96.767(3) deg.
	c = 17.4357(6) Å	γ =101.960(3) deg.
Volume	1998.99(13) $Å^3$	
Density (calculated)	1.30 g/cm^3	
Absorption coefficient	2.37 mm^{-1}	
Crystal shape	needle	
Crystal size	0.180 x 0.027 x 0.010 mm^3	
Crystal colour	red	
Theta range for data collection	2.6 to 68.6 deg.	
Index ranges	$-5\leq h\leq 9$, $-18\leq k\leq 15$, $-21\leq l\leq 20$	
Reflections collected	29825	
Independent reflections	7124 (R(int) = 0.0424)	
Observed reflections	4564 ($I > 2\sigma(I)$)	
Absorption correction	Semi-empirical from equivalents	
Max. and min. transmission	0.99 and 0.87	
Refinement method	Full-matrix least-squares on F^2	
Data/restraints/parameters	7124 / 138 / 548	
Goodness-of-fit on F^2	1.04	
Final R indices (I>2sigma(I))	R1 = 0.076, wR2 = 0.187	
Largest diff. peak and hole	0.37 and -0.42 $eÅ^{-3}$	

8. Quantum Chemical Calculation

8.1. Frontier Molecular Orbitals

Calculations were performed using Gaussian 16, manipulation of obtained results were performed using Gaussview.[S11] The Frontier Molecular Orbitals Calculation of frontier molecular orbitals was achieved by generating a formatted checkpoint file after single point calculation using DFT-methods (u-B3LYP/6-31G(d,p)) [S12-22] with an isosurface value of 0.02.

8.2. Transfer Integrals and Theoretical Mobilities

Fragment based non-adiabatic molecular dynamics (NAMD) simulations were performed using the fewest switches surface hopping algorithm (FSSH), implemented in a local version of GROMACS 4.6[S23] The methodology details are described in Ref. S24. This computational approach is based on the partitioning of the crystal super-cell into classical and quantum regions. The propagation of the excess charge carrier is restricted in the quantum chemical (QM) region, while the remainder of the crystal is treated with molecular mechanics (MM). The wave function of the charge carrier, ψ, is expressed as the linear combination of frontier orbitals of the fragments (HOMO/LUMO), ϕ_m , in the QM zone.

$$\psi = \sum_A \sum_{m \in A} a_m |\phi_m >$$

Fragmentation of the QM zone makes it possible to use a coarse-grained model Hamiltonian matrix where the diagonal elements represent site energies (HOMO/LUMO energies of the fragments) and the off-diagonal elements are couplings between two fragments J. The corresponding Hamiltonian matrix elements, $H\ mn = <\phi\ m \mid H \mid \phi\ n>$, are computed using the nonself-consistent variant of the density functional tight-binding method (DFTB) as discussed in ref S25. Moreover, it is found that using an uniform scaling factor results in an accuracy comparable to high-level ab initio methods.[26] Therefore, in the present work, the DFTB electronic couplings, *J*, were scaled by a factor of 1.54 and 1.79 for hole and electron transport, respectively. Charge carriers wave function is propagated using time dependent Schrödinger equation (TDSE) coupled to the classical motion of the nuclei. Quantum forces cause a relaxation in the geometry of the molecular fragment, resulting in a modification of the site energy H_{mm}. In Marcus theory, this relaxation is characterized by the inner-sphere relaxation parameter λ. When one site is charged, the site energy decreases by λ. To account

for the charge relaxation effect on the electronic system, the on-site energy Hmm is reduced by a pre-calculated parameter, weighted by the charge occupation on site m. We refer to this method as implicit relaxation (IR). Details of this approach outlined in ref S23. The charge carrier mobility is calculated using Einstein Smoluchowski relation $\mu = eD/k\ \ BT$ where *e* is the elementary charge, k_B is the Boltzmann factor and *T* is the absolute temperature. The diffusion coefficient, *D*, is calculated by

$$D = \frac{1}{2n} \lim_{t \to \infty} \frac{dMSD(t)}{dt}$$

where n is the dimensionality (n = 1 for 1D system) and mean square displacement of the charge carrier, MSD, is defined as

$$MSD(t) = \frac{1}{N_{\text{traj}}} \sum_{l}^{N_{\text{traj}}} \sum_{A} (x_A(t)^{(l)} - x_0^l)^2 P(t)^{(l)}(t)$$

where $x_A(t)^l$ and $P(t)^{(l)}$are the center of mass of molecule A and corresponding charge population along the trajectory l, respectively. $x\ \ 0\text{^}\ \ l$ is the center of charge at *t* = 0.

It has been demonstrated that this method can accurately reproduce experimental results.15 Below, we detail the NAMD simulations. [23]

Super-cell structures of the investigated molecular crystals were generated based on crystallographic data from experiments, expanded in various directions to make the simulation boxes. The resulting structures were equilibrated using an NVT ensemble at 300 K with a Nose-Hoover thermostat[S27] for 1 ns and a time step of 2 fs. The General Amber Force Field (GAFF)[S28] was employed for these simulations. Atomic partial charges were obtained through restrained electrostatic potential (RESP)[S29] fitting, calculated by the Hartree-Fock (HF) method with a 6-311G(p,d) basis set.[S30] The molecular geometries were optimized using Density Functional Theory (DFT) with the B3LYP functional and the 6-311G(p,d) level of theory, implemented in Gaussian 16.[S31]

Subsequently, a production MD simulation was conducted for 1 ns with a 2 fs time step, sampling initial super-cell coordinates every 100 fs for the FSSH simulation. For each initial super-cell geometry, NAMD simulations were conducted for 1 ps with a 0.1 fs time step.[24-26]

The reorganization energy of the molecules was computed using DFT with B3LYP and ωB97xd functionals and a 6-31G(d,p) basis set, utilizing Gaussian 16 software.[S31] Average hole/electron transfer integrals <J> were calculated for 100,000 structures sampled from the NAMD simulation of the corresponding crystal over 100 ps with a 1 fs time step. In this simulation, a dimer in the relevant direction was included in the QM zone, with the charge localized on one of the monomers. The transfer integral calculations are detailed in Ref. S25 and S26. Table S1 shows the reorganization energies(RE) together with average coupling values <J>.

Table S1: Reorganization Energy (RE) and Average Hole/Electron coupling <J> of the π stack directions. All the values are in meV.

	Hole			Electron		
	RE (B3LYP)	RE(ωB97xd)	<J>	RE (B3LYP)	RE(ωB97xd)	<J>
DBAF	153	336	20±14	117	214	-46±30
DBAF-N_2	167	370	-70±24	105	182	54±18
mes-DBAF	161	346	3±2	123	222	11±5
mes-DBAF-N_2	176	381	-19±11	110	245	21±13

NAMD simulations of hole/electron transfer were conducted for the one-dimensional QM zone in crystals with the highest transfer integral values. For **DBAF**: 50 and **DBAF-N_2**: 85, **mes-DBAF**: 15, **mes-DBAF-N_2**: 35 molecules (from the corresponding π-stacked packing direction) were selected to constitute the QM zone. Table S2 shows the calculated mobility with different reorganization energies.

Table S2: Hole and electron mobility. All the values are in cm^2/Vs.

	Hole		Electron	
	FSSH-IR (B3LYP)	FSSH-IR (ωB97xd)	FSSH-IR (B3LYP)	FSSH-IR (ωB97xd)
DBAF	0.31	0.00	6.70	1.87
DBAF-N_2	14.41	0.58	23.65	5.46
mes-DBAF	0.00	0.00	0.53	0.00
mes-DBAF-N_2	0.07	0.00	0.95	0.00

9. Device Fabrication and Analysis

Organic thin-film transistors (TFTs) were fabricated on 125-µm-thick flexible polyethylene naphthalate (PEN) substrates (Inabata Europe GmbH, Düsseldorf, Germany). The TFTs were fabricated either in the inverted staggered (bottom-gate, top-contact) or in the inverted coplanar (bottom-gate, bottom-contact) device architecture.[S31] To define the gate electrodes, aluminum (Al) with a thickness of 25 nm was deposited by thermal evaporation in vacuum through a polyimide shadow mask (CADiLAC Laser, Hilpoltstein, Germany).[S32] The film thickness of the vacuum-deposited films was monitored using a quartz crystal microbalance. The surface of the Al gate electrodes was briefly exposed to oxygen plasma and subsequently functionalized with a self-assembled monolayer (SAM) of *n*-tetradecylphosphonic acid (PCI Synthesis, Newburyport, MA, U.S.A.) to form a hybrid AlO_x/SAM gate dielectric with a thickness of 8 nm and a unit-area capacitance of 0.7 µF/cm^2.[S33] For the TFTs fabricated in the staggered (top-contact) device architecture, the next process step is the deposition of the organic-semiconductor layer, followed by the deposition of the source and drain contacts. The organic semiconductor (**DBAF** or **DBAF-N_2**) was deposited by thermal sublimation in vacuum through a polyimide shadow mask and has a nominal thickness of 30 nm. During the semiconductor deposition, the substrate was held at a temperature of 60 or 80 °C. To define the source and drain contacts, gold (Au) with a thickness of 30 nm was deposited by thermal evaporation in vacuum through a polyimide shadow mask. For the TFTs fabricated in the coplanar (bottom-contact) device architecture, the source and drain contacts were deposited prior to the organic semiconductor. In this case, the surface of the source and drain contacts was functionalized with a chemisorbed monolayer of pentafluorobenzenethiol (PFBT; TCI Deutschland GmbH, Eschborn, Germany) by immersing the substrates into a 10 mM ethanol solution of PFBT for 5 h, with the purpose of minimizing the contact resistance of the TFTs.[S31] In the last process step, the organic semiconductor was deposited by thermal sublimation in vacuum through a polyimide shadow mask, with a nominal thickness of 30 nm. The TFTs have a channel length of 30 µm and a channel width of 100 µm. The current-voltage characteristics of the TFTs were recorded using a manual probe station connected to an Agilent 4156C Semiconductor Parameter Analyzer. All measurements were performed in ambient air at room temperature. From the measured transfer characteristics, the effective charge-carrier mobilities were extracted using the equation $I_D = \mu_{eff} \cdot C_{diel} \cdot W \cdot (V_{GS}-V_{th})^2/(2 \cdot L)$, where I_D is the

drain current, μ_{eff} is the effective charge-carrier mobility, C_{diel} is the unit-area gate-dielectric capacitance (0.7 μF/cm^2), W is the channel width (100 μm), V_{GS} is the gate-source voltage, V_{th} is the threshold voltage, and L is the channel length (30 μm). [S34] The measured current-voltage characteristics of the TFTs and atomic force microscopy (AFM images of the vacuum-deposited organic-semiconductor films are shown in Figures S70-74.

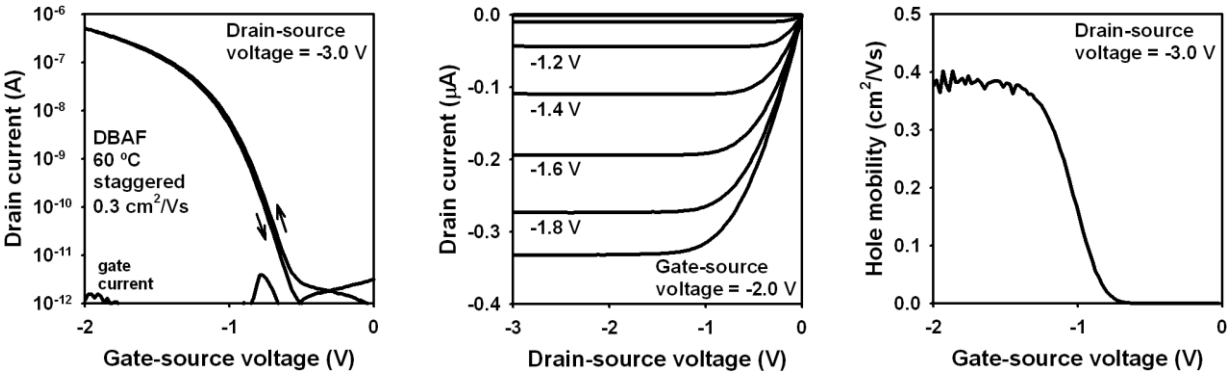

Figure S70: Electrical characteristics of a **DBAF** TFT fabricated in the inverted staggered (bottom-gate, top-contact) device architecture, with the substrate held at a temperature of 60 ºC during the semiconductor deposition. The effective charge-carrier mobility is 0.3 cm^2/Vs

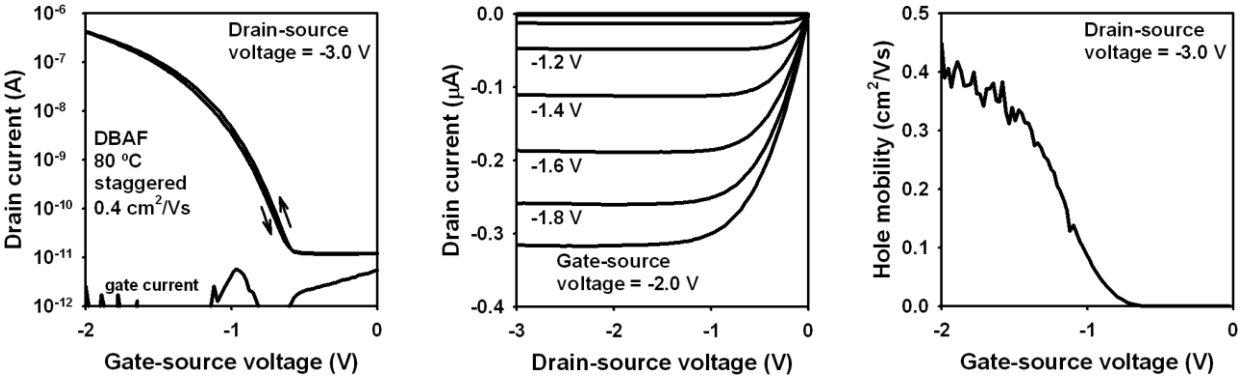

Figure S71: Electrical characteristics of a **DBAF** TFT fabricated in the inverted staggered (bottom-gate, top-contact) device architecture, with the substrate held at a temperature of 80 ºC during the semiconductor deposition. The effective charge-carrier mobility is 0.4 cm^2/Vs.

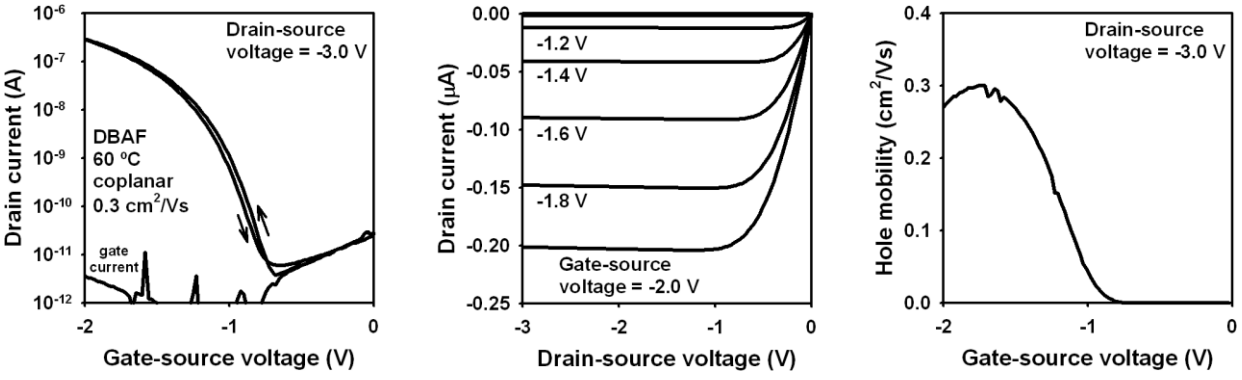

Figure S72: Electrical characteristics of a **DBAF** TFT fabricated in the inverted coplanar (bottom-gate, bottom-contact) device architecture, with the substrate held at a temperature of 60 ºC during the semiconductor deposition. The effective charge-carrier mobility is 0.3 cm2/Vs.

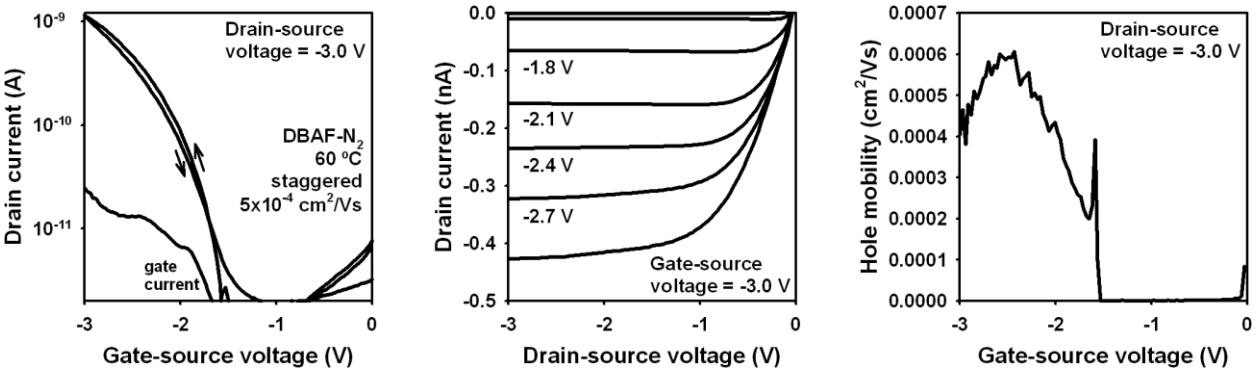

Figure S73: Electrical characteristics of a **DBAF-N_2** TFT fabricated in the inverted staggered (bottom-gate, top-contact) device architecture, with the substrate held at a temperature of 60 ºC during the semiconductor deposition. The effective charge-carrier mobility is 5×10^{-4} cm^2/Vs.

Table S1: Summary of the effective charge-carrier mobilities extracted from the measured current-voltage characteristics of the TFTs.

semiconductor	device architecture	substrate temperature during semiconductor deposition	
		60 °C	80 °C
DBAF	staggered	0.3 cm^2/Vs	0.4 cm^2/Vs
	coplanar	not tested	0.3 cm^2/Vs
DBAF-N_2	staggered	5×10^{-4} cm^2/Vs	not tested
	coplanar	not tested	not tested

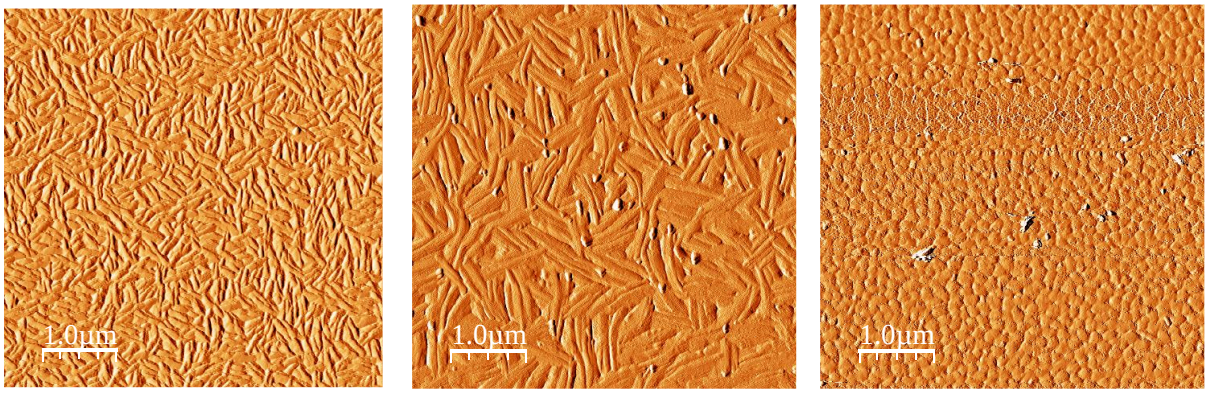

Figure S74: Atomic force microscopy (AFM) amplitude images of a **DBAF** film deposited with the substrate held at a temperature of 60 ºC (left), of a **DBAF** film deposited with the substrate held at a temperature of 80 ºC (center), and of a **DBAF-N_2** film deposited with the substrate held at a temperature of 60 ºC (right).

10. References

S1. H. W. H. Lai, Y. C. Teo and Y. Xia, Functionalized Rigid Ladder Polymers from Catalytic Arene-Norbornene Annulation Polymerization, *ACS Macro Lett.*, 2017, **6**, 1357-1361.

S2. P. Meti, E.-S. Lee, J.-W. Yang and Y.-D. Gong, Regioselective synthesis of dipyrrolopyrazine (DPP) derivatives via metal free and metal catalyzed amination and investigation of their optical and thermal properties, *RSC Adv.*, 2017, **7**, 18120-18131.

S3. N. D. Shapiro, V. Rauniyar, G. L. Hamilton, J. Wu and F. D. Toste, Asymmetric additions to dienes catalysed by a dithiophosphoric acid, *Nature*, 2011, **470**, 245-249.

S4. C. H. E. Chow, H. Phan, X. Zhang and J. Wu, Sulfur-Doped (Dibenzo)heptazethrene and (Dibenzo)octazethrene Diradicaloids, *J. Org. Chem.*, 2020, **85**, 234-240.

S5. L. Valenta, M. Mayländer, P. Kappeler, O. Blacque, T. Šolomek, S. Richert and M. Juríček, Trimesityltriangulene: a persistent derivative of Clar's hydrocarbon, *Chem.Commun.* 2022, **58**, 3019-3022.

S6. C. Würth, M. Grabolle, J. Pauli, M. Spieles and U. Resch-Genger, Relative and absolute determination of fluorescence quantum yields of transparent samples, *Nat. Protocols*, 2013, **8**, 1535-1550.

S7. J. Koziskova, F. Hahn, J. Richter and J. Kožíšek, Comparison of different absorption corrections on the model structure of tetrakis(μ2-acetato)-diaqua-di-copper(II), *Acta Chim. Slov.*2016, **9**, 136-140.

S8. G. Sheldrick, SHELXT - Integrated space-group and crystal-structure determination, *Acta Crystallograp. A*, 2015, **71**, 3-8.

S9. G. Sheldrick, Crystal structure refinement with SHELXL, *Acta Crystallograph. C*, 2015, **71**, 3-8.

S10. J. Lubben, C. M. Wandtke, C. B. Hubschle, M. Ruf, G. M. Sheldrick and B. Dittrich, Aspherical scattering factors for SHELXL - model, implementation and application, *Acta Crystallograph. A*, 2019, **75**, 50-62.

S11. M. J. Frisch, G. W. Trucks, H. B. Schlegel, G. E. Scuseria, M. A. Robb, J. R. Cheeseman, G. Scalmani, V. Barone, G. A. Petersson, H. Nakatsuji, X. Li, M. Caricato, A. V. Marenich, J. Bloino, B. G. Janesko, R. Gomperts, B. Mennucci, H. P. Hratchian, J. V. Ortiz, A. F. Izmaylov, J. L. Sonnenberg, Williams, F. Ding, F. Lipparini, F. Egidi, J. Goings, B. Peng, A. Petrone, T. Henderson, D. Ranasinghe, V. G. Zakrzewski, J. Gao, N. Rega, G. Zheng, W. Liang, M. Hada, M. Ehara, K. Toyota, R. Fukuda, J. Hasegawa, M. Ishida, T. Nakajima, Y. Honda, O. Kitao, H. Nakai, T. Vreven, K. Throssell, J. A. Montgomery Jr., J. E. Peralta, F. Ogliaro, M. J. Bearpark, J. J. Heyd, E. N. Brothers, K. N. Kudin, V. N. Staroverov, T. A. Keith, R. Kobayashi, J. Normand, K. Raghavachari, A. P. Rendell, J. C. Burant, S. S. Iyengar, J. Tomasi, M. Cossi, J. M. Millam, M. Klene, C. Adamo, R. Cammi, J. W. Ochterski, R. L. Martin, K. Morokuma, O. Farkas, J. B. Foresman and D. J. Fox, Gaussian 16, Revision B.01/C.01, Gaussian Inc., Wallingford, CT, 2016

S12. R. Ditchfield, W. J. Hehre and J. A. Pople, Self-Consistent Molecular-Orbital Methods. IX. An Extended Gaussian-Type Basis for Molecular-Orbital Studies of Organic Molecules, *J. Chem. Phys.*, 1971, **54**, 724-728.

S13. W. J. Hehre, R. Ditchfield and J. A. Pople, Self-Consistent Molecular Orbital Methods. XII. Further Extensions of Gaussian-Type Basis Sets for Use in Molecular Orbital Studies of Organic Molecules, *J. Chem. Phys.*, 1972, **56**, 2257-2261.

S14. P. C. Hariharan and J. A. Pople, The influence of polarization functions on molecular orbital hydrogenation energies, *Theor. Chim. Acta*, 1973, **28**, 213-222.

S15. J. D. Dill and J. A. Pople, Self-consistent molecular orbital methods. XV. Extended Gaussian-type basis sets for lithium, beryllium, and boron, *J. Chem. Phys.*, 1975, **62**, 2921-2923.

S16. J. S. Binkley and J. A. Pople, Self-consistent molecular orbital methods. XIX. Split-valence Gaussian-type basis sets for beryllium, *J. Chem. Phys.*, 1977, **66**, 879-880.

S17. M. M. Francl, W. J. Pietro, W. J. Hehre, J. S. Binkley, M. S. Gordon, D. J. DeFrees and J. A. Pople, Self-consistent molecular orbital methods. XXIII. A polarization-type basis set for second-row elements, *J. Chem. Phys.*, 1982, **77**, 3654-3665.

S18. M. S. Gordon, J. S. Binkley, J. A. Pople, W. J. Pietro and W. J. Hehre, Self-consistent molecular-orbital methods. 22. Small split-valence basis sets for second-row elements, *J. Am. Chem. Soc.*, 1982, **104**, 2797-2803.

S19. S. H. Vosko, L. Wilk and M. Nusair, Accurate spin-dependent electron liquid correlation energies for local spin density calculations: a critical analysis, *Can. J. Phys.* 1980, **58**, 1200-1211.

S20. C. Lee, W. Yang and R. G. Parr, Development of the Colle-Salvetti correlation-energy formula into a functional of the electron density, *Phys. Rev. B*, 1988, **37**, 785-789.

S21. A. D. Becke, Density-functional thermochemistry. I. The effect of the exchange-only gradient correction, *J. Chem. Phys.* 1992, **96**, 2155-2160.

S22. A. D. Becke, Density-functional thermochemistry. III. The role of exact exchange, *J. Chem. Phys.* 1993, **98**, 5648-5652.

S23. S. Roosta, F. Ghalami, M. Elstner and W. Xie, Efficient Surface Hopping Approach for Modeling Charge Transport in Organic Semiconductors, *J. Chem. Theory Comput.* 2022, **18**, 1264-1274.

S24. W. Xie, D. Holub, T. Kubař and M. Elstner, Performance of Mixed Quantum-Classical Approaches on Modeling the Crossover from Hopping to Bandlike Charge Transport in Organic Semiconductors, *J. Chem. Theory Comput.* 2020, **16**, 2071-2084.

S25. A. Heck, J. J. Kranz, T. Kubař and M. Elstner, Multi-Scale Approach to Non-Adiabatic Charge Transport in High-Mobility Organic Semiconductors, *J. Chem. Theory Comput.* 2015, **11**, 5068-5082.

S26. A. Kubas, F. Gajdos, A. Heck, H. Oberhofer, M. Elstner and J. Blumberger, Electronic couplings for molecular charge transfer: benchmarking CDFT, FODFT and FODFTB against high-level ab initio calculations. II, *Phys. Chem. Chem. Phys.* 2015, **17**, 14342-14354.

S27. D. J. Evans and B. L. Holian, The Nose–Hoover thermostat, *J. Chem. Phys.* 1985, **83**, 4069-4074.

S28. J. Wang, R. M. Wolf, J. W. Caldwell, P. A. Kollman and D. A. Case, Development and testing of a general amber force field, *J. Comput. Chem.* 2004, **25**, 1157-1174.

S29. U. C. Singh and P. A. Kollman, An approach to computing electrostatic charges for molecules, *J. Comput. Chem.* 1984, **5**, 129-145.

S30. G. A. Petersson, A. Bennett, T. G. Tensfeldt, M. A. Al-Laham, W. A. Shirley and J. Mantzaris, A complete basis set model chemistry. I. The total energies of closed-shell atoms and hydrides of the first-row elements, *J. Chem. Phys.* 1988, **89**, 2193-2218.

S31. J. W. Borchert, B. Peng, F. Letzkus, J. N. Burghartz, P. K. L. Chan, K. Zojer, S. Ludwigs and H. Klauk, Small contact resistance and high-frequency operation of flexible low-voltage inverted coplanar organic transistors, *Nat. Commun.* 2019, **10**, 1119.

S32. M. Geiger, R. Acharya, E. Reutter, T. Ferschke, U. Zschieschang, J. Weis, J. Pflaum, H. Klauk and R. T. Weitz, Effect of the Degree of the Gate-Dielectric Surface Roughness on the Performance of Bottom-Gate Organic Thin-Film Transistors, *Adv. Mater. Interfaces* 2020, **7**, 1902145.

S33. M. Geiger, M. Hagel, T. Reindl, J. Weis, R. T. Weitz, H. Solodenko, G. Schmitz, U. Zschieschang, H. Klauk and R. Acharya, Optimizing the plasma oxidation of aluminum gate electrodes for ultrathin gate oxides in organic transistors, *Sci. Rep*, 2021, **11**, 6382.

S34. H. Klauk, Organic thin-film transistors, *Chem. Soc. Rev.*, 2010, **39**, 2643-2666.